THESE DE DOCTORAT

Presentée à

L'UNIVERSITE DE LILLE

Ecole Doctorale Régionale Science Pour L'Ingénieur Lille Nord-de-France

Université de Lille

pour obtenir le grade de

DOCTEUR EN SCIENCES

Dans la spécialité :

Electronique, microélectronique, nanoélectronique et micro-ondes

par

Chengnan LI

Heat-based Nanotechnologies: Application For Photothermal Pathogen Ablation and Transdermal Drug Delivery

Directeur de thèse :

Prof. Sabine SZUNERITS

Soutenue le 4 Avril 2019 devant le jury composé de :

Dr. Céline FROCHOT	Rapporteur	Université de Lorraine
Dr. Hervé HILLAIREAU	Rapporteur	Université Paris-Sud
Prof. Sorin MELINTE	Examinateur	Université catholique de Louvain
Prof. Tuami LASRI	Examinateur	Université de Lille
Dr. Rabah BOUKHERROUB	Examinateur	CNRS

iemn

cnrs

CHINA SCHOLARSHIP COUNCIL

ACKNOWLEDGEMENT

This research work was conducted at the Nanobiointerfaces (NBI) group of the Institut d'électronique de microélectronique et de nanotechnologie (IEMN). I would like to express my deepest gratitude to all the people who have helped and encouraged me during the last three and a half years' PhD career.

First of all, I would like to render my warmest thanks to my supervisors, Prof. Sabine Szunerits and Dr. Rabah Boukherroub, for their patient guidance, expert advice and friendly encouragement throughout my time as their student. Scientific talks with Sabine always keep me on the right track to move forward. It is a great honor for me to share with her sharp views, exceptional scientific knowledge and positive working attitude. I am also grateful for all the precious time she spent on correcting my thesis and all the other reports. I would like to acknowledge my indebtedness to Rabah for his valuable suggestions in research and constant support in both administrative papers and daily life. As group leader, his easygoing personality provides us a relaxing research environment. Experiences of working with them will be beneficial for the rest of my life.

I would like to extend my thanks to Prof. Sorin Melinte and Ran Ye for providing K/Au NHs interfaces and Dr. Rostyslav Bilyy for all the *in vivo* experiments. My special thanks are due to Prof. Musen Li from Shandong University, who encouraged me to pursue my PhD study in France. He is a kind and generous mentor who is always there to provide me support and encouragement for my study and future career life.

I am thankful to all the jury members for sharing their precious time to read my thesis and to participate in my PhD defense. Their valuable advice on the corrections of my thesis help me to think more globally.

I am grateful to all the colleagues during my stay in the NBI team. My heartfelt thanks go to Alex for his patient instructions to detailed manipulations and experiments. He has been helpful in almost all the work I did and advice to daily routines. I am thankful to Roxana, Florina and Santosh for showing me how to do bacterial and chemistry experiments at the beginning of my PhD. My gratitude goes to Hakim, Sawsen and Ioana for helping me to deal with language and registration problems. I would also like to thank Patrik, Milica, Aleks,

Anna, Vlad, Abir, Lylia, Mathias, Quentin, Emerson, Léa and all my lab mates for all those pleasant talks and enjoyable times spending together.

I must thank all my friends who have offered great help and encouragement to me. I would extend my sincere thanks to Qi Wang for giving me advice even before I came to France. My earnest gratitude is attributed to Ning Cao and Qian Wang for picking me up at the train station, helping me to settle down in France, as well as guiding me in research work. I would also like to thank Zijie Wang, Jian Zhang, Yue Wang, Yuanyuan Cheng, Fei Wang, Yuan Zhang, Min Li, Liuqing Pang, Tianlong Yu, Jing Zhang and other friends for their invitations of parties, delicious food and constant encouragement during my stressful times

In particular, I thank Chinese government for offering me with the Chinese Scholarship Council (CSC) Award as financial support, which allowed me to conduct this research work in France. I owe my most sincere gratitude to my dear parents. They are always there for me with unconditional love, encouragement and understanding throughout my life. I have gained a great spiritual support from them. Lastly, I would extend the deepest gratitude to my beloved wife for her long-lasting companionship. Her love makes my life colorful and powerful. She is my most solid backing for pursuing my PhD in France.

Chengnan Li

Villeneuve D'Ascq, France

14th February, 2019

RÉSUMÉ

Malgré la disponibilité de différents antibiotiques, les infections bactériennes demeurent l'une des principales causes d'hospitalisation et de mortalité. L'échec clinique du traitement antibiotique est dû à une faible pénétration générale des antibiotiques dans les sites d'infection bactérienne ainsi qu'au développement de pathogènes résistants aux antibiotiques. La mise au point de stratégies antibactériennes alternatives moins soumises aux forces sélectives à l'origine de l'apparition d'une résistance acquise aux antibiotiques est devenue un besoin urgent. Les températures supérieures à 70 °C provoquent généralement une destruction instantanée des bactéries. L'ablation bactérienne par la chaleur est par conséquent une stratégie intéressante à poursuivre. Dans cette thèse, l'ablation photothermique d'agents pathogènes est étudiée. Le développement d'un patch photothermique flexible à base d'un film mince de poly (imide), Kapton, modifié avec de l'oxyde de graphène réduit (rGO) a permis un traitement rapide et très efficace des infections de plaies sous-cutanées par irradiation dans le proche infrarouge. L'isolement magnétique et spécifique dans le sérum de *E. coli* responsable d'infection des voies urinaires (UTI) était possible à l'aide de nanocomposites rGO magnétiques modifiés avec des anticorps anti-fimbrial *E.coli*. Un "nanotransporteur" magnétique optimisé atteint une efficacité de capture de 99.9%, même à des concentrations de $1x10^{1}$ cfu mL^{-1} de *E. coli* en 30 min. L'irradiation du nanocomposite chargé de *E. coli* avec un laser proche de l'infrarouge entraîne l'ablation totale des agents pathogènes éliminés.

Parallèlement, l'administration de médicaments transdermiques à base de chaleur a été envisagée pour l'administration d'antibiotiques et d'autres médicaments tels que la metformine. Des hydrogels d'oxyde de graphène (GO)/metformine et d'hydrogel de graphène réduit enrichi en acide carboxylique (rGO-COOH)/metformine ont été notamment fabriqués, leur profil de chauffage ainsi que la perméabilité à travers la peau de la metformine ont été déterminés.

Mots clés: graphène; photothermique; antibactérien; infection de la peau; isolation bactérienne magnétique; administration transdermique.

ABSTRACT

Despite the availability of different antibiotics, bacterial infections are still one of the leading causes of hospitalization and mortality. The clinical failure of antibiotic treatment is due to a general poor antibiotic penetration to bacterial infection sites as well as the development of antibiotic resistant pathogens. The development of alternative antibacterial strategies that would be less subject to the selective forces that drive the emergence of acquired antibiotic resistance has become an urgent need. Temperatures higher than 70°C cause generally an instant killing of bacteria. Heat based bacterial ablation is consequently an interesting strategy to pursue. In this thesis, photothermal ablation of pathogens is investigated. The development of a flexible photothermal patch based on a poly(imide) thin film, Kapton, modified with reduced graphene oxide (rGO) allowed for a rapid and highly efficient treatment of subcutaneous wound infections *via* near-infrared irradiation. Magnetic and specific isolation of *E. coli* associated with urinary tract infection (UTIs) from serum was possible using magnetic rGO nanocomposites modified with anti-fimbrial *E.coli* antibodies. An optimized magnetic nanocarrier achieved a 99.9 % capture efficiency even at *E. coli* concentrations of $1x10^1$ cfu mL^{-1} in 30 min. Irradiation of the *E. coli* loaded nanocomposite with a near-infrared laser resulted in the total ablation of the eliminated pathogens.

In parallel, heat-based transdermal drug delivery has been considered for the delivery of antibiotics and other drugs such as metformin. Graphene oxide (GO)/metformin and carboxylic acid enriched reduced graphene oxide (rGO-COOH)/metformin hydrogels were notably fabricated and their heating profile as well as metformin permeability across skin were determined.

Key words: graphene; photothermal; antibacterial; skin infection; magnetic bacterial isolation; transdermal delivery.

TABLE OF CONTENT

ACRONYMS

Au NHs	Gold nanoholes
AMPs	Antimicrobial peptides
BHI	Brain Heart Infusion medium
BSA	Bovine Serum Albumin
CVD	Chemical vapor deposition
CDC	the Center of Disease Control
DNA	Deoxyribonucleic acid
EDC	1-Ethyl-3-(3-dimethylaminopropyl)carbodiimide
E .Coli	*Echerichia coli*
E. feacalis	*Enterococcus faecalis*
FDA	Food and Drug Administration
FTIR	Fourier transformed-infrared spectroscopy
G	Graphene
GO	Graphene oxide
G6P	Glucose 6 phosphatase
HPLC	High performance liquid chromatography
HRTEM	High resolution transmission electron microscopy
H&E	Hematoxylin & Eosin
IHH	Immortalized Human Hepatocytes
K/Au NHs	Kapton modified with gold nanoholes
K/Au NHs-G	Graphene coated kapton modified with gold nanoholes
K/Au NHs-rGO	Reduced graphene oxide coated kapton modified with gold nanoholes
LB	Luria-Bertani medium
MDR	Multiple drug resistance
MNs	Microneedles

MP	Magnetic nanoparticles
MP_{ND}	2-nitro dopamine stabilized magnetic nanopatticles
MRS	Man-Rogasa-Sharpe medium
NHS	*N*-Hydroxysuccinimide
NIR	Near infrared light
NMR	Nuclear magnetic resonance
PBP	Penicillin-binding proteins
PBS	Phosphate buffered saline
PDT	Photodynamic therapy
PI	Propodium iodide
PS	Photosensitizer
PTT	Photothermal therapy
pyrene-PEG	N-(26-azido-3,6,9,12,15,18,21,24-octaoxahexacosyl)-pyrene-1 Carboxamide
QS	Quorum sensing
rGO	Reduced graphene oxide
rGO-COOH	Carboxylic acid enriched reduced graphene oxide
rGO/ MP_{ND}	Reduced graphene oxide coated 2-nitro dopamine stabilized magnetic Nanopatticles
ROS	Reactive oxygen species
SC	Stratum corneum
SEM	Scanning electron microscope
SLNs	Solid-lipid nanoparticles
SPR	Surface plasmon resonance
S. aureus	*Staphylococcus aureus*
S. epidermidis	*Staphylococcus epidermidis*
TDD	Transdermal drug delivery

TLC	Thin layer chromatography
UTIs	Urinary tract infections
WHO	World Health Organization
XPS	X-ray photoelectron spectrometry

OBJECTIVES

In recent years, the great development of nanotechnology has fueled the application of nanomaterials in biomedical treatment. Photothermal therapy (PTT) is a newly developed and encouraging therapeutic modality, which employs light absorbing nanomaterials to generate heat for thermal therapy under laser irradiation. PTT has been extensively investigated for cancer cells ablation owing to its unique advantages such as high selectivity, minimal invasiveness and precise spatial-temporal selectivity. In this thesis, based on photothermal therapy, different nanomaterials, notably graphene based nanomaterials, were synthesized for antibacterial treatment and enhanced transdermal drug delivery (TDD). Photothermal ablation can effectively compromise bacterial cells without causing antibiotic resistance. While on the other hand, photothermal heating can significantly enhance skin permeation, resulting in enhanced TDD.

Following this idea, this thesis will be constructed in 5 chapters. In **Chapter 1**, a general overview will be presented on antibiotic resistance and alternative strategies, challenges of transdermal drug delivery and current enhancing strategies, as well as the application of PTT in antibacterial treatment and TDD.

In **Chapter 2**, a reduced graphene oxide (rGO) coated gold nanoholes (Au NHs) flexible photothermal patch will be introduced for rapid and efficient treatment of subcutaneous bacterial infections. This patch combines the outstanding near infrared (NIR) photothermal properties of Au NHs patterned on flexible polyimide surface with that of rGO nanosheets, resulting in the formation of well-adapted photothermal patch for NIR laser inactivation of bacteria. The fabricated patch was then applied for photothermal antibacterial tests both *in vitro* and *in vivo*.

In **Chapter 3**, a 2-nitrodopamine coated magnetic nanoparticles (MP_{ND})/ rGO nanocomposites will be demonstrated for rapid and efficient separation of bacteria from water. The large surface area of rGO offers good bacterial capture efficiency while the magnetic property renders contactless magnetic separation. Further decoration of poly(ethylene glycol) modified pyrene units (pyrene-PEG) and anti-fimbrial *E.Coli* antibodies allows selective separation of urinary tract infections (UTIs) related *E.Coli* from serum. Moreover, the good photothermal heating property of rGO provides the possibility to complete inactivation of the

isolated bacterial cells through laser irradiation.

In **Chapter 4**, self-assembled graphene oxide (GO)/metformin and carboxylic acid enriched reduced graphene oxide (rGO-COOH)/metformin hydrogels will be shown for photothermal enhanced transdermal delivery of metformin. The fabrication process can be realized through a simple one-step mixing of GO or rGO-COOH with metformin in a certain ratio. The driving forces of gelation, including hydrogen bonding and electrostatic interactions, can be readily weakened through photothermal heating, triggering the release of metformin. On the other hand, skin permeation can be enhanced at elevated temperature, achieving synthetic enhancing effect for transdermal delivery of metformin. Transermal permeation study will be carried out on Franz cells and the activity of photothermally heated metformin will be verified by monitoring its effect on glucose 6 phosphatase catalytic (G6P) gene expression. Lastly, conclusions and perspectives will be drawn in **Chapter 5**.

CHAPTER 1 INTRODUCTION

In the last few decades, medical technology has experienced a great development, which leads to the tremendous increase of world average life expectancy from 48 years old in 1950s to 71.5 years old in 2014 [1]. However, despite the great achievement we have got in medical technology, there are still many serious health problems to be addressed. Antibiotic-resistant bacterial infection is one of the major concerns. According to the data, more than 63,000 patients from the United States of America (USA) die every year from hospital-acquired bacterial infections [2] and an estimated 25,000 patients die due to multiple drug resistance (MDR) bacterial infections in Europe [3]. Although new antibiotics have been developed, the pace of development is slow compared to the emergence of resistant strains. Past experience has proven that the use of any conventional antibiotic will ultimately lead to the emergence of such resistance. In addition, many forms of bacterial infection, specifically those associated with biofilm formation, are intrinsically resistant to antimicrobial therapy regardless of the acquired resistance status of the offending bacteria [4]. Thus, the development of alternative antibacterial strategies that would be less subject to the selective forces that drive the emergence of acquired antibiotic resistance has become an urgent need.

Apart from the serious health problems, in the meanwhile, people are seeking for a more patient compliant drug delivery route other than regular routes: oral intake and hypodermic injection. Oral uptake is easy, economic and safe, but always turns out to be less efficient due to the drug degradation in stomach and the first pass metabolism in liver and gut. Hypodermic injection is fast and efficient, but painful and less patient compliant at the same time. Transdermal drug delivery, which refers to deliver drug through skin and into bloodstream, represents an attractive alternative to the other two routes. It has made an important contribution to medical practice, but has yet to fully achieve its potential as an alternative to the regular routes [5], as due to the special structure of skin, only few lipophilic drugs with a molecular mass up to 500 Daltons are permitted in this route [6]. It remains a great challenge to exploit the transdermal route to deliver hydrophilic drugs, peptides and macromolecules.

1.1 Antibiotic-resistant crisis and alternative strategies

1.1.1 Mechanisms of action of antibiotics

Over the last 90 years since the first discovery of penicillin by Scottish Scientist Alexander

Flaming, antibiotics have saved millions of lives. Nowadays, antibiotics still play an important role in treating and preventing bacterial infections. There are over 100 types of antibiotics available in the market, they can be divided into different classes according to the chemical structure. Despite the various types of antibiotics, there are mainly three different ways through which they act on bacterial cells, namely the inhibition of cell wall synthesis, DNA or RNA synthesis and protein synthesis (**Figure 1.1**) [7].

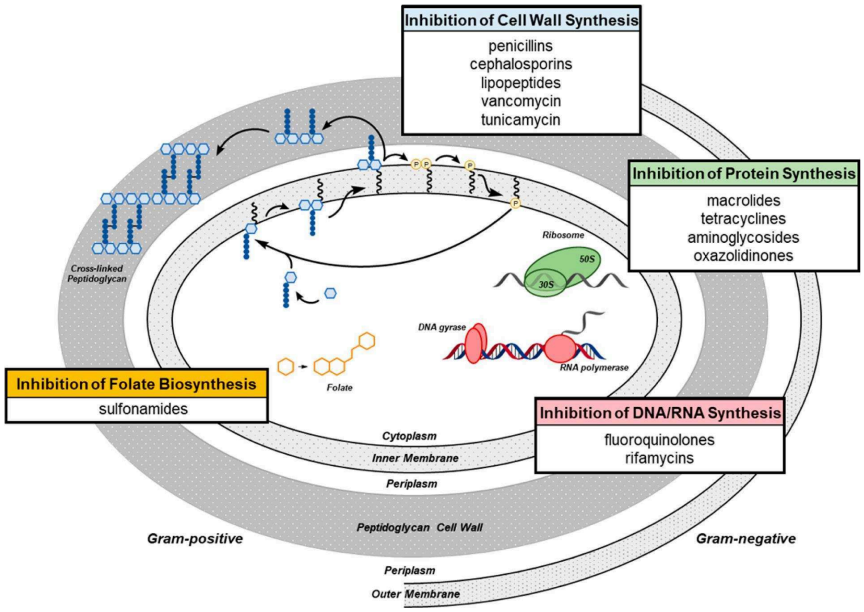

Figure 1.1: Three major mechanisms of action of widely used antibiotics [7].

Bacterial cell wall is a peptidoglycan-abundant layer which can protect the cell from internal turgor pressure. The maintenance of peptidoglycan is largely supported by the activity of transglycosylases and penicillin-binding proteins (PBP), which add disaccharide pentapeptides to extend the glycan strands of existing peptidoglycan molecules and cross-link adjacent peptide strands of immature peptidoglycan units, respectively [8]. β-lactams and glycopeptides act by interfering with the specific biosynthesis process of cell wall. The cyclic amide ring of β-lactams mimics the binding site of PBP on the peptide chain, which can cause the unavailability of this important enzyme, leading to the failure of peptidoglycan biosynthesis [9]. Instead of interacting with enzymes, glycopeptides often act by binding peptidoglycan unit, preventing the cell wall construction from proceeding [7].

DNA is a nucleic acid that carries genetic information for the development and function of living things. Gyrase and topoisomerase IV are two important enzymes in the process of DNA replication and transcription, as gyrase can prevent excessive positive supercoiling by

introducing negative supercoils while topoisomerase IV is responsible for unlinking. Quinolones antibiotics, mostly fluoroquinolones, are able to bind to the DNA-enzyme complex, turning the important enzymes into cellular toxins [10]. This action will cause DNA strand breakage, which leads to an immediate cell death. Interestingly, quinolones have low affinity to topoisomerase II, which is existed in mammalian cells in place of gyrase and topoisomerase IV, making them low toxic drugs [11].

In the process of protein synthesis, mRNA is translated in a ribosome with the participation of other cytoplasmic accessory factors. Ribosome is composed of two ribonucleoprotein subunits, the 50S and 30S, which are targets of various types of antibiotics. 50S inhibitors, such as macrolides, oxazolidinones, act by blocking either the initiation of protein or translocation of peptidyl tRNAs. On a contrast, 30S inhibitors, include tetracyclines and aminoglycosides, work by blocking the access of aminoacyl tRNAs to the ribosome [12].

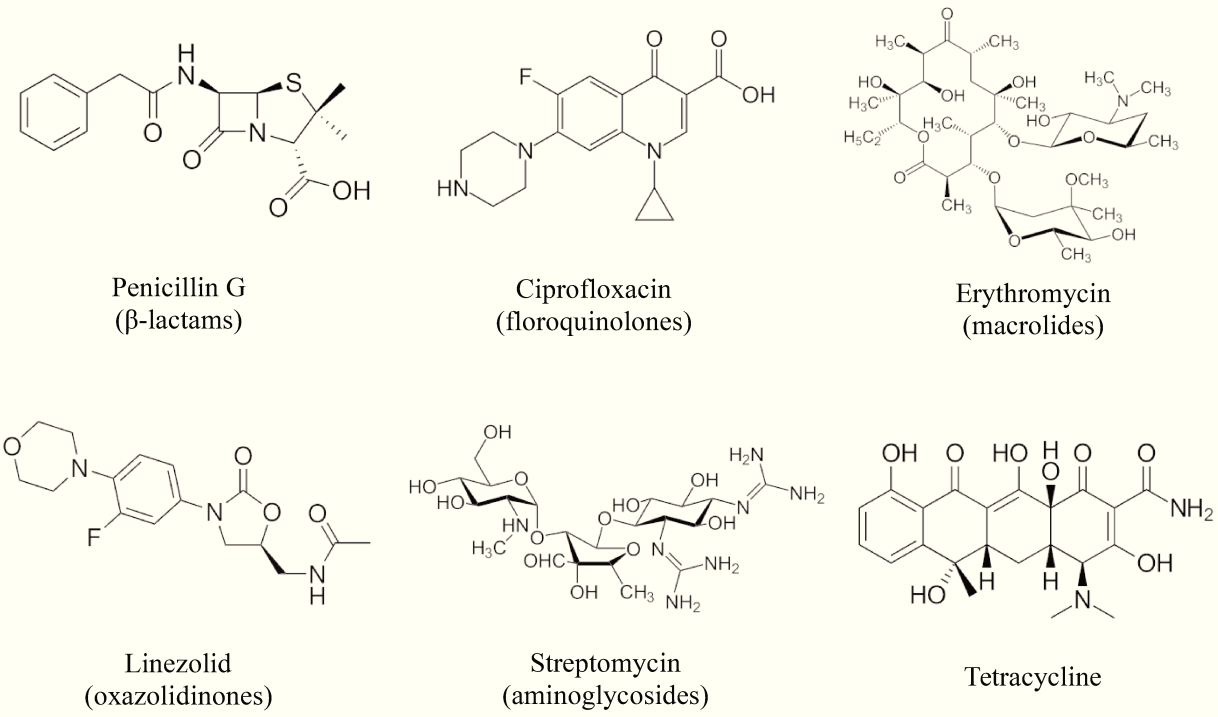

Figure 1.2: Chemical structures of typical antibiotics and their classes (in round brackets).

1.1.2 Mechanisms of antibiotic-resistance

Though the introduction of antibiotics is among the greatest achievements in 20th century, its brilliancy is dramatically compromised by antibiotic-resistance. The infections caused by antibiotic-resistant strains have resulted in elevated morbidity and mortality rates as well as increased treatment costs [13]. In the long history of revolution, bacteria have developed the

ability to adapt to harsh environmental changes. They can be either intrinsically resistant to some of the antibiotics or acquire the resistance through mutations or by horizontal gene transfer. Currently, resistance has been found to all the antibiotics available in the market, measures have to be taken to prevent the situation from going worse.

Typically, bacteria can protect themselves from antibiotic attack through three different ways. Namely, reduced penetration or increased efflux of antibiotics, modifications of antibiotic binding targets and metabolism or modification of antibiotics [14]. In the first case of resistance, reduced permeability of cell membrane and efflux pump are usually employed. The entry of hydrophilic antibiotics is realized by diffusing through outer membrane porin proteins. Therefore, reducing the permeability of the outer membrane and limiting antibiotic entry into the bacterial cell is achieved by the down regulation of porins or by the replacement of porins with more-selective channels. In addition, more studies have demonstrated that the selective pressure exerted by antibiotics prompts the emergence of mutations in porin genes, as well as in genes that regulate porin expression, thus protect the cell from the attack [15]. Efflux pumps actively transport small molecules out from bacterial cells, resulting in antimicrobial resistance. Some pumps are able to remove a wide range of drugs, contributing to the factor of multi-drug resistance.

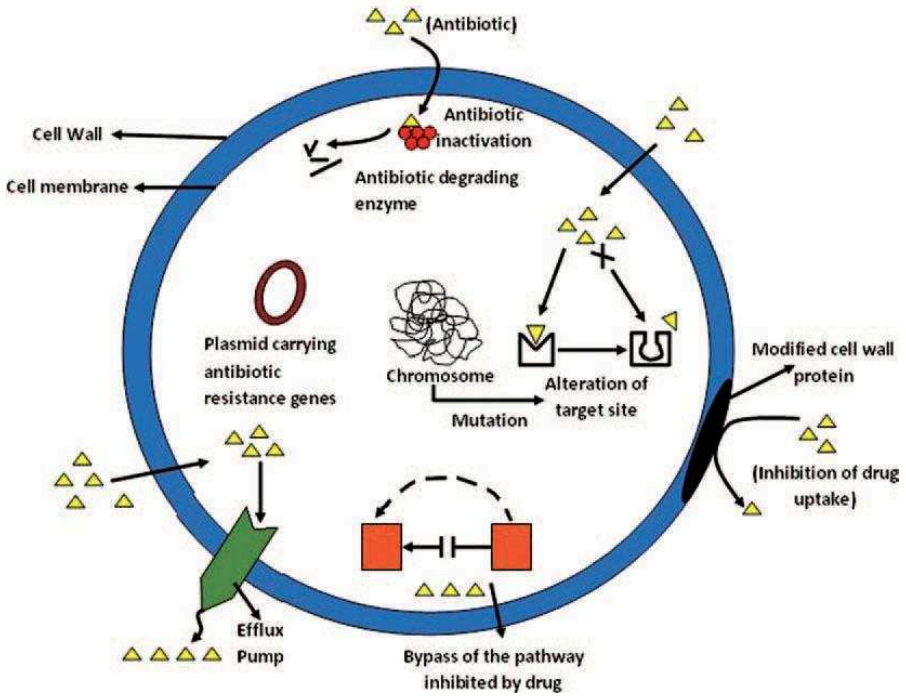

Figure 1.3: Different mechanisms of antibiotic resistance [16].

As aforementioned, most antibiotics have specific binding sites, thus lead to the failure of the targets. Therefore, introducing modifications to the binding site is another strategy taken in antibiotic resistance. The modifications are often realized through mutations or enzymatic alternations. Changes of the target prevent the binding of antibiotics while minimize the impact of the activity [17]. In some cases, the attack of antibiotics is diverted by the complete replacement or bypass of the binding site. The function of the target is completely substituted by new ones, or the effect of the drug is circumvented by the overproduction of the target [18].

Enzymatic-catalyzed inactivation is another weapon that bacteria use to fight against antibiotic killing. This mechanism relies on chemical modification of antibiotics. The discovery of this mechanism can be dated back as early to 1940s, the time when antibiotics were first used. Two distinct chemical mechanisms are known relating to this resistance: formation of a covalent enzyme intermediate followed by hydrolysis, or metal-activation of a nucleophilic water molecule [19].

1.1.3 Causes of the antibiotic resistance

In 2013, the Center of Disease Control (CDC) in the USA asserted that the human race is now in the "post-antibiotic" era. The next year, the World Health Organization (WHO) stated that the antimicrobial resistance is becoming dire [20, 21]. Antibiotics are no longer "wonder drugs" as they were before. Despite the great effort we have made, the resistance keeps rising. From different perspectives, there are various factors that result in the antibiotic resistance crisis.

First of all, microorganisms have a much longer revolution history than humankind, they have developed the ability to effectively and rapidly adapt to environmental change. Unlike multicellular organisms, these small creatures are too simple to have very complex genetic materials, therefore, they are not able to deal with environmental change individually. However, when considered as communities, they can compensate the shortage of simplicity through the huge populations and rapid generation time. Once a mutation happens in one bacterial cell, the number will be multiplied in a tremendous rate as the generation time may be as short as 20 min. Furthermore, they are endowed a gift with which the adaptive genes can be horizontally transferred between different cells in the same or different species [22]. So, once a selective pressure (application of antibiotics) is exerted on a bacterial community, the survivors will remarkably eclipse the effect of treatment, leaving the infections more tricky to be cured.

Overuse is another major cause of antibiotic resistance. As early as 1945, Sir Alexander Flaming warned that the increased public demand of antibiotics will begin an era of abuse [23]. Epidemiological studies have demonstrated a direct relationship between antibiotic consumption and the emergence and dissemination of resistant bacteria strains [24]. Though being warned regarding overuse, antibiotics are prescribing worldwide. Based on a data obtained by estimating the amount of antibiotics sold in retail and hospital pharmacies, an analysis demonstrated that 22 standard unit of antibiotics were prescribed per person in the U.S. in 2010 [25]. This number is even greater in developing countries where there is less regulation regarding antibiotics. Moreover, overuse is not restricted in the domain of medical treatment. In agriculture, antibiotics are used to prevent infections and promote growth of livestock, some of the drugs are also applied on fruits as pesticides [26, 27]. These antibiotics, either consumed by human through taking the contaminated agricultural products or exerted by livestock, will favor the emergence of "superbugs".

Besides, the shortage of new antibiotics makes the situation even worse. The development of new antibiotics is an effective way to combat resistance. However, the introduction of new drugs is far behind the path of new resistances. As we can see from **Figure 1.4**, the number of new antibiotic application approvals were decreasing since the year of 1983, while only a bit climbing up since the year of 2013. Economic obstacles largely resulted in this dilemma. The

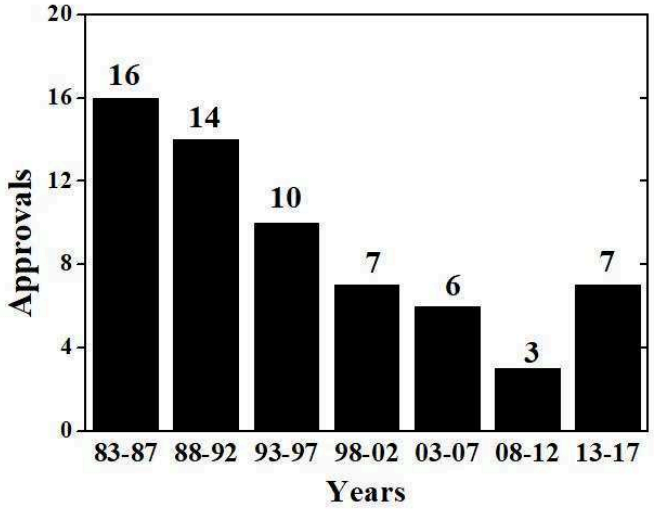

Figure 1.4: Number of Antibacterial New Drug Application Approvals by FDA Versus Year Intervals.

development of new drugs requires enormous investment, while this investment is often not

rewarding. Once a new agent is applied, the resistance is nearly inevitable. Manufacturers often find that resistance is already developed before they start to make profits. In this regard, unwilling to risk this economic uncertainty, 15 out of the 18 largest pharmaceutical companies have abandoned the development of new antibiotics [28]. In those largest companies, only Merck, Roche and Pfizer are remaining active in antibiotic programs.

1.1.4 Alternative strategies against antibiotic resistant infections

The loss of effectiveness of antibiotics makes people helpless when facing antibiotic resistant infections, which are already worldwide spread. For example, the notorious Methicillin-Resistant *Staphylococcus Aureus* was found to be the arch criminal of 11,285 deaths per year in the US alone [29]. Together with other multi-drug resistant strains, such as Vancomycin-Resistant *Enterococci*, Drug-Resistant *Streptococcus pneumoniae* etc., they pose great threat to human health life. This critical situation forced people to develop new approaches in combating against the "superbugs".

1.1.4.1 Anti-virulence strategies

As an alternative strategy, inhibition of virulence has drawn much attention. Compared with antibiotics, this kind of method is less likely to apply selective pressure for the development of resistance as most of the virulence traits are not essential for bacterial survival. The virulence traits, such as quorum sensing pathways, toxin production, adhesive mechanisms, specialized secretion systems and regulation of virulence genes, account for the colonization of bacteria, resulting in serious infectious diseases [30, 31]. The inhibition of these traits allows innate immune system to protect the host from bacterial colonization or to remove the colonized non-virulent bacteria.

Quorum sensing (QS) inhibitor is one of the most investigated anti-virulence strategies. QS is a process through which bacteria can sense the population density thus regulates the expression of virulence factors and the formation of biofilms [32]. It includes three steps: synthesis and secretion of signaling molecules, detection of the concentration of signaling molecules and regulation of the gene express accordingly [33]. QS can be circumvented *via* interrupting the synthesis and reception process of signaling molecules, minimizing the effect virulence factors.

Though regarded as a promising approach to combat antibiotic resistance, the feasibility of anti-virulence therapies is still to be verified. As none of these strategies has received broad-

scale clinical trial, the potential side-effects are remaining unknown. Moreover, though it is predicted that less selective pressure will be exerted through these methods, resistance is still possible likely to develop over time due to the fast revolution of bacteria.

1.1.4.2 Antibiotic alternatives

Biologics are considered as alternative strategies than antibiotics. They are less likely to give rise to resistance as most of them are natural products that are found in organisms varying from microorganisms to mammals. Typical biologics employed in fighting against bacteria include antimicrobial peptides, bacteriophage.

Antimicrobial peptides (AMPs) have drawn much attention as a substitution of antibiotics. AMPs are diverse, biologically activate molecules of the innate immune system, protecting the host against infections. They exhibit a broad-spectrum of antimicrobial activities, targeting both gram-positive and gram-negative bacteria, as well as fungi and viruses [34]. Due to the multiple cellular targets that AMPs aim, including cell membrane and intracellular targets [35], it is difficult for microbes to develop resistance compared with antibiotics. It is accepted that the positively charged groups on AMPs can interact with negatively charged bacterial membranes, causing cytoplasmic leakage that leads to cell death. The disruption of cell membranes also enables AMPs to enter bacterial cell, resulting in the inhibition of nucleic acid and protein synthesis. Besides, some of the peptides are known to be able to strengthen the host immune system through chemokine induction, histamine release and angiogenesis modulation, thus increase the clearance of pathogens. Up to now, several existed databases are covering more than 2000 peptides, and the list is still accumulating[36]. In **Table 1.1** listed some of the antimicrobial peptides that are approved by FDA. Though showing superior properties than other antibiotics, there exists several hurdles to clinical application of AMPs, such as their high cost and toxicity, as well as fast degradation rate [32]. It is estimated that the cost of producing a 5000 Da molecular mass peptide exceeds more than 10-fold of the production cost of a 500 Da molecular mass small molecule[37]. The fast degradation rate of AMPs makes oral intake almost impossible, the most common routes of administration, as we can see from **table 1.1**, are topical or injection. Even so, the peptides are prone to degradation by tissue proteolytic enzymes, limiting their wide clinical applications.

Table 1.1. List of some antimicrobial peptides FDA-approved to be used in therapeutics[37].

Name	Peptide	Category	Target disease	Route of administration
Bacitracin	Mixture of related cyclic peptides	Antimicrobial	Pneumonia and empyema in infants (*staphylococci*)	Topical
Dalbavancin	Lipoglycopeptide	Antimicrobial	Adult patients with acute bacterial skin and skin structure infection	Intravenous
Daptomycin	Lipopeptide	Antimicrobial	Bacterial infections of skin and underlying tissues	Intravenous
Oritavancin	Glycopeptide	Antimicrobial	Acute bacterial skin and skin structure infection	Intravenous
Teicoplanin	Glycopeptide	Antimicrobial	Several skin, soft tissue, bone, joint, urinary tract, endocarditis and peritonitis associated with continuous ambulatory peritoneal dialysis	Intravenous
Telavancin	Cyclic lipoglycopeptide	Antimicrobial	Methicillin-resistant *Staphylococcus aureus* and other Gram-positive infections	Intravenous
Vancomycin	Glycopeptide	Antimicrobial	Gram-positive bacteria	Intravenous

Bacteriophages offer another promising therapeutic strategy against antibiotic resistance. These viruses, which can specifically infect and kill bacteria, were discovered in early 1900s and received extensive investigations in treating bacterial infections until 1930s, when broad spectrum antibiotics were found. The occurrence of antibiotic resistance prompts reconsideration of phage therapy. Phage therapy exhibits several advantages over conventional antibiotics. Firstly, phages are natural predators of bacteria, they show high specificity on their targets without effecting eukaryotic cells. Besides, their rapid replication inside bacterial cells renders a persistent remedy of the infectious site. Moreover, their high tissue permeability enables them to cure deep rooted infections, including biofilm infections. Although phage therapy displays great superiorities over other strategies, there exists also some setbacks that prevent it from practical application. For example, due to the high specificity on certain bacterial species, it is necessary to identify the pathogen causing the infection before to apply the right phage. Application of phage triggers immune response leading to the production of antibodies, which can drastically reduce the effectiveness of the antimicrobial treatment.

1.1.4.3 Nanomaterials

In recent years, the great development in nanotechnology has sparked tremendous

investigations in its application in fighting against the spread of antibiotic resistance. Due to the unique physical and chemical properties of nanomaterials, including small size, high surface to volume ratio and facile surface modifications, they can be tailored into different weapons against bacteria [38]. Typically, according to the functions of these nanomaterials, they can be divided into three different categories, namely, direct antibacterial nanomaterials, antibacterial drug vehicles and stimuli responsive antibacterial agents.

Direct antibacterial nanomaterials act by directly interacting with bacterial cells and thus kill bacteria. To date, many nanomaterials have been explored, they can be generally divided into two categories based on different components: inorganic and organic antibacterial nanomaterials. Inorganic antibacterial nanomaterials are mainly composed of metal and metal oxides nanoparticles, including silver, zinc oxide, titanium oxide and copper oxide etc. [39]. The exact mechanisms of antibacterial effect for these materials are still under investigation. But there exists two mainstream explanations: (I) the metal ions released from these nanoparticles lead to toxicity to bacterial cells. (II) reactive oxygen species (ROS) generated on the surface of nanoparticles result in oxidative stress to bacteria [40] (**Figure 1.5**). Transition metallic nanoparticles, such as Cu, Fe, influence oxidative stress ($\cdot O_2^-$ and $\cdot OH$) via Fenton reaction, while other nanoparticles, such as Ag, can depolarize the mitochondrial membrane and to interfere with the electron-transport chain, resulting in accumulated level of $\cdot O_2^-$ [41]. In addition, shape, size, surface charge of the reagents are also reported to play important roles in killing bacteria [42, 43]. Organic antibacterial nanomaterials often refer to cationic polymeric nanoagents, such as quaternary ammonium compounds, N-Halamine compounds and chitosan. The cationic groups on the long chains of these polymers are able to penetrate bacterial cell membrane, they are also reported to kill bacteria by attaching to bacterial cells, disrupting ion exchanges, which will lead to bacterial cell death.

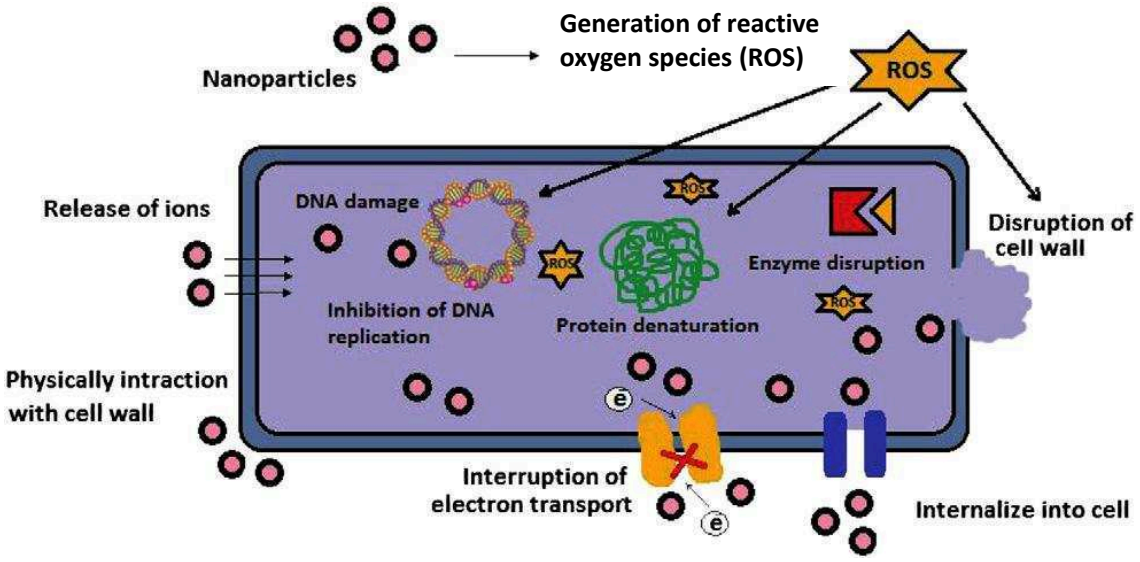

Figure 1.5: Various mechanisms of antimicrobial activity of the metal nanoparticles [44].

Targeted antimicrobial drug delivery via nanoparticles is another promising way to restrict the development of antibiotic resistance. Antibiotics are administrated locally to the site of infection through this method to avoid systemic exposure to the drugs, which potentially reduces resistance development [45]. In addition, nanoparticles capped antibacterial drugs exhibit improved drug half-life and better water solubility, which renders a better therapeutic efficacy [46]. Amphiphilic nanoparticles such as liposomes, polymeric nanoparticles and some dendrimers have received extensive studies as antibiotic vehicles due to their outstanding properties. For example, liposomes, the nanosized vesicles comprising of phopholipid bilayer with an aqueous core, can capsulate both hydrophobic and hydrophilic antimicrobial drugs. Once the particles reach bacterial cells, they can mimic the cell membrane and fuse with infectious bacteria, causing a burst release of drugs [47]. To further strengthen antibacterial effect, reports have been found to use combinatorial antibiotic release or metal nanoparticles-antibiotic complex to broaden the antimicrobial spectrum and generate synergy to counteract antibiotic resistance [48-50].

Stimuli responsive antibacterial nanoparticles refer to the nanoparticles that remain inactivate until triggered by outer stimuli. Compared with other kinds of antibacterial nanoparticles, stimuli responsive nanoparticles further enhance the therapeutic efficacy, as they are more controllable and more efficient [51, 52]. Common stimulations include pH, enzyme activities, light, magnetic field etc. Innate stimulations such as change of pH and enzyme activities can automatically trigger the antibacterial effect once the nanoparticles reach the site of infection. Pornpattananangkul *et al.* demonstrated carboxyl-modified gold nanoparticles attached

phospholipid liposomes, which remain stable at physiological pH while fuse with bacterial cells at acidic pH due to the detach of protonated gold nanoparticles. This kind of liposomes can be potentially applied as antimicrobial compound vehicles to treat skin infections where always display an acidic pH [53]. Komnatnyy *et al.* reported a promising antimicrobial compound release method based on extracellular lipase, an enzyme that is abundant in the site of infection. The antibacterial compounds were loaded onto polymeric surface through lipase-sensitive linkages which can be broken when interacting with lipase and thus cause the release of drugs [54]. Besides, external stimuli responsive nanoparticles are arising as promising agents in fighting against bacterial infections due to their fast therapeutic effect. Magnetic nanoparticles are employed in rapid eradication or removal of bacteria, the particles guided by magnetic field exhibit potent killing effect on bacteria. Geilich *et al.* [55] proved that the magnetic nanoparticles can penetrate thick biofilm following the application of external magnetic field. Our group synthesized magnetic reduced graphene oxide nanocomposites for rapid and selective isolation of pathogenic bacteria [56]. Photoactive therapeutic modalities, including photodynamic and photothermal therapy have received extensive studies. Photodynamic therapy (PDT) is originally used as a therapeutic modality for the treatment of oncological pathologies and recently applied in dealing with localized infections. PDT is a process that combines a non-toxic photosensitizer (PS) and a harmless light of appropriate wavelength to promote a phototoxic effect on the targeted cells via oxidative damage (**Figure 1.6**) [51]. In the PDT process, PS first absorbs photons from light and reaches an excited state,

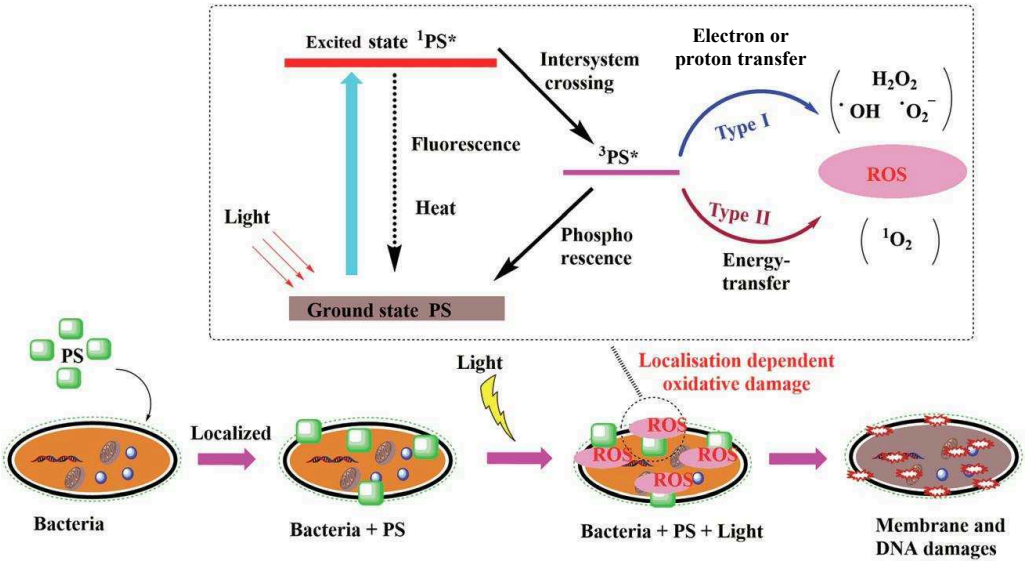

Figure 1.6: Schematic illustration of photodynamic inactivation of bacteria under light irradiation [51].

followed by switching to more stable triplet state through intersystem crossing. Then the triplet state of PS can transfer its electrons or protons to the surrounding matters to generate radical ions or pass its energy to molecular oxygen to produce singlet oxygen [57, 58]. The generated radical ions and singlet oxygen initiate oxidative damage of the cytoplasmatic membrane and DNA of bacteria cells [59]. To date, many studies have been published based on different PS agents, ranging from organic nanoparticles (porphyrines, phenothiazines, phthalocyanines) [60, 61] to inorganic nanoparticles (Au, Ag, and Pt) [62-64]. Photothermal therapy involves use the synergetic effect of light irradiation and light absorbing nanoparticles to achieve hyperthermia, the details are discussed in **Chapter 1.3**.

1.2 Transdermal drug delivery and enhancing strategies

For thousands of years, people have applied substances on skin for therapeutic effect, such as application of lotion to moisturize skin. In 1970s, Michaels and co-workers showed that some drugs have significant permeability through skin, which had fueled the development of transdermal drug delivery (TDD) [65, 66]. TDD is a novel route of administration in which drug is topically applied onto skin and finally flux into blood stream by penetrating skin. It has several advantages over conventional routes of administration. The short diffusive pathway enables TDD to avoid first pass metabolism through oral intake, while the noninvasiveness helps to advert pain in needle injection. Other merits include sustained delivery and improved patient compliance. However, TDD is not a flawless method, transdermal drug candidates have to meet several requirements due to the great barrier posed by skin. As is listed in Table 1.1, most FDA-approved transdermal delivery drugs are lipophilic small molecules (< 500 Daltons) that require low-dose administration.

Table 1.2. FDA-approved transdermal delivery systems [67].

Drug	Molecular Weight/Da	Indication	Year
Buprenorphine	467	Chronic Pain	2010
Capsaicin	305	Neutropathy	2009
Clonidine	230	Hypertension	1984
Diclofenac epolamine	411	Acute pain	2007
Estradiol	272	Menopausal symptoms	1986
Estradiol/levonorgestrel	272/312	Menopausal symptoms	2003
Estradiol/norethidrone	272/341	Menopausal symptoms	1998
Ethiryl estradiol/norethidrone	296/327	Contraception	2001

Fentanyl	337	Chronic pain	1990
Granisetron	312	Chemo-induced emesis	2008
Influenza-virs vaccine	122,000	Influenza virus	2011
Lidocaine with tetracaine	234/264	Local dermal analgesia	2004
Methylphenidate	233	Hyperactivity disorder	2006
Nicotine	162	Smoking cessation	1991
Nitroglycerin	227	Angina pectoris	1981
Oxybutynin	358	Overactive bladder	2003
Rivastigmine	250	Dementia	2007
Rotigotine	316	Parkison's disease	2007
Scopolamine	303	Motion thickness	1979
Selegiline	187	Depressive disorder	2006
Testosterone	288	Testosterone deficiency	1993

1.2.1 Skin structures

Skin, as our largest organ, provides a large surface for systemic drug administration. Human skin is comprised of different layers, including epidermis, dermis and subcutis. Drugs have to pass through the outer layers of skin to reach blood capillary in dermal layer. However, skin functions as a protection to our body by impeding the flux of toxins, which likewise pose a great barrier to the permeation of drugs. Stratum corneum (SC), the outermost layer of skin, is thought to be responsible for the barrier [66]. In the structure of SC (**Figure 1.7**), corneocytes are densely paved inside the extracellular lipid matrix, which is mainly composed of ceramide, cholesterol and fatty acid that are assembled into multi-lamellar bilayers. The special configuration of SC, often referred as 'brick and mortar' arrangement, displays a highly lipophilic property, which greatly inhibit the pass of hydrophilic molecules. In addition, the tight structure of SC leaves very limited intercellular space (less than 100 nm), which largely prevent the pass of macromolecules [68].

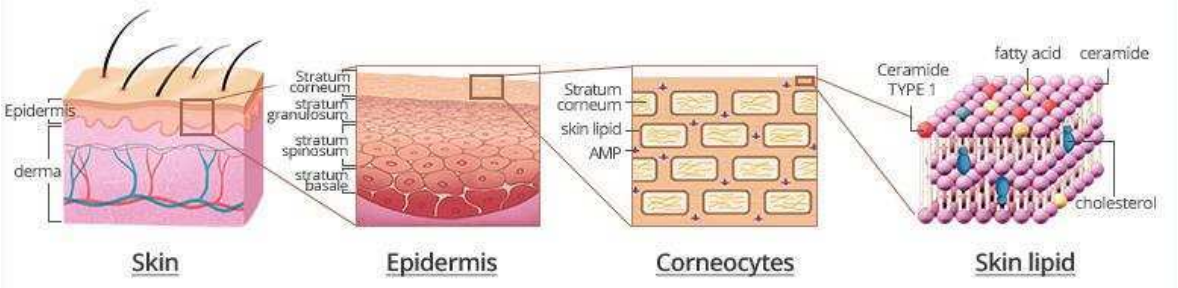

Figure 1.7: The structure of stratum corneum (http://zeroid.com/main/brand.asp?cate=272 &Pcate=267&Mcate=269).

1.2.2 Enhancing strategies for TDD

Since the first approval of transdermal patch by FDA in 1979, the list of drugs are accumulating. However, most of these drugs are lipophilic with small molecular weight. To broaden the class of drugs to be delivered through TDD, efforts have been made to develop new approaches to overcome the barrier of SC. These approaches can be broadly divided into two parts: passive and active technologies [69]. Passive technologies include chemical permeation enhancers and nanoparticles while active technologies are consisting ultrasound, electrically assisted methods (electroporation and iontophoresis), velocity based devices (powder injection, jet injectors), thermal approaches (lasers and radio-frequency heating) and mechanical methodologies such as microneedles (MNs) and tape stripping [70-73]. Passive methods are relatively easy to incorporate into TDD patches while the big lag time restricts its use in rapid onset drugs, such as insulin [74]. Active methods require more sophisticated systems, which could hinder its clinical application. However, they can effectively and rapidly deliver a much broader range of drugs, as well as offer more reproducible control over the delivery profiles of the medications. These advantages prompt active methods to be developed as novel TDD patches.

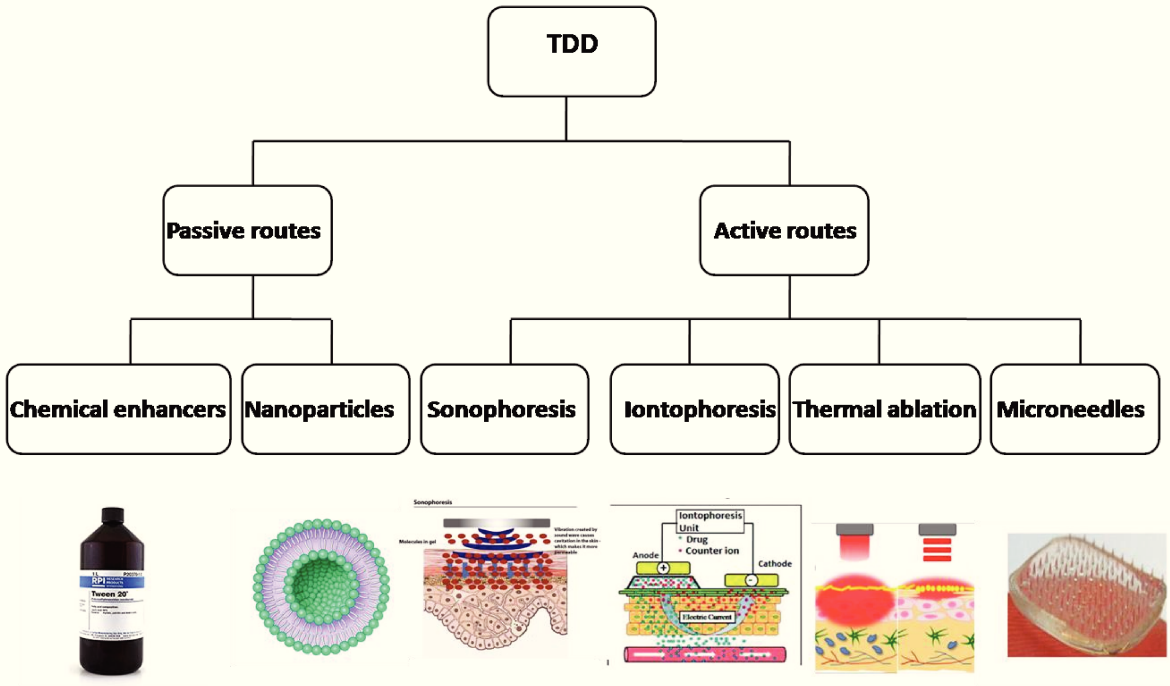

Figure 1.8: Different enhancing strategies of TDD (pictures reprinted from [75-79])

1.2.2.1 Chemical enhancers

Chemical enhancers have long been employed to increase transdermal delivery. Typically, chemical enhancers improve TDD through three different ways:

1. Disruption of the highly ordered structure of stratum corneum.
2. Interaction with intercellular protein.
3. Improved partition of the drug, coenhancer or solvent into the stratum corneum [80].

On top of the mechanisms, chemical enhancers should also fit several prerequisites such as low toxicity, no pharmacological activity within the body etc. Common chemical enhancers include sulfoxides, pyrrolidones, fatty acids and urea, etc.

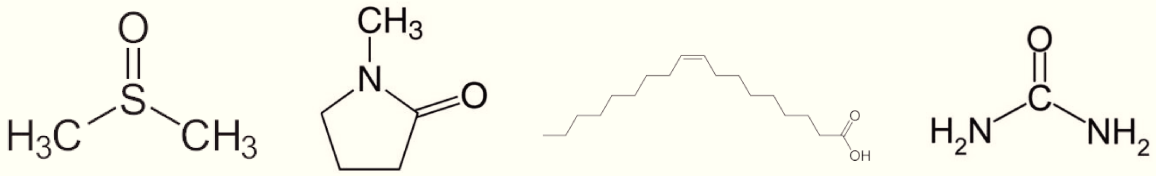

Dimethyl sulfoxide N-methylpyrrolidone Oleic acid Urea

Figure 1.9: Chemical structures of some common chemical enhncers.

1.2.2.2 Nanoparticles

The rapid development of nanotechnology and increased demand for enhanced TDD have prompted extensive studies regarding the effect of nanoparticles in promoting skin permeation of drugs. Nanoparticles are thought to pass through skin via three different pathways: intracellular routes via corneocytes, intercellularly through the lipid matrix and through skin appendages like hair follicles **(Figure 1.10)** [81]. Several factors are reported to be influential on the penetration of nanoparticles through skin, including surface charge, hydrophilicity and particle size [82]. Positively charged nanoparticles are presented to have deeper penetration into skin as they can better interact with negatively charges skin surface in neutral pH [83]. Nanoparticles with an amphiphilic property penetrate deeper layers of skin as they can overcome the changing of hydrophilicity-hydrophobicity ratio in different layers of skin [81]. The most common nanoparticles used in TDD, depending on material composition, can be categorized into liposomes, solid-lipid nanoparticles (SLNs), polymeric micelles and inorganic nanoparticles [69].

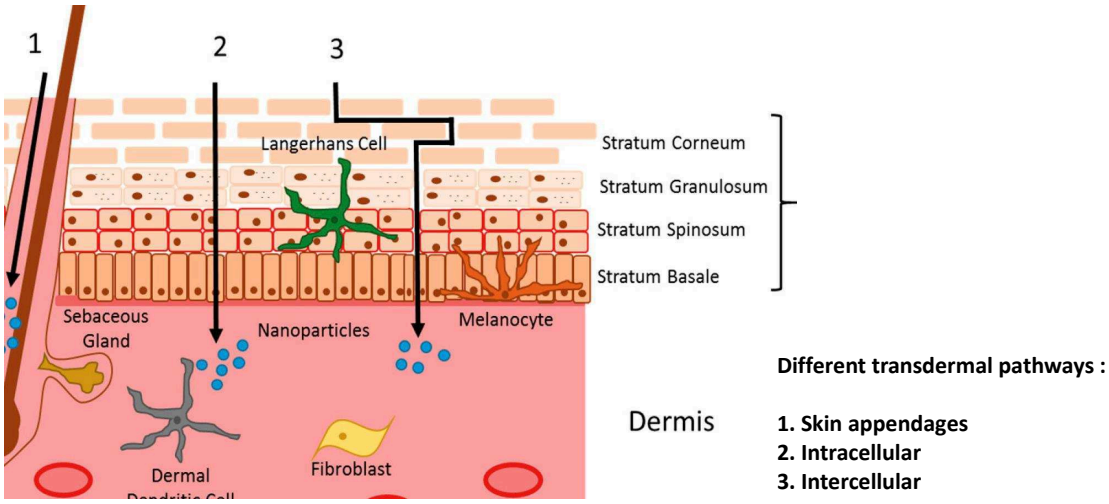

Figure 1.10: Three different pathways of nanoparticles enhanced TDD [84].

1.2.2.3 Sonophoresis

Sonophoresis is an active enhancing strategy in which ultrasound is used as a physical enhancer for TDD. Sonophoresis was first introduced into clinical application in 1950s. In 2004, the first ultrasound device for TDD was approved by FDA for the application of local dermal anesthesia of lidocaine [85]. Thermal effects and cavitations are believed to be the main mechanisms through which sonophoresis is enhancing TDD [86]. The increased temperature of skin, which is caused by absorbing ultrasound energy, results in an increase in diffusivity of the skin. Merino *et al.* showed that 35-fold increase in mannitol trandermal delivery was realized though sonophoresis that caused 20 °C increase in the skin temperature [87]. Cavitation effects refer to the collapse and oscillation of cavitation bubbles in the ultrasound field that may cause a mechanical impact on the skin structure, resulting in the increase of skin permeability [80]. To avoid extensive thermal damage of the skin, frequency and output power should be elaborately selected. Currently, most of the studies have been focus on using low-frequency ultrasound.

1.2.2.4 Electrical approaches

Electrical approaches, including iontophoresis and electroporation, are considered as effective enhancing strategies for TDD. Iontophoresis refers to apply a mild electric field onto skin to drive drugs across skin. It has been widely used to deliver agents for localized therapy, such as lidocaine delivery for local anesthesia and anti-inflammatory agents for local physical therapy [88, 90]. The main driving forces stem from electrophoresis and electroosmosis.

Electrophoresis is known to drive charged compounds by direct interaction with electric field, while electroosmosis is thought to increase drug permeation through electrically induced solvent flow [90]. In addition, transient increase in skin permeability induced by electric field also acts as minor mechanism. The therapeutic effect of iontophoresis is mainly affected by pH, current strength and density, drug concentration, as well as the charge of drugs [91]. Attributed to its fascinating characteristics, iontophoresis has been used to deliver both charged and non-charged molecules. However, molecules larger than 20kDa are limited through this method as delivery of macromolecules requires potent driving force, which may cause irreversible damage to skin [92]. In contrast, the process of electroporation involves application of high voltage for a short duration to create transient pores that can facilitate drug delivery. It has been shown to be effective in delivering both hydrophilic and macromolecular agents such as lidocaine, insulin and DNA [93-95]. However, the lack of quantitative delivery and bioactivity largely restrict its application.

1.2.2.5 Laser thermal ablation

Ablation of SC, the primary barrier that hinders drug permeation, is regarded as an effective means of enhancing strategy for TDD. Typical methods include mechanical ablation and chemical treatment, such as tape stripping and chemical enhancers. However, these tactics are always accompanied with skin irritation and acute pain, as well as lack of control and reproducibility [67]. Thermal ablation, a process in which SC is selectively removed by localized pulse heating, creates microchannels in skin for a wide range of drugs including macromolecules to pass through. As aforementioned, ultrasound and electricity are employed to cause thermal effect to facilitate drug penetration. However, these two strategies are turned out to be uncontrollable which may lead to a lack of reproducibility. As an alternative, laser is used to complement the setbacks as it is a highly concentrated light which can be tuned by changing the parameters such as irradiation time and power. Laser thermal ablation can be realized either through direct irradiation on skin or through photothermal effect generated by nanoparticles [96].

In the case of direct irradiation, human skin is heated up to hundreds of degrees by a laser for a very short period (micro- to milliseconds) to disrupt the SC while spare adjacent skin tissue from damaging. During the laser excitation, water is rapidly evaporated and micropores filled with exudate are formed (**Figure 1.11**) [97]. The pores act as channels through which drugs can pass through. The size and depth of the pores can be controlled through varying the power

or wavelength of laser. To date, many types of lasers have been explored, including ruby laser, neodymium:yttrium-aluminum-garnet (Nd:YAG) laser, alexandrite laser, carbon dioxide (CO_2) laser and erbium:yttrium-aluminum-garnet (Er:YAG) laser [96]. However only few of them are effective. For example, ruby laser and alexandrite laser, which display a wavelength of 694 nm and 755 nm respectively, show a very restricted effect on skin ablation as lights in NIR region (650-900 nm) are not absorbed by skin [98]. In contrast, far-infrared lasers, such as Er:YAG laser, cause a great increase of temperature in skin through water excitation and explosive evaporation from the epidermis, resulting in microporations of skin that increase drug permeation [99, 100]. Er:YAG laser has been utilized by Pantec Biosolutions to develop Precise Laser Epidermal System device (P.L.E.A.S.E.) for enhanced TDD.

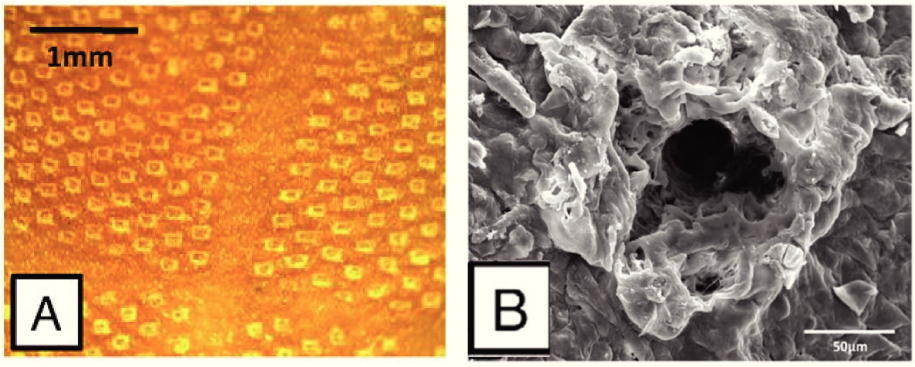

Figure 1.11: (A) Microporations formed on skin after laser ablation (B) SEM image of microporation [97].

Apart from direct laser irradiation, thermal ablation induced by photothermal effect in which laser power is absorbed by nanoparticles shows a promising application in TDD. The merits of laser and nanoparticles are integrated to further increase the effect of thermal ablation, the details are discussed in **Chapter 1.3**.

1.2.2.6 Microneedles

Microneedles (MNs) are among the most investigated means of strategies for enhanced TDD. MNs, an array of micro-sized needles that are ranging from 10 to 2000 µm in length, can puncture the epidermis layer of skin and thus lead to an enhanced delivery of both small and large molecules. Compared with hypodermic injection, the minimally invasive MNs offer painless drug delivery with better patient compliance. Since the first introduction by Gerstel and Place in drug delivery system in 1971, MNs have evolved into four different categories, namely solid, coated, dissolving and hollow MNs (**Figure 1.12**) [101]. Solid MNs are the first developed needles used in TDD. They are mostly employed to penetrate skin, followed by the

application of drugs. Drugs are able to diffuse through the holes that created by MNs piercing and finally reach blood stream [102]. To integrate the penetration and drug diffusion process, solid MNs are always coated with drugs that can be released when penetrating skin. Coated MNs also help to rapidly deliver desired dose of drug upon insertion into skin. However they are limited with the amount of drug that can be coated onto the needles [103]. In contrast to solid and coated MNs, dissolving MNs, fabricated from safe, inert and water soluble materials, act by releasing payload drugs through complete dissolution of needles, leaving no hazardous sharp waste. In the case of hollow MNs, the drug solution can be delivered either passively by diffusion or actively utilizing a pressure-driven flow through the needle lumen. As drug flow rate can be deliberately controlled by adjusting pressure, it offers a precise drug dosing delivery [104].

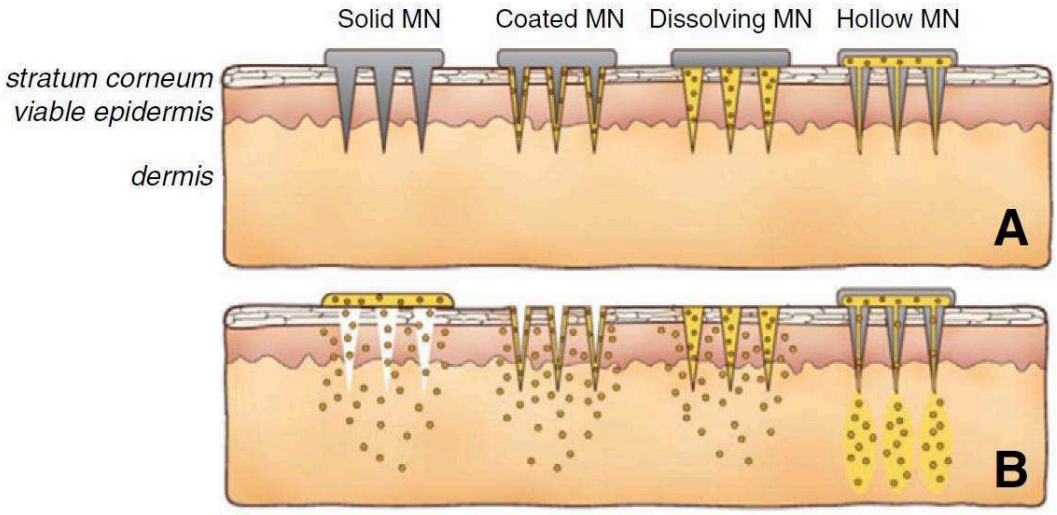

Figure 1.12: Working mechanisms of different types of MNs. (A) Penetration of stratum corneum with different MNs; (B) Drug release from applied MNs [103].

1.3 Heat-assisted antibacterial effect and enhanced TDD

Heat, as one of the major treatments in health care, has been applied in the treatments such as muscle spasms, myalgia, fibromyalgia, contracture and bursitis. Meanwhile, it offers the possibility in curing antibiotic-resistant bacterial infection and enhancing transdermal drug delivery. Heat causes hyperthermia to bacterial cells, which results in denaturation of protein, disruption of cell membrane structure and impediment of nucleic acid synthesis. Any temperature higher than 70 °C will cause an instant kill of bacteria. Heat can be applied in increasing transdermal drug release through disrupting the stratum corneum, increasing body fluid circulation and increasing blood vessel wall penetration [105]. However, in order to achieve targeted bacterial ablation and transdermal delivery with minimal side-effect, certain

strategies have to be elaborately taken. Based on nanostructured materials, we have conducted experiments through photothermal and electrothermal effect.

1.3.1 Photothermal antibacterial effect and enhanced TDD

Photothermal effect is a process in which materials are excited by light, resulting in the production of heat. Photothermal therapy (PTT) refers to employ this effect in clinical applications, including photothermal ablation of bacteria and enhanced TDD. To achieve directed and potent therapeutic effect, near infrared light (NIR) and nanomaterials are always involved in PTT attributed to their fascinating properties. NIR refers to the light with a wavelength of 700-2500 nm. In the application of PTT, the wavelength range of 700-1400 nm is always used as the absorption coefficient of water, lipid, deoxy- and hemoglobin (blood) are low in this region, thus leads to a deeper penetration of the light through the tissue without causing much damage [105]. Nanomaterials are the materials with a size ranging from 0 to 1000 nm. Due to the size effect, nanomaterials often display significantly large surface area per unit volume, which renders many unique behaviors and properties, including better opportunities for interactions with adjacent materials and facile surface modifications [106]. In addition, the nano-sized materials are able to reach biomolecules and microorganisms that shares similar size, such as DNA, virus and bacteria. These properties have fueled their use for nanodrugs, diagnostics, drug delivery [107].

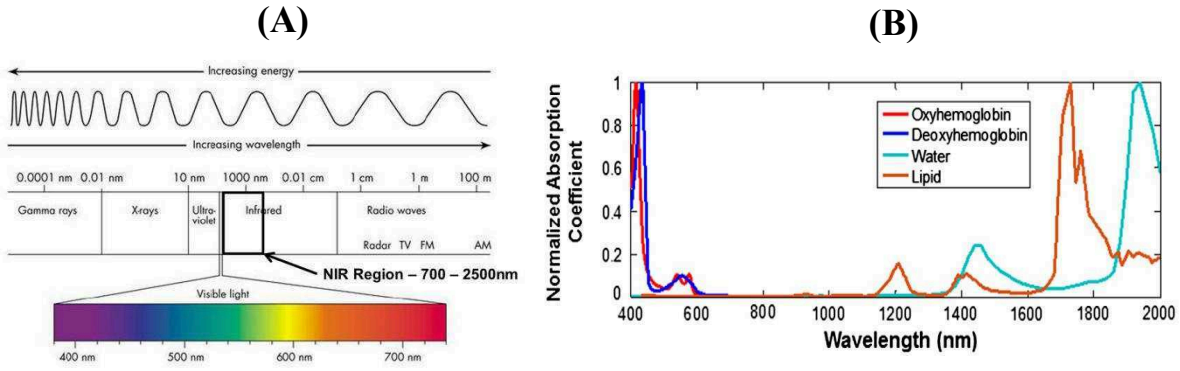

Figure 1.13: Characteristics of near infrared (NIR) light. (A) wavelength range of NIR light [108]; (B) absorption coefficient of oxyhemoglobin, deoxyhemoglobin, water and lipid in the region of visible and near infrared region[109].

In the case of PTT ablation of bacteria, the nanoagents are first introduced into the infection site, followed by the irradiation of NIR light. The activated nanomaterials can transfer heat to cause hyperthermal damage to bacterial cells and therefore lead to the inactivation of bacteria. As aforementioned, thermal ablation is an effective way for enhanced TDD. Recent

development in nanotechnology extended the application of thermal ablation in TDD as nanomaterials can be fine tailored to absorb NIR light, sparing normal tissues from thermal damage. In the meanwhile, the use of nanomaterials renders an integrated effect which could further increase the delivery. To date, various nanomaterials have been studied for photothermal ablation of bacteria and photothermal enhanced TDD.

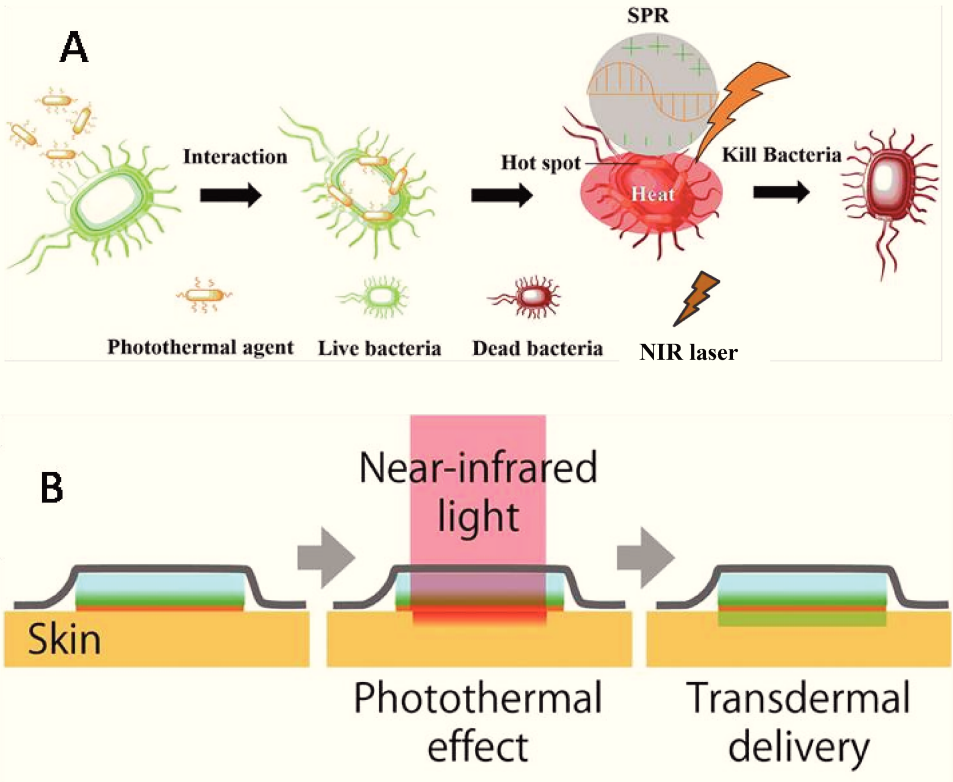

Figure 1.14: Schematic illustrations of (A) PTT ablation of bacteria with gold nanoparticles[51]; (B) PTT enhanced TDD using gold nanoparticles [110].

1.3.1.1 Gold nanoparticles

Gold nanoparticles are among the most explored PTT agents owing to their excellent chemical stability and Surface Plasmon Resonance (SPR) property. SPR effect, the oscillation of photo-activated conduction electrons at the surface of noble metal, can be efficiently transferred into heating by non-radiative relaxation through electron–phonon and subsequent phonon–phonon coupling processes [111]. Besides, the optical properties of gold nanoparticles are highly tunable depending on size and shape, which results in the development of different forms of particles for different PTT applications. Well-developed gold nanoparticles include Au nanospheres, Au nanorods (Au NRs), Au nanoshells and other forms of particles such as Au nanostars and Au nanodiscs. Au nanospheres strongly absorb light in visible region due to the coherent oscillations of the metal conduction band electrons

in strong resonance with visible frequencies of light [112]. Au nanospheres have been found in studies regarding PTT ablation of bacteria and enhanced TDD [113, 114]. However, the absorption and scattering of visible light by biological tissues usually limits the use of Au nanospheres. Unlike spherical particles, gold NRs display two absorption peaks, one corresponds to the short transversal axis while the other to the long longitudinal axis. The maximum longitudinal extinction band of Au NRs is very sensitive to the aspect ratio (length/width) [111], which can be fine-tuned to well adapt NIR triggered PTT. Owing to this fascinating property, Au NRs have been widely applied in both PTT bacteria ablation and enhanced TDD. For example, antibody conjugated Au NRs are reported by Norman and coworkers for targeted NIR ablation of *Pseudomonas aeruginosa* [115]. Tang *et al.* [78] performed protein TDD using ovalbumin as model drug based on gold NRs mediated continuous/pulsed PTT. Similarly, the absorption peak of Au nanoshells can be adjusted through modifying the thickness of the shell. They are utilized by Huang and coworkers in fabricating Fe_3O_4@SiO_2@Au hierarchical structure for NIR ablation of antibiotic-resistant bacteria [116].

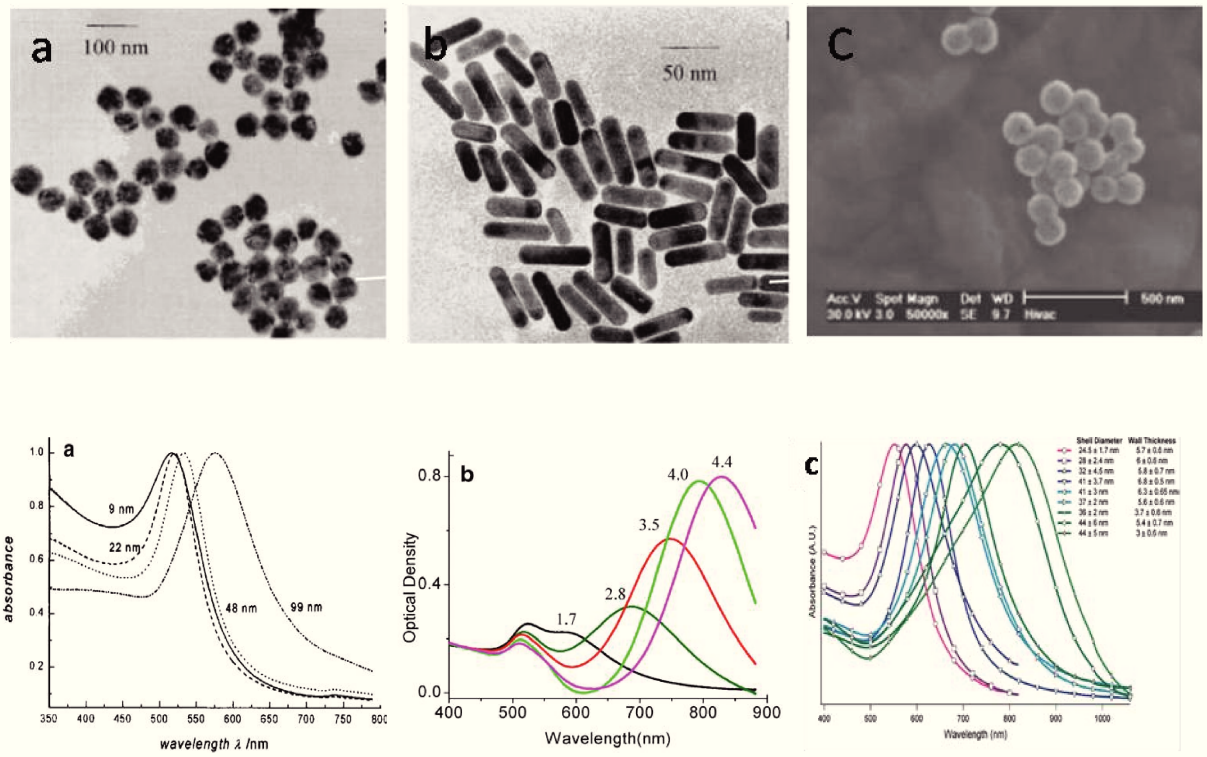

Figure 1.15: Morphological pictures and UV-Vis spectra of different gold nanostructures. (a) Gold nanospheres and UV-Vis spectra of Gold nanospheres with different sizes [117]; (b) Au NRs and UV-Vis spectra of Au NRs with different aspect ratios [118]; (c) Au shells and UV-Vis spectra of Au shells with different thicknesses [119, 120].

1.3.1.2 Carbon nanomaterials

Carbon nanostructures are being successfully employed in biological-related studies such as sensing, biomaterials, drug delivery, and antibacterial agents. The unique carbon bond architecture is able to form different nanostructures, including fullerenes, nanotubes, graphene and nanodiamond. When it comes to the application for PTT, carbon nanotubes and graphene are often referred. These materials are consisted of honey comb carbon skeletons formed by sp^2 bonding. The delocalized electrons on carbon sheet favor the NIR absorption, which subsequently leads to the vibrational mode of carbon atoms and results in a rise of temperature once the atoms recovered [121]. Carbon nanotubes are widely applied for PTT ablation of bacteria owing to their high binding affinity to bacterial cells and easy surface modifications [122]. Since 2007, when the first carbon nanotubes assisted PTT killing of bacteria was reported, various modified carbon nanotubes were demonstrated concerning targeted killing of bacteria. Moreover, the 1D structure of carbon nanotubes are able to penetrate biofilms and attach to the individual bacterial cell wall, resulting in a potent disruption of biofilm infections [123]. Inspired by the application of carbon nanotubes, graphene has also been developed as an PTT agent for bacterial disinfections. Unlike carbon nanotubes, the 2D structure of graphene offers a larger light converting surface area, as well as a better interaction with bacterial cells. Due to the facile and economical synthesizing process, reduced graphene oxide (rGO), a few layered carbon sheet with density of defects, are often reported. Furthermore, plenty of nanomaterials can be engineered onto graphene sheet to fabricate multifunctional nanocomposites. For example, magnetic reduced graphene oxide tethered with glutaraldehyde is reported by Meng-Chin *et al* [124]. For effective capture and PTT ablation of gram-positive and gram-negative bacteria. Results showed that bacteria could be effectively captured by the nanocomposites and later separated by external magnetic field. After applying NIR light for 10 min, 99% of the bacteria were killed by the heat generated by the photothermal effect. In the case of TDD, the large surface area of graphene can be used as an efficient drug vehicle, providing the possibility of PTT drug release and enhanced skin drug permeation. Based on this theory, our group recently reported a flexible rGO patch for efficient on-demand TDD of ondansetron, a medication used to prevent nausea and vomiting caused by motion sickness, through pork skin [125]. After 10 min irradiation with 980 nm laser at 5 W/cm^2 , a ondansetron flux rate of 1.6 $\mu g \cdot cm^{-2}\ h^{-1}$ was achieved. The use of tween 20, a chemical enhancer for TDD, further pushed the rate to 13.2 $\mu g \cdot cm^{-2}\ h^{-1}$ under the same laser irradiation. Similarly, in another study, rGO integrated hydrogel was

found to be able to transdermally deliver insulin through the skin [126]. The findings pave the road for controllable on-demand TDD using rGO based materials.

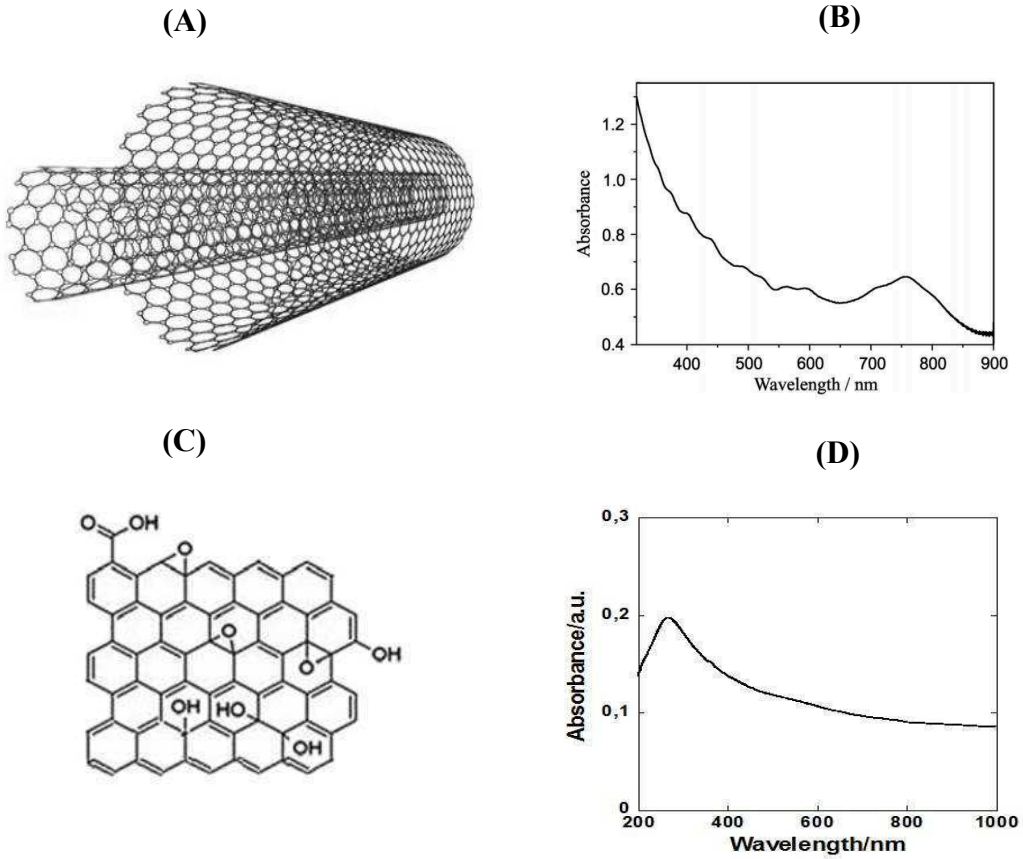

Figure 1.16: Structure of carbon nanomaterials and corresponding UV-Vis spectra. (A) Structure of carbon nanotubes [127]; (B) UV-Vis absorbance of carbon naotubes [128]; (C) Structure of reduced graphene oxide [129]; (D) UV-Vis absorbance of reduced graphene oxide.

1.3.1.3 Other nanoparticles

In addition to gold and carbon nanomaterials, many other NIR responsive and biocompatible nanomaterials have been developed. Copper sulfide (CuS) nanoparticles display a strong absorption in NIR region due to the d-d transition of Cu^{2+} ions. Compared with Gold nanoparticles, CuS exhibits advantages over its better photothermal stability and low cost. Owing to the excellent properties, CuS nanoparticles are emerging as a new type of photothermal therapeutic agent. Huang *et al* [130] presented a smart and green method in preparing CuS nanoparticles that are in situ grown on polymer template. After incorporating with cellulose nanofibers, the formed composite paper was applied for rapid wound infection healing. In the work of Ramadan and coworkers, hollow CuS nanoparticles were used for enhanced photothermal TDD of human growth hormone through nanosecond-pulsed laser irradiation [131]. Other semiconductive nanoparticles like silicon carbide (SiC) and Molybdenum disulfide (MoS_2) also show a good absorption of NIR light [51], which have

been applied in PTT antibacterial test and might have a potential in TDD application. In addition, as a metal-like plasmonic material, lanthanum hexaboride (LaB_6) exhibits comparable NIR absorption to gold nanoparticles. In the work of *Lai and Chen* [132], SiO_2 coated LaB_6 nanoparticles were modified with magnetic nanoparticles and Vancomycin for selectively magnetic separation and thermal ablation of bacteria. In the work of Chen *et al*. [133], the SiO_2 coated LaB_6 were integrated into microneedles for remote NIR triggered TDD of small molecules.

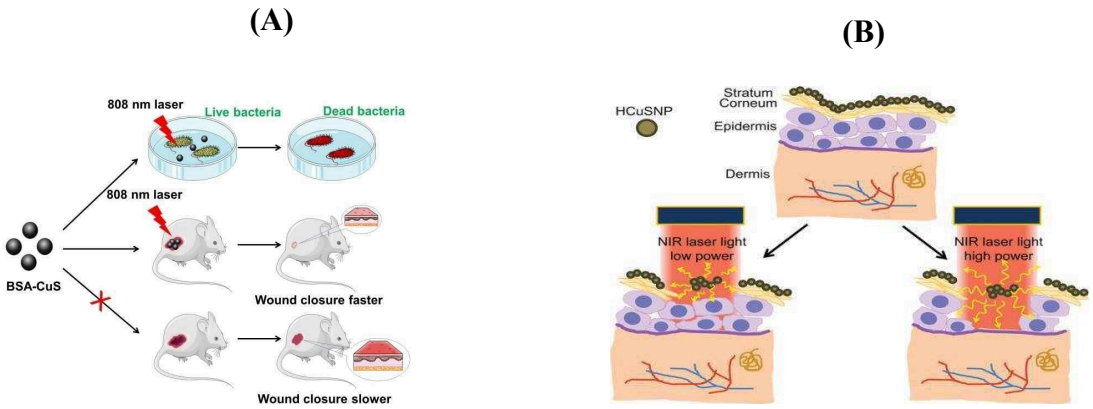

Figure 1.17: CuS nanoparticles for photothermal ablation of bacterial and photothermal enhanced TDD. (A) BSA coated CuS for NIR driven photothermal therapy of wound infection [134]; (B) Hollow CuS nanoparticles for Photothermal enahcend TDD [131].

1.4 Summary

In the first chapter, a general introduction is made on antibiotic resistance and transdermal drug release together with their corresponding solutions. Among the various strategies that can be taken, heat offers a solution for both of the problems. Photothermal heating is introduced in this chapter to achieve heat based treatment in both cases. By integrating the exceptional properties of NIR laser and nanomaterials, targeted photothermal bacterial ablation and controlled TDD can be achieved. Among different nanomaterials that have been developed, gold nanomaterials and carbon-based nanomaterials are drawing much attention owing to their outstanding photothermal properties. In this thesis, based on thesis two nanomaterials, studies on photothermal ablation of bacteria and enhanced transdermal drug delivery will be carried out.

1.5 References

[1] Kivlan, B. Arnheim's Principles of Athletic Training: A Competency-Based Approach,

11th Edition. Medicine & Science in Sports & Exercise. 2003: p. 370.

[2] Aminov, R.I.; Mackie, R.I., Evolution and ecology of antibiotic resistance genes. 2007: Oxford, UK. p. 147-161.

[3] Freire-Moran, L.; Aronsson, B.; Manz, C.; Gyssens, I.C.; So, A.D.; Monnet, D.L.; Cars, O. Critical shortage of new antibiotics in development against multidrug-resistant bacteria—Time to react is now. Drug Resistance Updates. 2011. 14(2): p. 118-124.

[4] Römling, U.; Balsalobre, C. Biofilm infections, their resilience to therapy and innovative treatment strategies. Journal of Internal Medicine. 2012. 272: p. 541-561.

[5] Prausnitz, M.R.; Langer, R. Transdermal drug delivery. Nature Biotechnology. 2008. 26(11): p. 1261-1268.

[6] Naik, A.; Kalia, Y.N.; Guy, R.H. Transdermal drug delivery: overcoming the skin's barrier function. Pharmaceutical Science & Technology Today. 2000. 3(9): p. 318-326.

[7] Rossiter, S.E.; Fletcher, M.H.; Wuest, W.M. Natural Products as Platforms To Overcome Antibiotic Resistance. Chemical Reviews. 2017. 117(19): p. 12415-12474.

[8] Park, J.T.; Uehara, T. How bacteria consume their own exoskeletons (turnover and recycling of cell wall peptidoglycan). Microbiology and Molecular Biology Reviews. 2008. 72(2): p. 211-227.

[9] Kapoor, G.; Saigal, S.; Elongavan, A. Action and resistance mechanisms of antibiotics: A guide for clinicians. Journal of Anaesthesiology Clinical Pharmacology. 2017. 33(3): p. 300-305.

[10] Aldred, K.J.; Kerns, R.J.; Osheroff, N. Mechanism of quinolone action and resistance. Biochemistry. 2014. 53(10): p. 1565-1574.

[11] Yoneyama, H.; Katsumata, R. Antibiotic Resistance in Bacteria and Its Future for Novel Antibiotic Development. Bioscience, Biotechnology, and Biochemistry. 2006. 70(5): p. 1060-1075.

[12] Chopra, I.; Roberts, M. Tetracycline antibiotics: mode of action, applications, molecular biology, and epidemiology of bacterial resistance. Microbiology and Molecular Biology Reviews. 2001. 65(2): p. 232-60 ; second page, table of contents.

[13] Lin, J.; Nishino, K.; Roberts, M.C.; Tolmasky, M.; Aminov, R.I.; Zhang, L. Mechanisms of antibiotic resistance. Frontiers in Microbiology. 2015. 6: p. 34.

[14] Blair, J.M.A.; Webber, M.A.; Baylay, A.J.; Ogbolu, D.O.; Piddock, L.J.V. Molecular mechanisms of antibiotic resistance. Nature Reviews Microbiology. 2014. 13: p. 42.

[15] Tängdén, T.; Adler, M.; Cars, O.; Sandegren, L.; Löwdin, E. Frequent emergence of porin-deficient subpopulations with reduced carbapenem susceptibility in ESBL-producing during exposure to ertapenem in an pharmacokinetic model. Journal of Antimicrobial Chemotherapy. 2013. 68(6): p. 1319-1326.

[16] Singh, R.; Smitha, M.S.; Singh, S.P. The Role of Nanotechnology in Combating Multi-Drug Resistant Bacteria. Journal of Nanoscience and Nanotechnology. 2014. 14(7): p. 4745-4756.

[17] Wright, G.D. Molecular mechanisms of antibiotic resistance. Chemical Communications. 2011. 47(14): p. 4055-4061.

[18] Munita, J.M.; Arias, C.A. Mechanisms of Antibiotic Resistance. Microbiology spectrum. 2016. 4(2): p. 10.1128/microbiolspec.VMBF-0016-2015.

[19] Drawz, S.; Bonomo, R. Three Decades of β-Lactamase Inhibitors. Clinical Microbiology Reviews. 2010. 23(1): p. 160-201.

[20] Centers for Disease Control and Prevention. Antibiotic Resistance Threats in the United States. 2013; Available from: http://www.cdc.gov/drugresistance/threat-report-2013/pdf/ar-threats-2013-508.pdf.

[21] World Health Organisation (WHO), Antimicrobial Resistance: Global Report on Surveillance. 2014; Available from:

http://www.who.int/drugresistance/documents/surveillancereport/en/.

[22] Michael, C.A.; Dominey-Howes, D.; Labbate, M. The antimicrobial resistance crisis: causes, consequences, and management. Frontier Public Health. 2014. 2: 145.

[23] Spellberg, B.; Gilbert, D.N. The future of antibiotics and resistance: a tribute to a career of leadership by John Bartlett. Clinical Infectious Diseases. 2014. 59 Suppl 2: p. 71-75.

[24] Ventola, C.L. The antibiotic resistance crisis: part 1: causes and threats. P & T : a peer-reviewed journal for formulary management. 2015. 40(4): p. 277-283.

[25] Van Boeckel, T.P.; Gandra, S.; Ashok, A.; Caudron, Q.; Grenfell, B.T.; Levin, S.A.; Laxminarayan, R. Global antibiotic consumption 2000 to 2010: an analysis of national pharmaceutical sales data. The Lancet Infectious Diseases. 2014. 14(8): p. 742-750.

[26] Golkar, Z.; Bagasra, O.; Pace, D.G. Bacteriophage therapy: a potential solution for the antibiotic resistance crisis. The Journal of Infection in Developing Countries. 2014. 8: p. 129-136.

[27] Smith, R.D.; Keogh-Brown, M.R.; Barnett, T. Estimating the economic impact of pandemic influenza: An application of the computable general equilibrium model to the UK. Social Science & Medicine. 2011. 73(2): p. 235-244.

[28] Bartlett, J.G.; Gilbert, D.N.; Spellberg, B. Seven ways to preserve the miracle of antibiotics. Clinical Infectious Diseases. 2013. 56(10): p. 1445-50.

[29] Gross, M. Antibiotics in crisis. Current Biology. 2013. 23(24): p. R1063-R1065.

[30] Rasko, D.A.; Sperandio, V. Anti-virulence strategies to combat bacteria-mediated disease. Nature Reviews Drug Discovery. 2010. 9(2): p. 117-128.

[31] Marston, H.D.; Dixon, D.M.; Knisely, J.M.; Palmore, T.N.; Fauci, A.S. Antimicrobial Resistance. JAMA. 2016. 316(11): p. 1193-1204.

[32] Bassegoda, A.; Ivanova, K.; Ramon, E.; Tzanov, T. Strategies to prevent the occurrence of resistance against antibiotics by using advanced materials. Applied Microbiology and Biotechnology. 2018. 102(5): p. 2075-2089.

[33] Kalia, V.C. Quorum sensing inhibitors: an overview. Biotechnology Advances. 2013. 31(2): p. 224-245.

[34] Chen, J.; Wang, F.; Liu, Q.; Du, J. Antibacterial polymeric nanostructures for biomedical applications. Chemical Communications. 2014. 50(93): p. 14482-14493.

[35] Fernanda, E.; Nathália, E.; Patrícia, E.; Lorena, E.; Ildinete, E.-P.; Cynthia, E. Antimicrobial development challenges: the various mechanisms of action of antimicrobial peptides and of bacterial resistance. Frontiers in Microbiology. 2013. 4: 353.

[36] Mahlapuu, M.; Håkansson, J.; Ringstad, L.; Björn, C. Antimicrobial Peptides: An Emerging Category of Therapeutic Agents. Frontiers in Cellular and Infection Microbiology. 2016. 6: 194

[37] Gomes, B.; Augusto, M.T.; Felício, M.R.; Hollmann, A.; Franco, O.L.; Gonçalves, Sónia.; Santos, Nuno C. Designing improved active peptides for therapeutic approaches against infectious diseases. 2018. 36(2): p. 415-429

[38] Sharma, A.; Kumar Arya, D.; Dua, M.; Chhatwal, G.S.; Johri, A.K. Nano-technology for targeted drug delivery to combat antibiotic resistance. Expert Opinion on Drug Delivery 2012. 9(11): p. 1325-1332.

[39] Beyth, N.; Houri-Haddad, Y.; Domb, A.; Khan, W.; Hazan, R. Alternative antimicrobial approach: nano-antimicrobial materials. Evidence-Based Complementary and Alternative Medicine. 2015: p. 1-16.

[40] Besinis, A.; De Peralta, T.; Handy, R.D. The antibacterial effects of silver, titanium dioxide and silica dioxide nanoparticles compared to the dental disinfectant chlorhexidine on Streptococcus mutans using a suite of bioassays. Nanotoxicology. 2014. 8(1): p. 1-16.

[41] Dayem, AA.; Hossain, Mk.; Lee, SB.; Kim, K.; Saha, Sk.; Yang, Gm.; Choi, Hy.; Cho, SG. The Role of Reactive Oxygen Species (ROS) in the Biological Activities of Metallic Nanoparticles. International Journal Of Molecular Sciences. 2017. 18(1)

[42] Mohammadi, G.; Valizadeh, H.; Barzegar-Jalali, M.; Lotfipour, F.; Adibkia, K.; Milani, M.; Azhdarzadeh, M.; Kiafar, F.; Nokhodchi, A. Development of azithromycin-PLGA nanoparticles: physicochemical characterization and antibacterial effect against Salmonella typhi. Colloids and Surfaces B: Biointerfaces. 2010. 80(1): p. 34-39.

[43] Seil, J.T.; Webster, T.J. Antimicrobial applications of nanotechnology: methods and literature. International Journal of Nanomedicine. 2012. 7: p. 2767-2781.

[44] Dizaj, S.M.; Lotfipour, F.; Barzegar-Jalali, M.; Zarrintan, M.H.; Adibkia, K. Antimicrobial activity of the metals and metal oxide nanoparticles. Materials Science and Engineering: C. 2014. 44: p. 278-284.

[45] Berdy, J. Thoughts and facts about antibiotics: where we are now and where we are heading. The Journal of Antibiotics. 2012. 65(8): p. 385-395.

[46] Zhang, L.; Fx, G.; Jm, C.; Az, W.; Rs, L.; Oc, F. Nanoparticles in Medicine: Therapeutic Applications and Developments. Clinical Pharmacology & Therapeutics. 2007. 83(5): p. 761-769.

[47] Zhang, L.; Pornpattananangku D Fau - Hu, C.M.J.; Hu Cm Fau - Huang, C.M.; Huang, C.M. Development of nanoparticles for antimicrobial drug delivery. Current Medicinal Chemistry. 2010;17(6):585-594.

[48] Fayaz, A.M.; Balaji, K.; Girilal, M.; Yadav, R.; Kalaichelvan, P.T.; Venketesan, R. Biogenic synthesis of silver nanoparticles and their synergistic effect with antibiotics: a study against gram-positive and gram-negative bacteria. Nanomedicine: Nanotechnology, Biology and Medicine. 2010. 6(1): p. 103-109.

[49] Kohanski, M.A.; Dwyer, D.J.; Collins, J.J. How antibiotics kill bacteria: from targets to networks. Nature Reviews Microbiology. 2010. 8(6): p. 423-435.

[50] Li, P.; Li, J.; Wu, C.; Wu, Q.; Li, J. Synergistic antibacterial effects of β-lactam antibiotic combined with silver nanoparticles. Nanotechnology. 2005. 16(9): p. 1912-1917.

[51] Feng, Y.; Liu, L.; Zhang, J.; Aslan, H.; Dong, M. Photoactive antimicrobial nanomaterials. Journal of Materials Chemistry B. 2017. 5(44): p. 8631-8652.

[52] Gao, W.; Thamphiwatana, S.; Angsantikul, P.; Zhang, L. Nanoparticle approaches against bacterial infections. Wiley Interdiscip Rev Nanomed Nanobiotechnol. 2014. 6(6): p. 532-547.

[53] Pornpattananangkul, D.; Olson, S.; Aryal, S.; Sartor, M.; Huang, C.-M.; Vecchio, K.; Zhang, L. Stimuli-Responsive Liposome Fusion Mediated by Gold Nanoparticles. ACS nano. 2010. 4(4): p. 1935-1942.

[54] Komnatnyy, V.V.; Chiang, W.C.; Tolker-Nielsen, T.; Givskov, M.; Nielsen, T.E. Bacteria-triggered release of antimicrobial agents. Angewandte Chemie International Edition. 2014. 53(2): p. 439-441.

[55] Geilich, B.M.; Gelfat, I.; Sridhar, S.; van de Ven, A.L.; Webster, T.J. Superparamagnetic iron oxide-encapsulating polymersome nanocarriers for biofilm eradication. Biomaterials. 2017. 119: p. 78-85.

[56] Halouane, F.; Jijie, R.; Meziane, D.; Li, C.; Singh, S.K.; Bouckaert, J.; Jurazek, J.; Kurungot, S.; Barras, A.; Li, M.; Boukherroub, R.; Szunerits, S. Selective isolation and eradication of E. coli associated with urinary tract infections using anti-fimbrial modified magnetic reduced graphene oxide nanoheaters. Journal of Materials Chemistry B. 2017. 5(40): p. 8133-8142.

[57] Mohammad, A.; Hasan, M.; David, R.B. Differential Role of Reactive Oxygen Intermediates in Photofrin-I- and Photofrin-II-Mediated Photoenhancement of Lipid Peroxidation in Epidermal Microsomal Membranes. Journal of Investigative Dermatology. 1988. 90(5): p. 652-657.

[58] Redmond, R.W.; Gamlin, J.N. A compilation of singlet oxygen yields from biologically relevant molecules. Journal of Photochemistry and Photobiology. 1999. 70(4): p. 391 – 475.

[59] Hamblin, M.R.; Hasan, T. Photodynamic therapy: a new antimicrobial approach to infectious disease? Photochemical & Photobiological Sciences. 2004. 3(5): p. 436-450.

[60] Fu, X.-J.; Fang, Y.; Yao, M. Antimicrobial Photodynamic Therapy for Methicillin-Resistant Staphylococcus aureus Infection. BioMed Research International. 2013: p. 159-157.

[61] Garland, M.J.; Cassidy, C.M.; Woolfson, D.; Donnelly, R.F. Designing photosensitizers for photodynamic therapy: strategies, challenges and promising developments. Future medicinal chemistry. 2009. 1(4): p. 667-691.

[62] Managa, M.; Nyokong, T. Photodynamic antimicrobial chemotherapy activity of gallium tetra-(4-carboxyphenyl) porphyrin when conjugated to differently shaped platinum nanoparticles. Journal of Molecular Structure. 2015. 1099: p. 432-440.

[63] Nakonieczna, J.; Rapacka-Zdonczyk, A.; Kawiak, A.; Bielawski, K.P.; Grinholc, M. Sub-lethal photodynamic inactivation renders Staphylococcus aureus susceptible to silver nanoparticles. Photochemical & Photobiological Sciences. 2013. 12(9): p. 1622-1627.

[64] Tawfik, A.A.; Alsharnoubi, J.; Morsy, M. Photodynamic antibacterial enhanced effect of methylene blue-gold nanoparticles conjugate on Staphylococcal aureus isolated from impetigo lesions in vitro study. Photodiagnosis and Photodynamic Therapy. 2015.12(2): p. 215-220.

[65] Michaels, A.S.; Chandrasekaran, S.K.; Shaw, J.E. Drug permeation through human skin: Theory and invitro experimental measurement. AIChE Journal. 1975. 21(5): p. 985-996.

[66] Prausnitz, M.R.; Mitragotri, S.; Langer, R. Current status and future potential of transdermal drug delivery. Nature Reviews Drug Discovery. 2004. 3(2): p. 115-124.

[67] Szunerits, S.; Boukherroub, R. Heat: A Highly Efficient Skin Enhancer for Transdermal Drug Delivery. Frontiers in Bioengineering and Biotechnology. 2018. 6: 15.

[68] Schoellhammer, C.M.; Blankschtein D Fau - Langer, R.; Langer, R. Skin permeabilization for transdermal drug delivery: recent advances and future prospects.

Expert Opinion on Drug Delivery. 2014. 11(3): p. 393-407.

[69] Jijie, R.; Barras, A.; Boukherroub, R.; Szunerits, S. Nanomaterials for transdermal drug delivery: beyond the state of the art of liposomal structures. Journal of Materials Chemistry B. 2017. 5(44): p. 8653-8675.

[70] Lee, J.W.; Gadiraju, P.; Park, J.H.; Allen, M.G.; Prausnitz, M.R. Microsecond thermal ablation of skin for transdermal drug delivery. Journal of Controlled Release. 2011. 154(1): p. 58-68.

[71] Azagury, A.; Khoury, L.; Enden, G.; Kost, J. Ultrasound mediated transdermal drug delivery. Advanced Drug Delivery Reviews. 2014. 72: p. 127-143.

[72] Mitragotri, S. Devices for overcoming biological barriers: the use of physical forces to disrupt the barriers. Advanced Drug Delivery Reviews. 2013. 65(1): p. 100-103.

[73] Zhang, D.; Rielly Cd Fau - Das, D.B.; Das, D.B. Microneedle-assisted microparticle delivery by gene guns: experiments and modeling on the effects of particle characteristics. Drug Delivery. 2015. 22(3): p. 335-350.

[74] Alkilani, A.Z.; McCrudden, M.T.; Donnelly, R.F. Transdermal Drug Delivery: Innovative Pharmaceutical Developments Based on Disruption of the Barrier Properties of the stratum corneum. Pharmaceutics. 2015. 7(4): p. 438-470.

[75] Zaborski, C. Why are liposomes so good for the skin? 2017; Available from: http://spacanada.ca/liposomes-good-skin/.

[76] Available from: https://thetopiarysalon.co.uk/tried-amazing-new-facial/sonophoresis/.

[77] Iontophoresis. Available from:
https://www.slideshare.net/mallikarjuna2055/penetration-enhancers.

[78] Tang, H.; Kobayashi, H.; Niidome, Y.; Mori, T.; Katayama, Y.; Niidome, T. CW/pulsed NIR irradiation of gold nanorods: effect on transdermal protein delivery mediated by photothermal ablation. Journal of Controlled Release. 2013. 171(2): p. 178-83.

[79] Microneedles. Available from: http://www.karplab.net/wp-content/uploads/Parasite-Inspired-Adhesive-Patch.jpg.

[80] Inayat Bashir Pathan, C.M.S. Chemical Penetration Enhancers for Transdermal. Tropical Journal of Pharmaceutical Research. 2009. 8(2): p. 173-179.

[81] Biancamaria, B.; Maria Grazia, E.; Felice, L.; Michela, I.; Raimondo, P.; López-Quintela, M.A. Penetration of Metallic Nanoparticles in Human Full-Thickness Skin. Journal of Investigative Dermatology. 2007. 127(7): p. 1701-1712.

[82] Wang, M.; Marepally, S.K.; Vemula, P.K.; Xu, C. Chapter 5 - Inorganic Nanoparticles for Transdermal Drug Delivery and Topical Application, in Nanoscience in Dermatology, M.R. Hamblin, P. Avci, and T.W. Prow, Editors. 2016, Academic Press: Boston. p. 57-72.

[83] Ryman-Rasmussen, J.P.; Riviere, J.E.; Monteiro-Riviere, N.A. Penetration of intact skin by quantum dots with diverse physicochemical properties. Toxicological Science. 2006. 96(1): p. 159-165.

[84] Palmer, B.C.; DeLouise, L.A. Nanoparticle-Enabled Transdermal Drug Delivery Systems for Enhanced Dose Control and Tissue Targeting. Molecules. 2016. 21(12).

[85] Sontra Medical Receives FDA Clearance for SonoPrep(R) Skin Permeation Device and Procedure Tray for Use with Topical Lidocaine. PR Newswire 2004: p. 1.

[86] Park, D.; Park, H.; Seo, J.; Lee, S. Sonophoresis in transdermal drug deliverys. Ultrasonics. 2014. 54(1): p. 56-65.

[87] Merino, G.; Kalia, Y.N.; Delgado-Charro, M.B.; Potts, R.O.; Guy, R.H. Frequency and

thermal effects on the enhancement of transdermal transport by sonophoresis. Journal of Controlled Release. 2003. 88(1): p. 85-94.

[88] Costello, C.T.; Jeske, A.H. Iontophoresis: applications in transdermal medication delivery. Physical therapy. 1995. 75: p. 554-563.

[89] Miller, K.A.; Balakrishnan G Fau - Eichbauer, G.; Eichbauer G Fau - Betley, K.; Betley, K. 1% lidocaine injection, EMLA cream, or "numby stuff" for topical analgesia associated with peripheral intravenous cannulation. AANA Journal. 2001. 69: p. 185-187.

[90] Rawat, S.; Vengurlekar, S.; Rakesh, B.; Jain, S.; Srikarti, G. Transdermal Delivery by Iontophoresis. Indian Journal of Pharmaceutical Sciences. 2008. 70(1): p. 5-10.

[91] Wang, Y.; Thakur, R.; Fan, Q.; Michniak, B. Transdermal iontophoresis: combination strategies to improve transdermal iontophoretic drug delivery. European Journal of Pharmaceutics and Biopharmaceutics. 2005. 60(2): p. 179-91.

[92] Tokumoto, S.; Higo, N.; Sugibayashi, K. Effect of electroporation and pH on the iontophoretic transdermal delivery of human insulin. International Journal of Pharmaceutics. 2006. 326(1): p. 13-19.

[93] Murthy, S.N.; Zhao, Y.L.; Marlan, K.; Hui, S.W.; Kazim, A.L.; Sen, A. Lipid and electroosmosis enhanced transdermal delivery of insulin by electroporation. Journal of Pharmaceutical Sciences. 2006. 95(9): p. 2041-2050.

[94] Wallace, M.S.; Ridgeway, B.; Jun, E.; Schulteis, G.; Rabussay, D.; Zhang, L. Topical delivery of lidocaine in healthy volunteers by electroporation, electroincorporation, or iontophoresis: An evaluation of skin anesthesia. Regional Anesthesia and Pain Medicine. 2001. 26(3): p. 229-238.

[95] Lin, F.; Shen, X.; McCoy, J.R.; Mendoza, J.M.; Yan, J.; Kemmerrer, S.V.; Khan, A.S.; Weiner, D.B.; Broderick, K.E.; Sardesai, N.Y. A novel prototype device for electroporation-enhanced DNA vaccine delivery simultaneously to both skin and muscle. Vaccine. 2011. 29(39): p. 6771-6780.

[96] Li, Y.; Guo, L.; Lu, W. Laser ablation-enhanced transdermal drug delivery. Photonics & Lasers in Medicine. 2013. 2(4).

[97] Weiss, R.; Hessenberger, M.; Kitzmuller, S.; Bach, D.; Weinberger, E.E.; Krautgartner, W.D.; Hauser-Kronberger, C.; Malissen, B.; Boehler, C.; Kalia, Y.N.; Thalhamer, J.; Scheiblhofer, S. Transcutaneous vaccination via laser microporation. Journal of Controlled Release. 2012. 162(2): p. 391-399.

[98] Weissleder, R. A clearer vision for in vivo imaging. Nature Biotechnology. 2001. 19: p. 316.

[99] Hohenleutner, U.; Hohenleutner, S.; Bäumler, W.; Landthaler, M. Fast and effective skin ablation with an Er:YAG laser: Determination of ablation rates and thermal damage zones. Lasers in Surgery and Medicine. 1997. 20(3): p. 242-247.

[100] Kaufmann, R.; Beier, C. Laser Skin Ablation: An Update on Aesthetic and Medical Indications. Medical Laser Application. 2004. 19(4): p. 212-222.

[101] Indermun, S.; Luttge, R.; Choonara, Y.E.; Kumar, P.; du Toit, L.C.; Modi, G.; Pillay, V. Current advances in the fabrication of microneedles for transdermal delivery. Journal of Controlled Release. 2014. 185: p. 130-138.

[102] Hao, Y.; Li, W.; Zhou, X.; Yang, F.; Qian, Z. Microneedles-Based Transdermal Drug Delivery Systems: A Review. Journal of Biomedical Nanotechnology. 2017. 13(12): p. 1581-1597.

[103] Kim, Y.C.; Park, J.H.; Prausnitz, M.R. Microneedles for drug and vaccine delivery.

Advanced Drug Delivery Reviews. 2012. 64(14): p. 1547-68.

[104] Ita, K. Ceramic microneedles and hollow microneedles for transdermal drug delivery: Two decades of research. Journal of Drug Delivery Science and Technology. 2018. 44: p. 314-322.

[105] Zeng, H.; Du, X.-W.; Singh, S.C.; Kulinich, S.A.; Yang, S.; He, J.; Cai, W. Nanomaterials via Laser Ablation/Irradiation in Liquid: A Review. Advanced Functional Materials. 2012. 22(7): p. 1333-1353.

[106] Krishnan, S.; Diagaradjane, P.; Cho, S.H. Nanoparticle-mediated thermal therapy: evolving strategies for prostate cancer therapy. International Journal of Hyperthermia. 2010. 26(8): p. 775-789.

[107] Thomas Tumillo, A.R., Sahana Pentyala, Pooja Mysore, and Srinivas N. Pentyala. Nanomaterials in Healthcare. Translational Research in Environmental and Occupational Stress. 2014: p. 57-68.

[108] https://www.processsensors.com/whats-new/blog/near-infrared-measurements-how-do-they-work.

[109] Wilson, RH.; Nadeau, Kp.; Jaworski, Fb.; Tromberg, Bj.; Durkin, Aj.Review of short-wave infrared spectroscopy and imaging methods for biological tissue characterization. Journal Of Biomedical Optics. 2015, 20(3)

[110] Haine, A.T.; Koga, Y.; Hashimoto, Y.; Higashi, T.; Motoyama, K.; Arima, H.; Niidome, T. Enhancement of transdermal protein delivery by photothermal effect of gold nanorods coated on polysaccharide-based hydrogel. European Journal of Pharmaceutics and Biopharmaceutics. 2017. 119: p. 91-95.

[111] Dickerson, E.B.; Dreaden, E.C.; Huang, X.; El-Sayed, I.H.; Chu, H.; Pushpanketh, S.; McDonald, J.F.; El-Sayed, M.A. Gold nanorod assisted near-infrared plasmonic photothermal therapy (PPTT) of squamous cell carcinoma in mice. Cancer Letters. 2008. 269(1): p. 57-66.

[112] Huang, X.; Jain Pk Fau - El-Sayed, I.H.; El-Sayed Ih Fau - El-Sayed, M.A.; El-Sayed, M.A. Plasmonic photothermal therapy (PPTT) using gold nanoparticles. Lasers in Medical Science. 2008. 23(3): p. 217-228.

[113] Zharov, V.P.; Mercer Ke Fau - Galitovskaya, E.N.; Galitovskaya En Fau - Smeltzer, M.S.; Smeltzer, M.S. Photothermal nanotherapeutics and nanodiagnostics for selective killing of bacteria targeted with gold nanoparticles. Biophysical Journal. 2006. 90(2): p. 619-627.

[114] Kim, Y.J.; Kim, B.; Kim, J.W.; Nam, G.; Jang, H.S.; Kang, S.W.; Jeong, U. Combination of nanoparticles with photothermal effects and phase-change material enhances the non-invasive transdermal delivery of drugs. Colloids and Surfaces B: Biointerfaces. 2015. 135: p. 324-331.

[115] Norman, R.S.; Stone, J.W.; Gole, A.; Murphy, C.J.; Sabo-Attwood, T.L. Targeted photothermal lysis of the pathogenic bacteria, Pseudomonas aeruginosa, with gold nanorods. Nano Letters. 2008. 8(1): p. 302-306.

[116] Huang, W.C.; Tsai P.J.; Chen, Y.C. Multifunctional Fe3O4@Au nanoeggs as photothermal agents for selective killing of nosocomial and antibiotic-resistant bacteria. Small. 2009. 5(1): p. 51-56.

[117] Link, S.; El-Sayed, M. Size and temperature dependenceof the plasmon absorption of colloidal gold nanoparticles. The Journal of Physical Chemistry B. 1999. 103: p. 4212-4217.

[118] Nikoobakht, B.; El-Sayed, M.A. Preparation and Growth Mechanism of Gold

Nanorods (NRs) Using Seed-Mediated Growth Method. Chemistry of Materials. 2003. 15(10): p. 1957-1962.

[119] Loo, C.; Lin A Fau - Hirsch, L.; Hirsch L Fau - Lee, M.-H.; Lee Mh Fau - Barton, J.; Barton J Fau - Halas, N.; Halas N Fau - West, J.; West J Fau - Drezek, R.; Drezek, R. Nanoshell-enabled photonics-based imaging and therapy of cancer. Technology in Cancer Research & Treatment. 2004. 3(1): p. 33-40.

[120] Young, J.K.; Figueroa, E.R.; Drezek, R.A. Tunable nanostructures as photothermal theranostic agents. Annals of Biomedical Engineering. 2012. 40(2): p. 438-59.

[121] Akhavan, O.; Ghaderi, E.; Aghayee, S.; Fereydooni, Y.; Talebi, A. The use of a glucose-reduced graphene oxide suspension for photothermal cancer therapy. Journal of Materials Chemistry. 2012. 22(27): p. 13773-13781.

[122] Jose´ A. Rojas-Chapana; Miguel A. Correa-Duarte; Zhifeng Ren; Krzysztof Kempa; Giersig, M. Enhanced Introduction of Gold Nanoparticles into Vital Acidothiobacillus ferrooxidans by Carbon Nanotube-based Microwave Electroporation. Nano Letters. 2004. 4(5): p. 985-988.

[123] Levi-Polyachenko, N.; Young, C.; MacNeill, C.; Braden, A.; Argenta, L.; Reid, S. Eradicating group A streptococcus bacteria and biofilms using functionalised multi-wall carbon nanotubes. International Journal of Hyperthermia. 2014. 30(7): p. 490-501.

[124] Meng-Chin Wu; Archana R. Deokar; Jhan-Hong Liao; Po-Yuan Shih; Ling, Y.-C. Graphene-Based Photothermal Agent for rapid and effective killing of bacteria. ACS Nano. 2013. 7(2): p. 1281-1290.

[125] Teodorescu, F.; Queniat, G.; Foulon, C.; Lecoeur, M.; Barras, A.; Boulahneche, S.; Medjram, M.S.; Hubert, T.; Abderrahmani, A.; Boukherroub, R.; Szunerits, S. Transdermal skin patch based on reduced graphene oxide: A new approach for photothermal triggered permeation of ondansetron across porcine skin. Journal of Controlled Release. 2017. 245: p. 137-146.

[126] Teodorescu, F.; Oz, Y.; Queniat, G.; Abderrahmani, A.; Foulon, C.; Lecoeur, M.; Sanyal, R.; Sanyal, A.; Boukherroub, R.; Szunerits, S. Photothermally triggered on-demand insulin release from reduced graphene oxide modified hydrogels. Journal of Controlled Release. 2017. 246: p. 164-173.

[127] Ibrahim, K.S. Carbon nanotubes-properties and applications: a review. Carbon letters. 2013. 14(3): p. 131-144.

[128] Mikheev, K.G.; Saushin, A.S.; Zonov, R.G.; Nasibulin, A.G.; Mikheev, G.M. Photon-drag in single-walled carbon nanotube and silver-palladium films: the effect of polarization. Journal of Nanophotonics. 2015. 10(1).

[129] Rella, S.; Giuri, A.; Corcione, C.E.; Acocella, M.R.; Colella, S.; Guerra, G.; Listorti, A.; Rizzo, A.; Malitesta, C. X-ray photoelectron spectroscopy of reduced graphene oxide prepared by a novel green method. Vacuum. 2015. 119: p. 159-162.

[130] Huang, X.; Hu, N.; Wang, X.; Zhang, Y.S.; Sun, R. Copper Sulfide Nanoparticle/Cellulose Composite Paper: Room-Temperature Green Fabrication for NIR Laser-Inducible Ablation of Pathogenic Microorganisms. ACS Sustainable Chemistry & Engineering. 2017. 5(3): p. 2648-2655.

[131] Ramadan, S.; Guo, L.; Li, Y.; Yan, B.; Lu, W. Hollow copper sulfide nanoparticle-mediated transdermal drug delivery. Small. 2012. 8(20): p. 3143-3150.

[132] Lai, B.H.; Chen, D.H. Vancomycin-modified LaB6@SiO2/Fe3O4 composite nanoparticles for near-infrared photothermal ablation of bacteria. Acta Biomaterialia. 2013. 9(7): p. 7573-7579.

[133] Chen, M.-C.; Wang, K.-W.; Chen, D.-H.; Ling, M.-H.; Liu, C.-Y. Remotely triggered release of small molecules from LaB6@SiO2-loaded polycaprolactone microneedles. Acta Biomaterialia. 2015. 13: p. 344-353.

[134] Zhao, Y.; Cai, Q.; Qi, W.; Jia, Y.; Xiong, T.; Fan, Z.; Liu, S.; Yang, J.; Li, N.; Chang, B. BSA-CuS Nanoparticles for Photothermal Therapy of Diabetic Wound Infection In Vivo. ChemistrySelect. 2018. 3(32): p. 9510-9516.

CHAPTER 2 FLEXIBLE PLASMONIC PHOTOTHERMAL PATCH FOR BACTERIAL SKIN INFECTION TREATMENT

2.1 Introduction

Skin is a complex multilayer organ that provides the largest interface between the human body and the external environment. In the case of skin damage, infected wounds are easily formed, in particular when the wound is not properly treated or when the human healing mechanism fails [1, 2], which could lead to a serious fever, sepsis or even death. Current treatment approaches for subcutaneous bacterial abscesses involve incision-induced wound drainage and administration of high doses of antibiotics intravenously. Since the wound is usually covered with exudate, topical application of antibiotics usually fails. Besides, it has been shown that activated neutrophils can form a completely unpermeable barrier around the wound [3], making superficial wound a hard place to be reached by treatment agents. While the pain associated with incision-based drainage remains a serious complication for the patient, antibiotic administration continues to be challenging due to the lack of vascularity, limiting the access of the drug to the infection site. Moreover, most of skin infections are attributed to biofilm formation that is intrinsically resistance to antimicrobial therapy regardless of the acquired resistance status of the offending bacteria [4, 5].

The importance of temperature in the wound−healing process [6, 7] as antibiotic alternative for the effective killing of pathogens [8-11] has been recognized as a novel way to treat wound infections. Elevated temperatures can not only directly compromise bacterial cells but also increase local dermal blood flow, leading to an enhanced immunological reaction [7]. Lately, the great development of nanotechnology has boosted the emergence of photothermal therapy, which can be used for fast and efficient ablation of bacteria. For example, we have shown lately that near-infrared absorbing gold nanorods coated with reduced graphene oxide and modified with a mannose comprising ligands allows for the selective and efficient ablation of *Escherichia coli* UTI89 in only a few minutes [9]. In the case of skin bacterial infections, Zhang *et al*. showed the magnetic particles incorporated molybdenum sulfide (MoS_2) for magnet guided photothermal treatment of focal infections [12]. Other targeted photothermal treatments regarding to skin bacterial infection include pH-sensitive nanoparticles that can accumulate at the infectious site [13-15], as well as antibiotic decorated

nanoparticles that can selectively bond to bacterial cells [16]. Despite the good properties of these nanostructures, most of the related studies are carried out in solution with dispersible nanomaterials, which could introduce long term cytotoxicity. In addition, the challenge for large-scale fabrication and the single-use property might hinder the actual use.

In this chapter, a plasmonic-based patch operating in the near-infrared region is demonstrated. While free-standing polymer films can adhere strongly to tissue and are useful as medical plasters [17, 18], compared to dispersed gold nanostructures [19], gold nanoparticle arrays attached to flexible substrates are essentially two-dimensional heating sources that can be operated uninterruptedly [20-23]. The presented antibacterial patch is accommodating a polyimide stripe modified by gold nanoholes (Au NHs) [24-26] film with strong absorption in the near-infrared (NIR) and postcoated with reduced graphene oxide (rGO) (**Figure 2.1**) to increase the light absorption efficiency. Kapton, highly aromatic polyimide resins, praised for its high thermal stability (>300 °C), high tensile strength, and bendability, was chosen due to the attractiveness of this material for a wide range of applications, including soft electronics [27], materials for membranes [28], and packaging. The advantage of this presented topical heating dressing compared to classical methods for the thermal treatment of wounds is that heat can be applied extremely locally, limiting side effects on intact skin. Furthermore, while the use of NIR lamps will result in temperature increase of some degrees, the proposed patch can in a short time raise solution temperatures by several tens of degrees, where the final temperature can be simply tuned by choosing the right laser power and time. Though not discussed in this work, the use of the reduced graphene oxide coatings allows loading of hydrophilic and hydrophobic drugs into the heating patch, which would allow, in addition, the local delivery of therapeutics.

The patch seems adapted for the treatment of infected skin at an early stage, as will be shown with *in vivo* treatment of subcutaneous skin infections initiated in mice. *In vivo* tests on mice with subcutaneous skin infections were successfully healed upon irradiation of the skin patch for 10 min with a light emitting diode (LED) array. The presence of these patches, deposited on artificially infected skin and light activated, prevents skin damage that extended infection could generate.

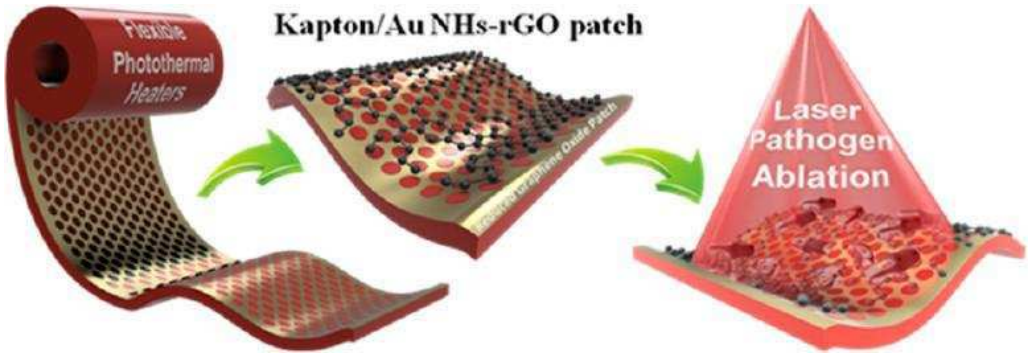

Figure 2.1: Flexible nanoholey photothermal heaters for the ablation of pathogens. Schematic view of the skin patch concept.

2.2 Formation of Nanoholey Photothermal Patches

In this study, the nanoholey photothermal patch is fabricated through a colloidal lithography process. Compared to electron beam or focused ion beam lithography that are used for the precise fabrication of well-ordered nanometric holes on various substrates, colloidal lithography is more facile, less expensive and less time-consuming alternative that can be used for large-scale fabrication of nanopatterned interfaces [29-31]. Though the process is always turned out to be less perfect due to the local defect caused by self-assembly process, it is not limiting given the final application targeted in this study, aiming at developing a flexible interface with plasmonic features absorbing in the near-infrared range. The hole diameter and the center-to-center spacing of the Au NHs array were elaborately adjusted though controlling the size of the spherical masks to produce a strong absorption band close to 980 nm, as the plasmonic heating in the near-infrared region with a 980 nm continuous wave laser is well-adapted for *in vivo* test. In such setup, more than 95% of the photons from a light source can be absorbed by gold nanostructures and converted into heat via electron−phonon interactions that is subsequently transferred to the surrounding medium via phonon−phonon relaxation in a picosecond timescale [32, 33]. The formation of gold nanoholes on Kapton as substrate is depicted in **Figure 2.2**. The polystyrene colloidal spheres with a diameter of 980 nm were first self assembled onto kapton. Then the obtained colloidal structures were subjected to plasma etching to reduce the diameter of the spheres and then coated with 2 nm titanium to ensure good adhesion [34], followed by the coating of 40 nm gold. The residue polystyrene spheres were removed through tape striping and chloroform dissolution to finally create a nanoholey pattern. **Figure 2.2B** shows a representative SEM image of the K/Au NHs

interface. For an etching time of the polystyrene particles of 11 min, highly homogeneous nanoholes with an average diameter of 630 ± 10 nm and a center-to-center spacing of 980 nm are formed in the thin gold film. The long-range ordered gold nanohole array supports both propagating and localized surface plasmon resonance (LSPR) modes, with the hole diameter and periodicity of the Au NHs being important parameters in tuning the absorption band of the interface [35-38]. The UV-Vis absorption spectra of Kapton only and K/Au NHs between 500 and 1100 nm are depicted in **Figure 2.2C**. Kapton alone absorbs strongly below 600 nm due to its polyimide nature. In the case of K/Au NHs, several absorption bands located at 650, 713, and 950 nm are observed. While the band at 713 nm might be associated with the SPR of the water−Au NHs interface, the maximum absorption at 950 nm occurs through the excitation of SP waves in the nanohole arrays, acting as two-dimensional diffraction gratings that convert incident photons into SP waves [39].

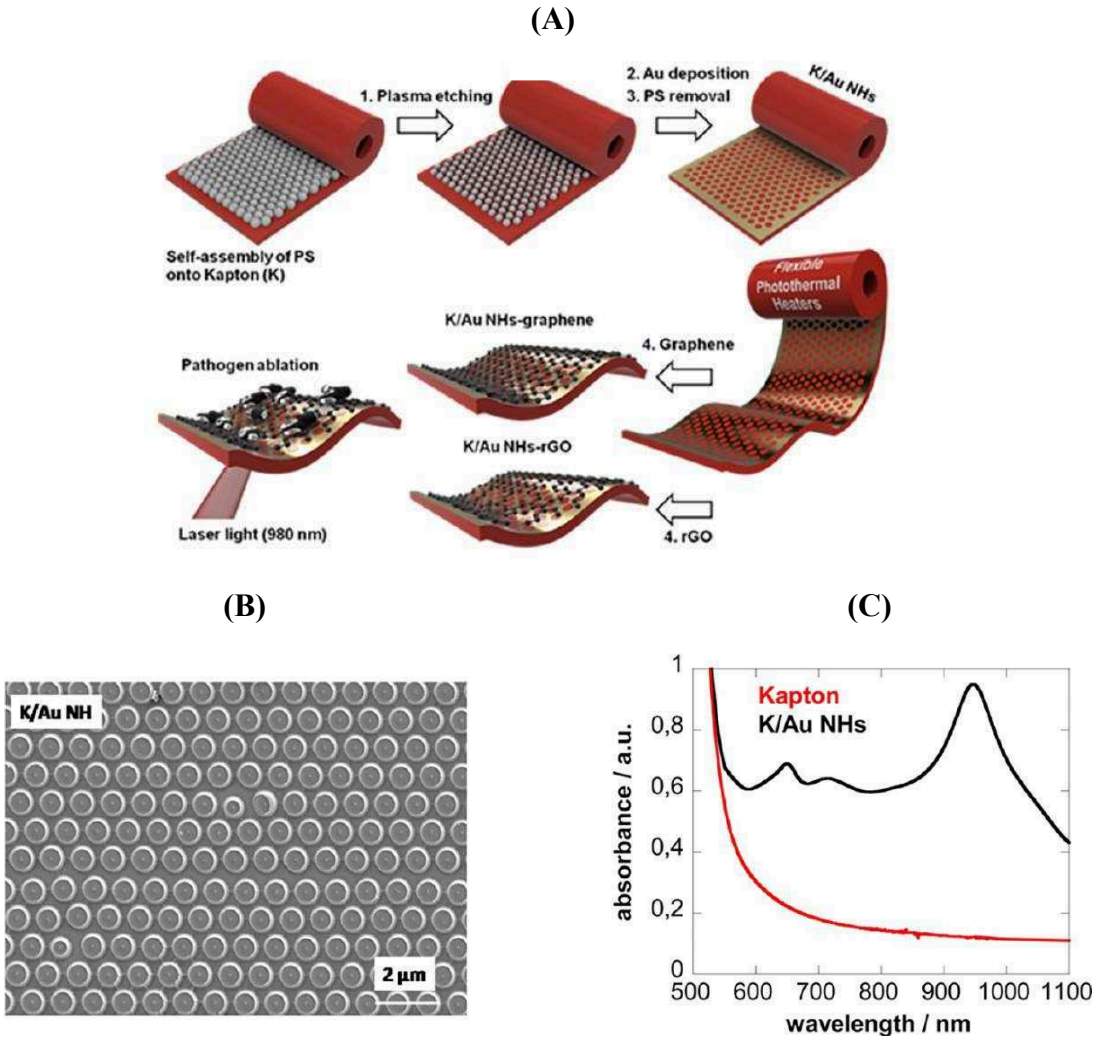

Figure 2.2: Flexible nanoholey photothermal patch. (A) K/Au NHs interface formation, postcoated with graphene or rGO for photothermal ablation of pathogens; (B) SEM image of

K/Au NHs formed by using colloidal lithography; (C) Typical absorption spectra for Kapton and K/Au NHs samples.

The photothermal heating properties of the patterned patch triggered by a 980 nm continuous laser is shown in **Figure 2.3A**. Compared to Kapton alone, which shows a negligible photothermal effect, irradiation of K/Au NHs under the same conditions results in an elevated average temperature of about 60 °C. However, for an efficient inactivation of bacteria, temperatures of more than 70 °C are recommended as this allows inactivation of the bacteria population through cell wall damage and protein denaturation [9]. Using laser power density of 5 W cm^{-2} results in final solution temperatures of 76 ± 2 °C (**Figure 2.3B**). However, we have shown lately that elevated laser powers result in skin inflammation and skin burning in the worst case [4, 40]. With laser power densities >5 W cm^{-2}, modification of the skin epidermis structure was noticed, with a total disruption of the stratum corneum collagen cell structure changing to keratin-like (scar tissue) [41]. We thus investigated if postcoating of K/Au NHs with graphene (G) or reduced graphene oxide (rGO) would allow reaching higher temperatures using lower power densities.

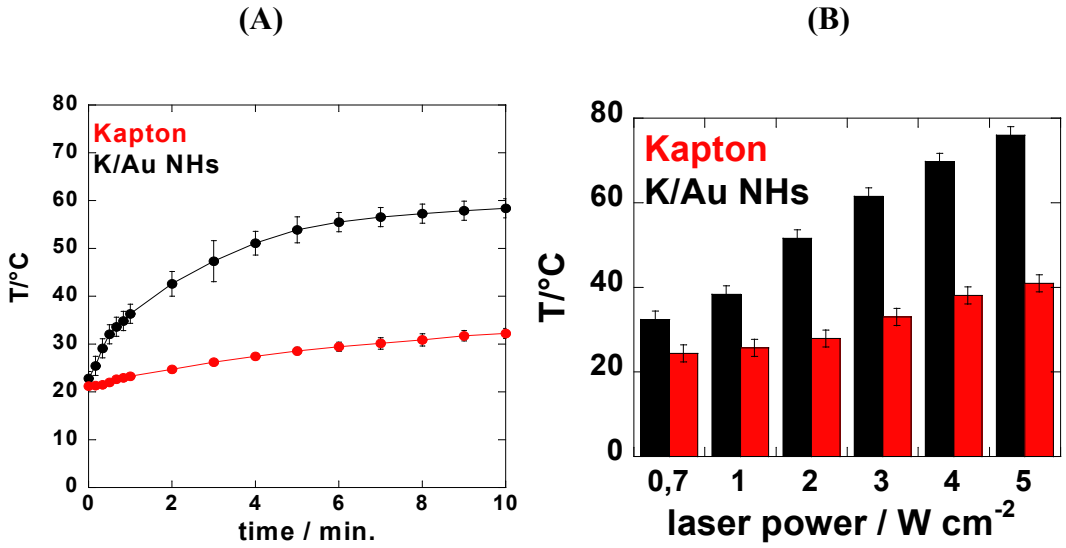

Figure 2.3: (A) Photothermal heating curves of Katon (red) and K/Au NHs (black) when immersed in water and exposed to laser light of 980 nm for 10 min at 2 W cm^{-2}; (B) Temperature profile of Kapton and K/Au NH interfaces at different laser power densities recorded after 10 min irradiation

The K/Au NHs-graphene (K/Au NHs-G) device was formed by mechanical transfer of chemical vapour deposition (CVD)-grown graphene on Cu onto the interface [9, 42]. As we can see from the SEM and Raman images of K/Au NHs-G in **Figure 2.4**, the nanohole arrays

are fully covered by monolayer graphene with several local multilayer defects, which is caused in the process of graphene transfer. However, K/Au NHs-G shows no improved photothermal properties over K/Au NHs (**Figure 2.4C**). This indicates that for K/Au NHs-G the photothermal heating capacitance is entirely governed by the Au NHs and the submicrometer thick graphene has a marginal additional effect.

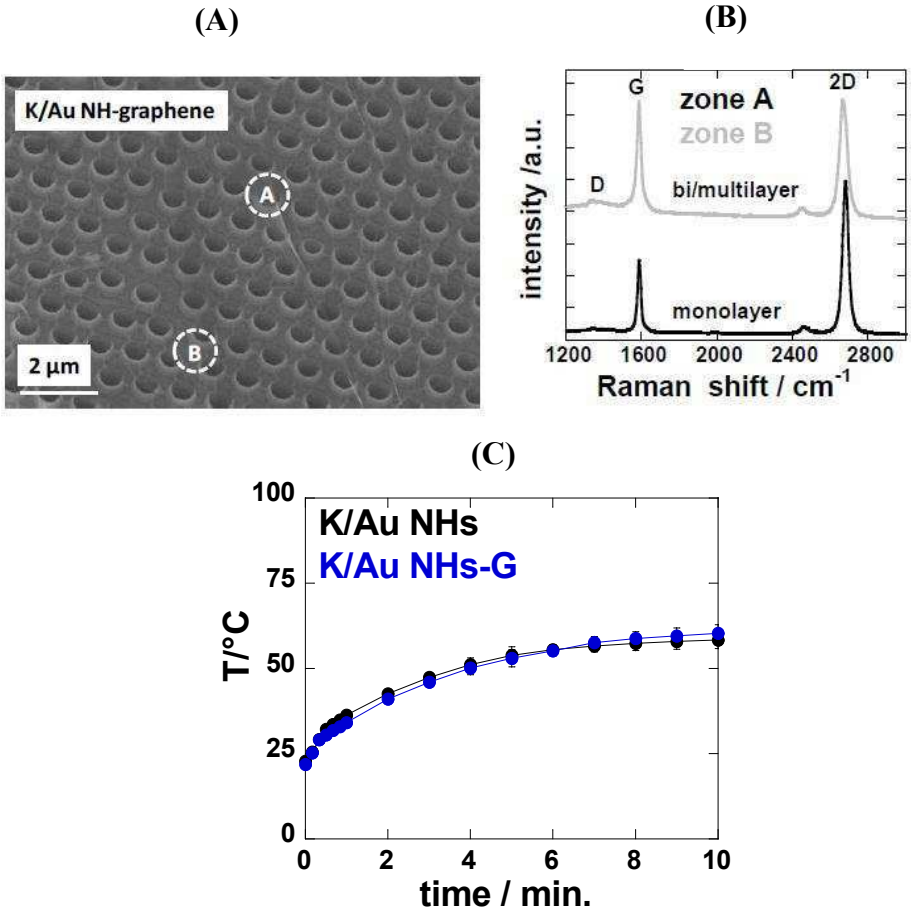

Figure 2.4: (A) SEM of graphene coated K/Au NHs; (B) Raman images on two different areas of K/Au NHs-graphene; (C) Photothermal heating curves of K/Au NHs (black) and K/Au NHs-graphene (blue) when immersed in water and exposed to laser light of 980 nm for 10 min at 2 W cm^{-2}.

Postcoating of K/Au NHs with rGO was achieved by 3 times drop-casting of a rGO solution (1 mg mL^{-1}), resulting in a K/Au NHs-rGO interface entirely covered with rGO nanoflakes of about 10−1000 nm in thickness (**Figure 2.5A**). These stacked rGO nanoflake coatings show considerable improvement of the photothermal properties, with temperatures reaching 80 ± 2 °C after 10 min irradiation at 2 W cm^{-2} (**Figure 2.5B**). As is depicted in **Figure 2.5C** and **Figure 2.5D**, the coated interfaces can be bended while the bending does not change the heating property, enabling the interface a good candidate for skin infection application. The interfaces proved to be highly stable over time even when in contact with skin of mice (see

Section 2.4) and no degradation of the photothermal properties were observed upon leaving the interfaces for 3 months either in air or immersed in water, making the interfaces for high interest for practical applications as seen in the following.

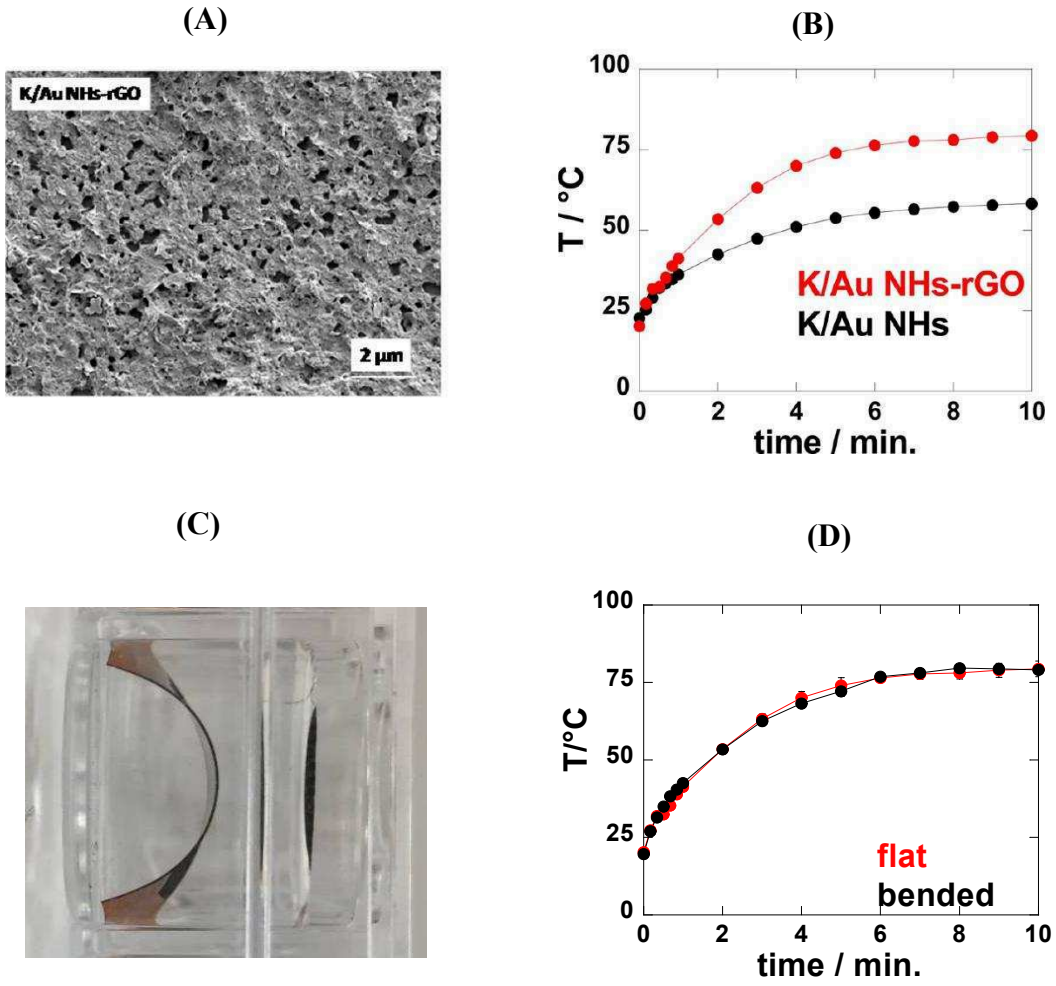

Figure 2.5: Flexible reduced graphene oxide (rGO)-based heating patches. (A) SEM of rGO coated K/Au NHs-rGO interface; (B) Photothermal heating curves of K/Au NHs (black) and K/Au NHs-rGO (red) immersed in water and exposed to laser light of 980 nm for 10 min at 2 W cm^{-2}; (C) Photograph of a bended K/Au NHs-rGO interface when immersed in water (D) Temperature profile of bended and flat patch.

2.3 Photothermal Ablation of Pathogens Present in Aqueous Solutions

The development of efficient treatments for biofilm-forming Gram-negative pathogens such as the clinical enteroaggregative Crohn's disease-associated adherent invasive *E. coli* LF82

strain, causing severe infections, has proven to be particularly difficult. *Enterococcus faecalis*, a Gram-positive pathogen from the Streptococcus system, was in addition investigated as it can establish life-threatening infections in humans, especially in hospital environments, where the naturally high levels of antibiotic resistance found in *E. faecalis* contribute to its resilience to resolution of the infection. Finally, Gram-positive *S. epidermidis* is included into our investigation. Staphylococci are the most abundant skin-colonizing bacteria and the most significant causes of nosocomial infections and community-associated skin infections [43]. **Figure 2.6A** shows the photothermal ablation capacity of the different patches for Gram positive and Gram negative planktonic bacteria. An interface-dependent photothermal pathogen ablation effect was observed. Kapton alone does not show any photothermal ablation of pathogens. The K/Au NHs patch exhibits about 2 log10 (*E. coli* LF82 and *E. faecalis*) and 3 log10 (*S. epidermidis*) reduction in cell viability of planktonic bacteria after 10 min light activation. In the case of using the K/Au NHs-G architecture, further reduction by 1 log10 is noticed for the Gram-positive strains. Using the K/Au NHs-rGO device and laser irradiation for 10 min, a complete photothermal ablation of all three pathogens was observed, being as effective as the antibiotic-loaded gold nanocages reported recently for *Staphylococcus aureus* [44]. Similar results were reported by Zhu *et al*. using gold nanorod (Au NR) arrays with optimized density on glass [45]. In this case an array of well-packed Au NRs was formed using the confined convective arraying technique, where the density of the deposited particles is controlled by the concentration of the gold nanorods solution, the velocity of the moving substrate, and the temperature. Only a high concentration of Au NRs, which have to be pre-synthesized, achieved bacterial mortality rates up to 98%. Our approach, using colloidal lithography to form Au NHs, has the advantage of being highly reproducible and adapted for high-throughput application such as the manufacturing of medical patches to treat skin infections, as discussed here. Live/Dead assays performed on *E. coli* before and after photothermal treatment with different patches are shown in **Figure 2.6B**. The cell viability was significantly affected by K/Au NHs-rGO as seen from the high number of red stained cells, compared with partial cell death in the case of K/Au NHs-G and K/Au NHs, Kapton alone does not show any effect on bacterial cell viability. These results demonstrate that the thermal diffusion, taking place upon irradiation, contributes to heat-induced damage of the bacteria present in the surrounding environment. The SEM images of *E. coli* LF82 before and after photothermal treatment with are K/Au NHs-rGO patches are demonstrated in **Figure 2.6C**. The untreated bacteria display an intact cell membrane, indicating a good cell

viability. While photothermal treatment with K/Au NHs-rGO patches results in the formation of pores in the bacteria cell membrane and subsequent cell death.

(A)

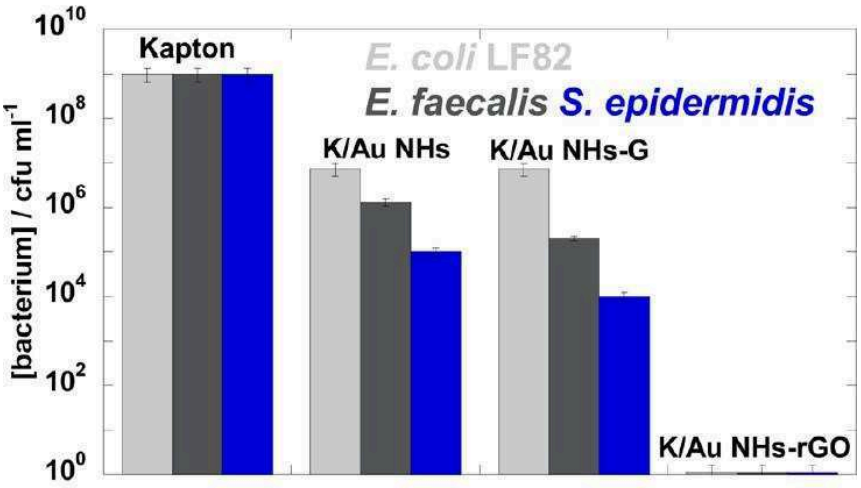

(B)

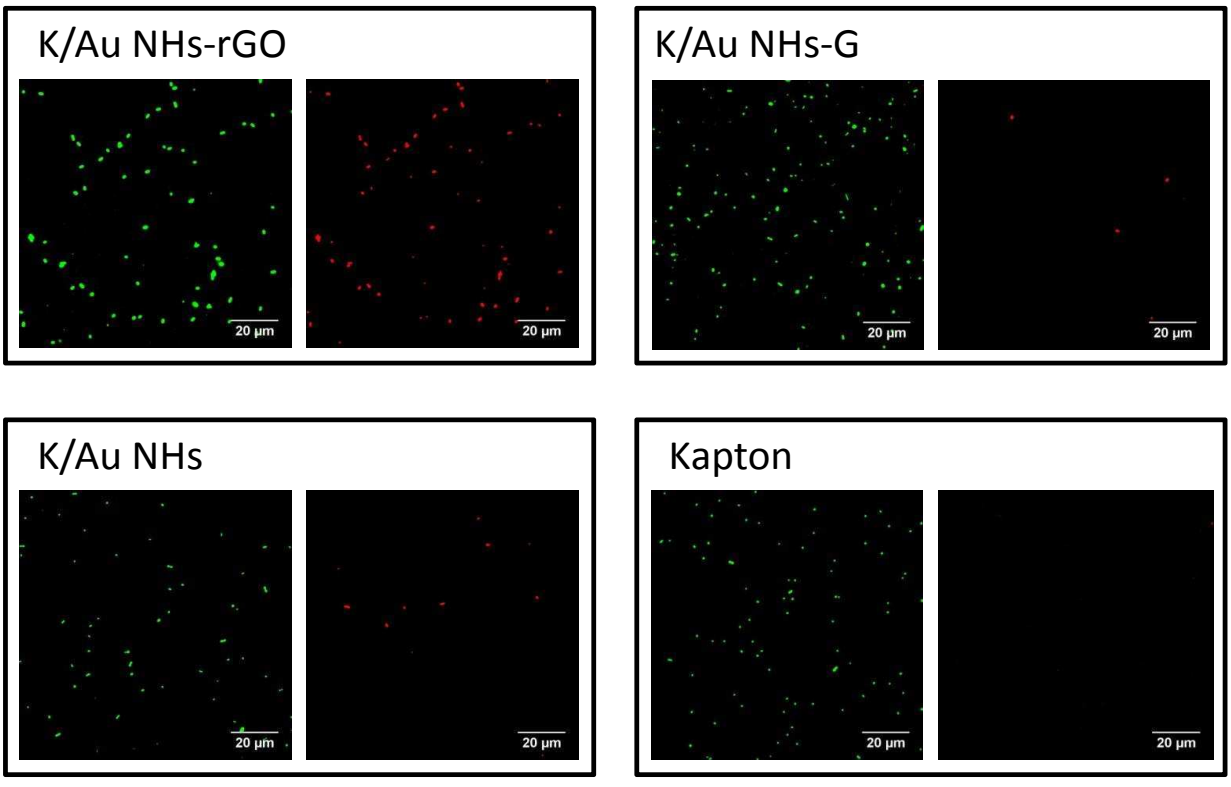

(C)

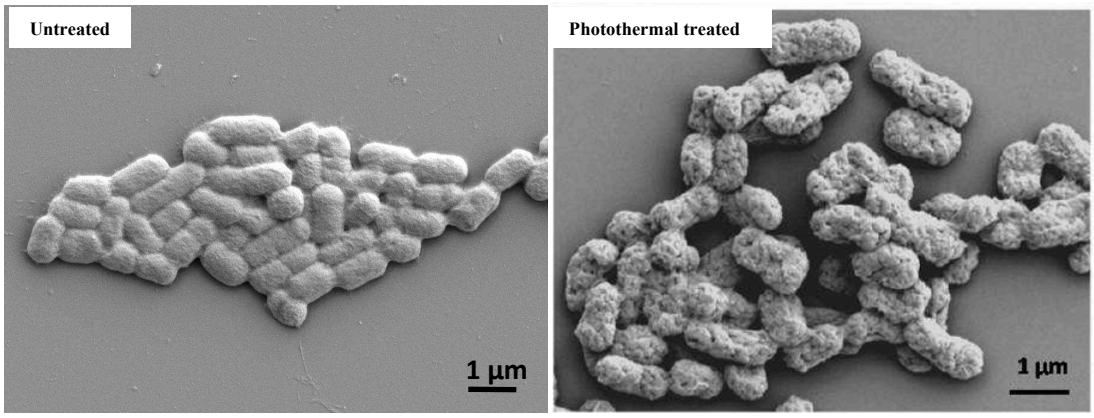

Figure 2.6: Photothermal bacteria ablation in solution. (A) Bacterial cell viability (in cfu mL^{-1}) of *E. coli* LF82, *E. faecalis*, and *S. epidermidis* upon irradiation of different interfaces at 980 nm (2 W cm^{-2}); (B) Live/dead assays total (green) and dead (red) bacteria cell count images of *E. coli* after photothermal treatment with different patches; (C) SEM image of *E.coli* LF82 before and after photothermal treatment with K/Au NHs-rGO for 10 min (980 nm, 2 W cm^{-2}).

Considering the good photothermal activity of K/Au NHs-rGO, we further performed an experiment to verify the time-dependence of photothermal antibacterial effect. As is shown in **Figure 2.7**, 2 log10 reduction in the case of *E.coli* LF82 and *E. faecalis* are seen after 3 min irradiation, while 3 more log10 reduction are found after 5 min in both cases. All the *E.coli* LF82 and *E. faecalis* are compromised after 7 min. The viability of *S. epidermidis* start to decease after 5 min while 4log10 cells are still alive after 7 min treatment. However, all the bacteria are killed after a 10 min photothermal treatment. The results, which are consistent with the one shown above, further proved the good photothermal antibacterial property of K/Au NHs-rGO as, in fact, 7 min are enough to compromise most of the bacterial cells.

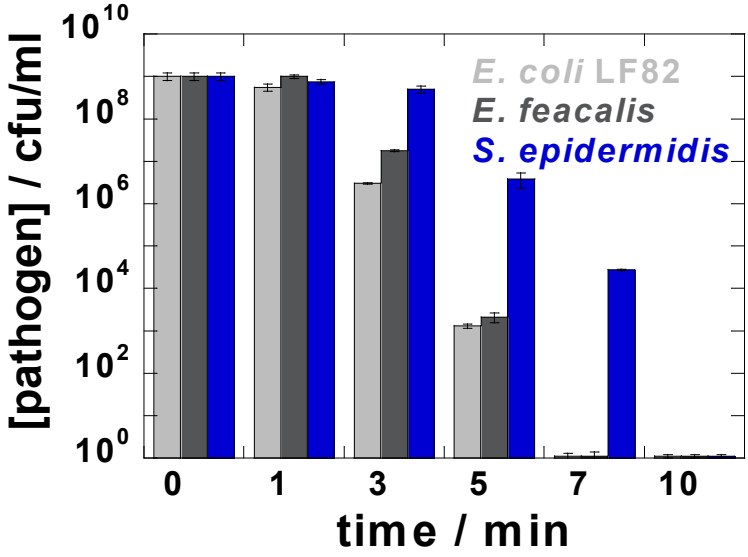

Figure 2.7: Bacterial cell viability of Gram-negative *E. coli* LF82 and Gram-positive *E. faecalis* and *S. epidermidis* upon immersion K/Au NHs-rGO at 980 nm with 2 W cm^{-2} for different time intervals.

2.4 Biofilm formation on different interfaces

A variety of coatings have been reported to prevent or reduce the formation of pathogenic biofilms. However, most of these films fail to work correctly over a long period of time in biological media such as urine, where bacteria grow rapidly. The capabilities of the different nanoholey interfaces to prevent bacteria attachment were investigated. SEM images and fluorescent images were taken after 72 h incubation with bacteria using different interfaces. As is shown in **Figure 2.8**, The SEM images and fluorescent images indicate that bacteria are in general settling neither onto K/Au NHs nor onto Kapton spontaneously, while dense bacteria films are formed on K/Au NHs-G patches and K/Au NHs-rGO patches. This result is in line with the well-accepted concept of the importance of the material surface properties on bacterial adhesion [46-48]. Compared to flat gold, nanostructured gold surfaces have shown to possess excellent antifouling properties [49], which are believed to be the underlying mechanism for the observed bacteria antifouling properties of K/Au NHs. The bacterial cell wall is negatively charged due to the presence of teichoic acids in the case of Gram-positive bacteria, and in the case of Gram-negative bacteria due to an outer covering of phospholipids and lipopolysaccharides, preferential adhesion to positively charged surfaces are expected [50]. Other adhesion parameters seem to be underlying the interaction between the negatively

charged rGO and graphene interfaces with the bacteria. Moreover, the increased roughness owing to the coating of rGO or grephene could attribute bacterial adhesion, permitting the formation of biofilm [51].

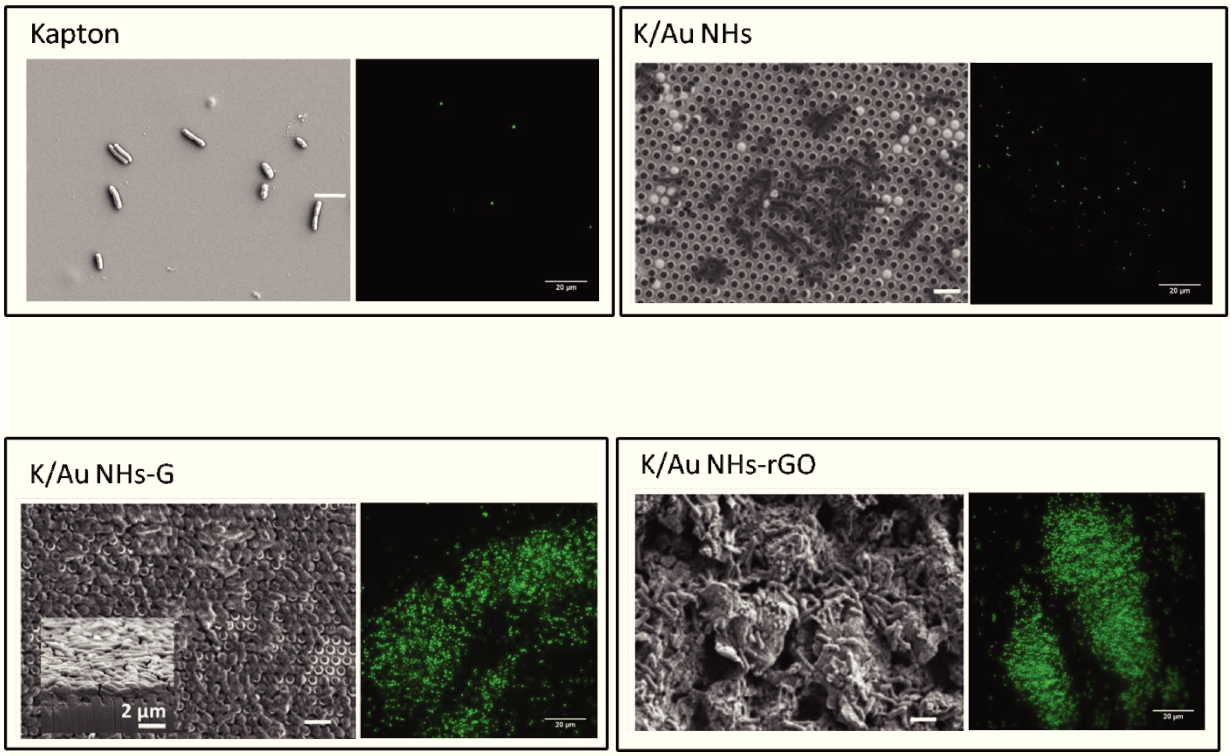

Figure 2.8: SEM images and green fluorescent images of bacterial adhesion to different interfaces studied with *E.Coli* LF82. (bacteria were stained with Cyto 9 and imaged with a fluorescent microscopy equipped with green filters, scale bars represent 2µm and 20µm in SEM images and fluorescent images, respectively.)

2.5 Treatment of Subcutaneous Skin Infections

To test the possibility of photothermal therapy of superficial skin infections *in vivo*, K/Au NHs and K/Au NHs-rGO interfaces were selected according to the results of *in vitro* test. Prior to any in vivo experiment, the level of living tissue heating was determined by applying sterilized K/Au NHs-rGO to the surface of raw pork meat and determining the surface temperature with a FLIR camera by irradiating the tissue with a 940 nm (2 W cm^{-2}) LED microarray. Sterilization of the patch was performed upon immersion of the patches into Anison for 1 h. The used LED microarray allows for a uniform irradiation of a 2 × 2 cm^2 surface area. As can be seen from **Figure 2.9**, the K/Au NHs-rGO interface result in different heating temperatures, the heating to 60 °C for 10 min caused visible denaturation of muscle tissue (“burns”) while heating to 47 °C did not affect the tissue. Indeed, previous study has shown that the denaturation of proteins such as collagen start from 55 °C [52], overheating

could compromise bacterial cells but could also lead to great side effects. Therefore, the LED power was adjusted to maintain surface heating at around 50 °C, where no visible damage was observed after 10 min irradiation.

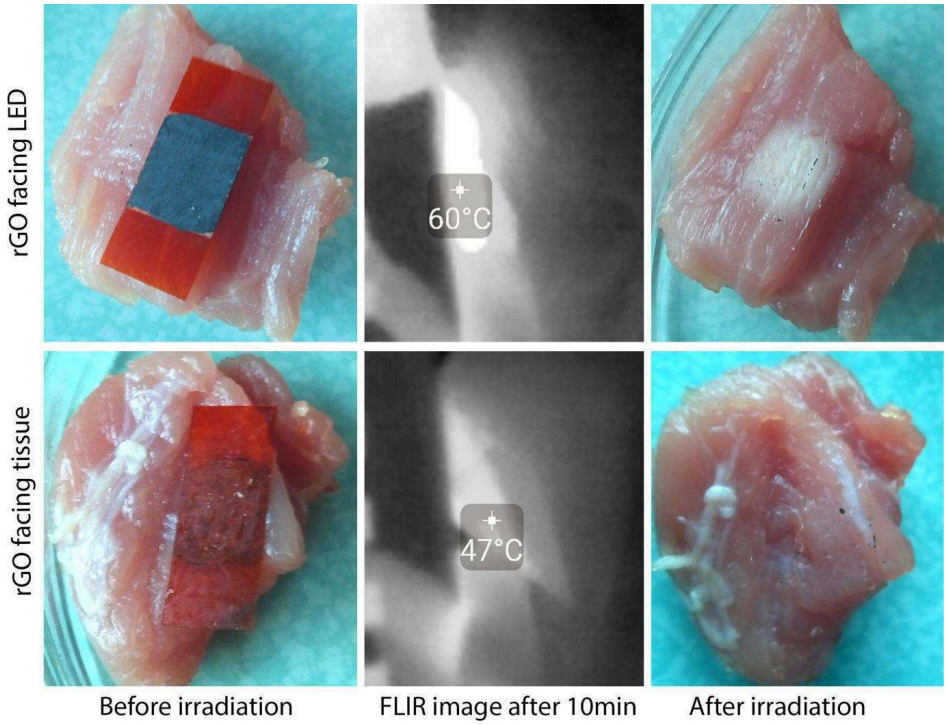

Figure 2.9: Different placements (graphene facing tissue and facing LED source) were tested, as well as LED power and heating distance to achieve optimal results. Upper row demonstrates the condition when graphene is facing the light source with heating up to 60 °C and causing meat burns, while lower row is using opposite orientation of K/Au NHs-rGO patch, with heating to 47 °C and no visible tissue damage.

In vivo test was carried out on white laboratory Balb/c mice infected with *S. epidermidis,* followed by applying different photothermal patches on the infected area and irradiating with the LED microarray. As is demonstrated in **Figure 2.10**, Mouse hairs on the back were firstly removed in order to facilitating the application of photothermal patch. Then an infected wound was developed through topical application of a bacterial suspension. This early state infection was treated by applying the photothermal patches on the infectious site, followed by an irradiation for 10 min at a power density of 2 W cm^{-2}. K/Au NHs was much less heated than K/Au NHs-rGO at the same power density, with 36 ˚C and 51 ˚C, respectively. The freshly infected mouse displays no obvious symptom, while after 5 days of infection initiation, superficial bacterial infiltrate was observed in the infected group, indicating a great damage of epidermal and dermal layers of skin. However, when treated with K/Au NHs-rGO photothermal patch, no obvious infiltrate was detected.

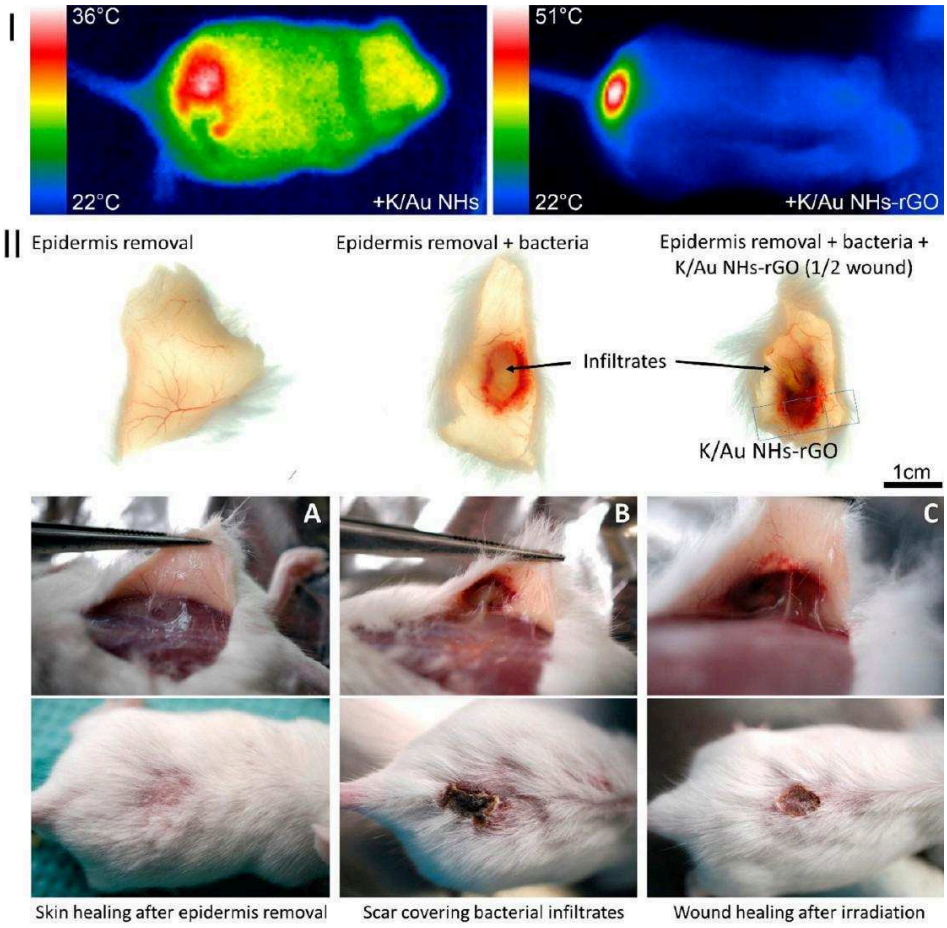

Figure 2.10: *In vivo* photothermal therapy of skin infections initiated in mice with K/Au NHs-rGO patches. (I) Thermal images of mice heated witheither K/Au NHs (max. temperature ~36 °C, left) or K/Au NHs-rGO (max. temperature ~51 °C, right) demostrate uniform heat distribution in theirradiated area. (II) Photographs of mouse skin before (A) and after 5 days of infection (B and C) without and with laser illumination.

To quantitatively estimate the therapeutic effect of the photothermal patches on skin bacterial infection, 11 white laboratory Balb/c mice were infected and monitored for 5 days. Then the mice were divided into three groups and subjected to different kinds of treatment. Thereafter, the skin erythema area was imaged with a camera before and 72 h after the treatment and the ratio between the two areas were calculated to estimate the skin recovery. As is displayed in **Figure 2.11**, photothermal treatment with K/Au NHs patch shows a very limited effect on the skin infection when compared to the untreated group, with the ratio reached 112% and 142.7%, respectively. However, in contrast, the treatment using K/Au NHs-rGO significantly decreased the skin erythema area with a ratio of 51.53%, indicating a superior recovery effect over the other two groups.

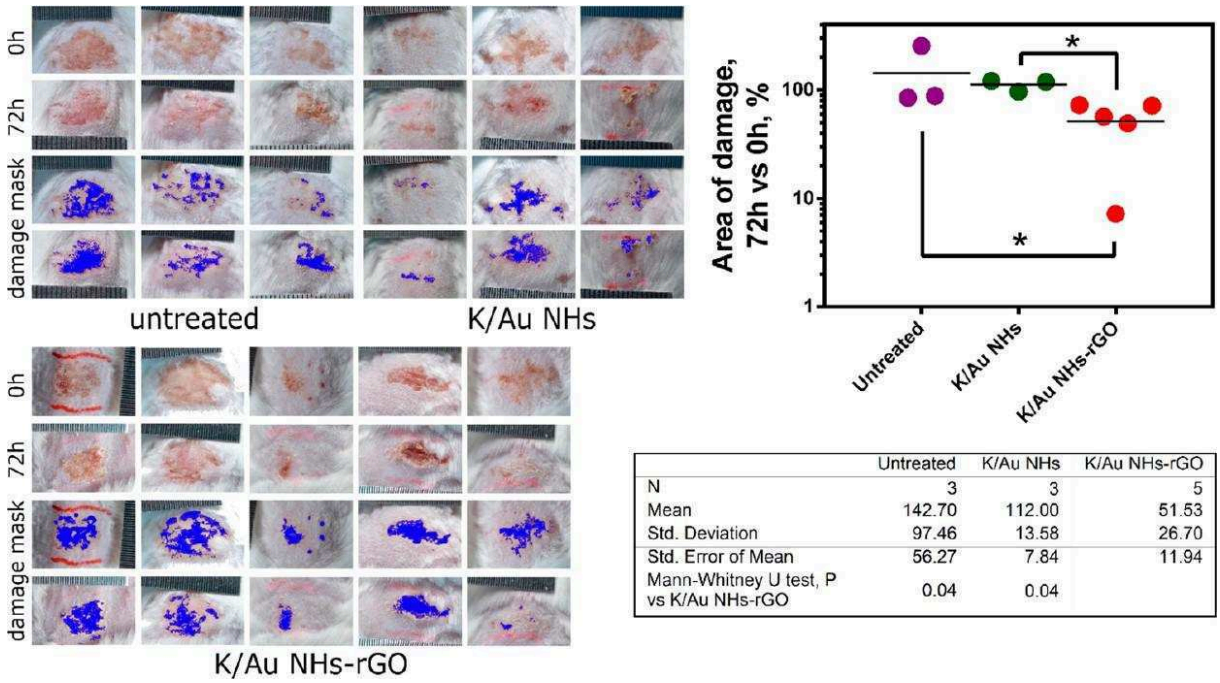

	Untreated	K/Au NHs	K/Au NHs-rGO
N	3	3	5
Mean	142.70	112.00	51.53
Std. Deviation	97.46	13.58	26.70
Std. Error of Mean	56.27	7.84	11.94
Mann-Whitney U test, P vs K/Au NHs-rGO	0.04	0.04	

Figure 2.11: Quantification of mouse skin erythema. Skin analysis before and 72 h after treatment with K/Au NHs and K/Au NHs-rGO patch: (left) Photographs of mouse skin indicating infected areas; (right) determination of average skin damage after 72 h under different treatment conditionstogether with statistical analysis.

To further study the therapeutic effect, the mice treated with K/Au NHs-rGO were sacrificed and the skin was sectioned for histological analysis. The results shown in **Figure 2.12** revealed that bacterial infection caused prominent skin damage beneath the scar covering the wound. This is accompanied by complete destruction of the epidermal, dermis layer and underlying muscles. In addition, bacterial and leukocytic infiltration is abundant (**Figure 2.12E**). At the same time the infected wound illuminated through the K/Au NHs-rGO patch for 10 min showed only traces of bacterial infiltration, with granulation tissue abundantly formed beneath the muscular layer, suggesting active wound healing. Indeed, at the interface between the treated and the nontreated wound, prominent granulation tissues are seen where the patch was present (**Figure 2.12F**), while the penetrating bacterial infection, accompanied by tissue necrosis, is clearly visible for areas without illumination.

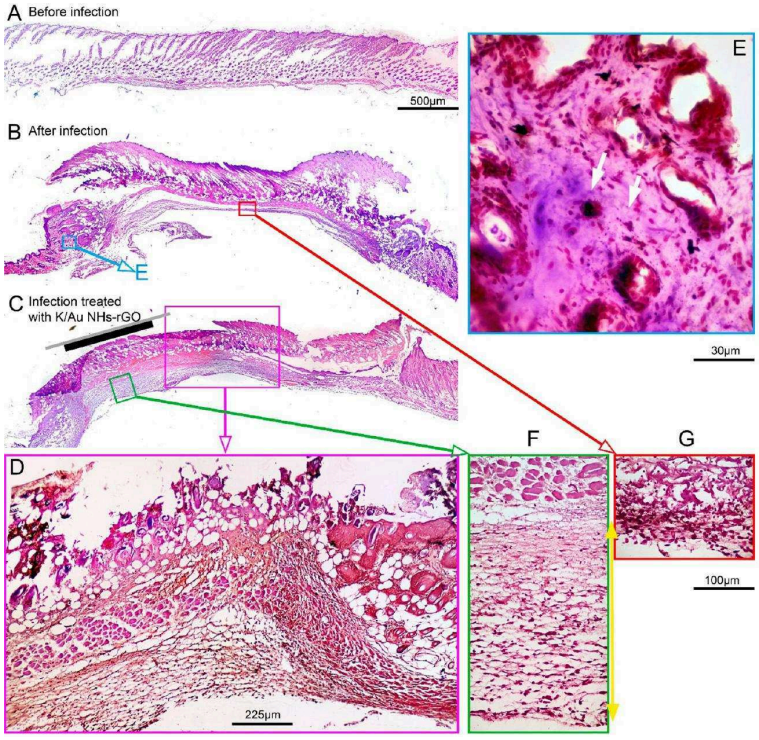

Figure 2.12: Histological analysis of mouse skin with longitudinal section across the wound and scar tissue. (A) Skin before infection. (B) Skin after infection. (C) Skin after infection with photothermally treated part of wound. (D) Interface between irradiated and nonirradiated tissue clearly showing abundant formation of granulation tissue beneath the heated area; (E) leukocyte and bacterial infiltration at the edge of the wound, where the tissue still was not converted to pus; (F and G) heated and unheated areas of infection demonstrating granulation tissue (marked with yellow arrow) attributable to wound healing, located beneath the layer of muscle (aligned at the top, to the same scale). Heated area shows viable muscular fiber and abundant granulation tissue, while the nonheated area possesses necrotic muscular fibers and puslike infiltrate beneath it. (A−C) H&E staining. (D−G) Gram staining. D−G are corresponding enlarged areas of parallel slides indicated by color.

2.6 Conclusion

In conclusion, a novel nanotechnology approach for the local healing of infected skin wounds at early stages is presented in this chapter. The strategy consists of using a flexible skin patch of variable size based on Kapton modified with gold nanoholes that exhibit plasmon-driven heat capacity in the NIR. While in this work skin patches of 1 × 1 cm^2 in size were used, the technology is easily adaptable to larger, relevant sizes for the treatment of wounded skin. Post coating of these patches with rGO enhances the observed photothermal behavior. Moreover, these fabricated interfaces are highly stable over time, ensuring safe use as functional skin patches. The bactericidal activity of the patch can be modulated and turned on and off using light. The highly efficient photothermal conversion of the patch resulted in total eradication of

Gram positive and Gram negative pathogens in solution. The device was further used for the local treatment of mice with infected skin wounds. Without the addition of any antibiotic, wound healing was observed upon placing the K/Au NHs-rGO patch over the wound and irradiating for 10 min. The thickness of the rGO layer (10−1000 nm) deposited onto the Au NHs array did not influence in any significant manner the healing process. As thinner rGO films proved to be mechanically more stable, thin rGO coatings are advantageous for this application. Indeed, rGO layers of about <100 nm in thickness were used more than 10 times without any loss in bactericidal activity upon light illumination. This approach opens new avenues to wound management and the treatment of patients with subcutaneous infections. The reusability of the patch, together with the possibility to sterilize it, recommend this method as cost-effective and, thus, potentially marketable. Furthermore, convenient patch usage rather than injection of nanostructures for photothermal pathogen treatment makes this approach a safe and highly attractive alternative as the toxicity of the nanostructures is of no concern here. This modus operando might allow personalized treatment of skin infections in a nonclinical setting.

2.7 References

[1] Martin, P. Wound healing--aiming for perfect skin regeneration. science. 1997. 276(5309): p. 75-81.

[2] Szunerits, S.; Boukherroub, R. Antibacterial activity of graphene-based materials. Journal of Materials Chemistry B. 2016. 4(43): p. 6892-6912.

[3] Bilyy, R.; Fedorov, V.; Vovk, V.; Leppkes, M.; Dumych, T.; Chopyak, V.; Schett, G.; Herrmann, M. Neutrophil Extracellular Traps Form a Barrier between Necrotic and Viable Areas in Acute Abdominal Inflammation. Frontier Immunology. 2016. 7: 424.

[4] Römling, U.; Balsalobre, C. Biofilm infections, their resilience to therapy and innovative treatment strategies. Journal of internal medicine. 2012. 272: p. 541-561.

[5] Brandwein, M.; Steinberg, D.; Meshner, S. Microbial biofilms and the human skin microbiome. NPJ Biofilms Microbiomes. 2016. 2: 3.

[6] Anisia, E.I.; Ciuntu, R.; Cantemir, A.; Anton, N.; Danielescu, C.; Negru, R.; Bogdanici, C.M.; Vasiluta, C.; Georgescu, S.; Sirbu, P.D.; Ciuntu, B.M. The Importance of Fluconazole in Treatment of Endogenous Endophthalmitis in Patients Prior Treated Using Negative Pressure Therapy for Wound Closure Contaminated with Methicillin-resistant Staphylococcus aureus. Revista De Chimie. 2017. 68(7): p. 1598-1601.

[7] Khan, A.A.; Banwell, P.E.; Bakker, M.C.; Gillespie, P.G.; McGrouther, D.A.; Roberts, A.H.; Topical radiant heating in wound healing: an experimental study in a donor site wound model. International Wound Journal. 2004. 1(4): p. 233-240.

[8] Wu. M.C.; Deokar. A.R.; Liao. J.H.; Shih. P.Y.; Ling. Y.C. Graphene-Based Photothermal Agent for rapid and effective killing of bacteria. ACS nano. 2013. 7(2): p. 1281-1290.

[9] Turcheniuk, K.; Hage, C.-H.; Spadavecchia, J.; Serrano, A.Y.; Larroulet, I.; Pesquera, A.; Zurutuza, A.; Pisfil, M.G.; Héliot, L.; Boukaert, J.; Boukherroub, R.; Szunerits, S. Plasmonic photothermal destruction of uropathogenic E. coli with reduced graphene oxide and core/shell nanocomposites of gold nanorods/reduced graphene oxide. Journal of Materials Chemistry B. 2015. 3(3): p. 375-386.

[10] Lee, E.S.; Caldwell, M.P.; Talarico, P.J.; Kuskowski, M.A.; Santilli, S.M.; Use of a noncontact radiant heat bandage and Staphylococcus aureus dermal infections inanovine model. Wound Repair and Regeneration. 2000. 8(6): p. 562-566.

[11] Chiang, W.-L.; Lin, T.-T.; Sureshbabu, R.; Chia, W.-T.; Hsiao, H.-C.; Liu, H.-Y.; Yang, C.-M.; Sung, H.-W. A rapid drug release system with a NIR light-activated molecular switch for dual-modality photothermal/antibiotic treatments of subcutaneous abscesses. Journal of Controlled Release. 2015. 199: p. 53-62.

[12] Zhang, W.; Shi, S.; Wang, Y.; Yu, S.; Zhu, W.; Zhang, X.; Zhang, D.; Yang, B.; Wang, X.; Wang, J. Versatile Molybdenum Disulfide Based Antibacterial Composites for in Vitro Enhanced Sterilization and in Vivo Focal Infection Therapy. nanoscale. 2013. 00: p. 1-7.

[13] Hsiao, C.-W.; Chen, H.-L.; Liao Z.-X.; Sureshbabu. R.; Hsiao H.-C.; Lin S.-J.; Chang Y.; Sung, H.-W. Effective Photothermal Killing of Pathogenic Bacteria by Using Spatially Tunable Colloidal Gels with Nano-Localized Heating Sources. Advanced Functional Materials. 2015. 25: p. 721-728.

[14] Korupalli, C.; Huang, C.C.; Lin, W.C.; Pan, W.Y.; Lin, P.Y.; Wan, W.L.; Li, M.J.; Chang, Y.; Sung, H.W. Acidity-triggered charge-convertible nanoparticles that can cause bacterium-specific aggregation in situ to enhance photothermal ablation of focal infection. Biomaterials. 2017. 116: p. 1-9.

[15] Hu, D.; Li, H.; Wang, B.; Ye, Z.; Lei, W.; Jia, F.; Jin, Q.; Ren, K.F.; Ji, J. Surface-Adaptive Gold Nanoparticles with Effective Adherence and Enhanced Photothermal Ablation of Methicillin-Resistant Staphylococcus aureus Biofilm. ACS Nano. 2017. 11(9): p. 9330-9339.

[16] Zhao, Z.; Yan, R.; Yi, X.; Li, J.; Rao, J.; Guo, Z.; Yang, Y.; Li, W.; Li, Y.Q.; Chen, C. Bacteria-Activated Theranostic Nanoprobes against Methicillin-Resistant Staphylococcus aureus Infection. ACS Nano. 2017. 11(5): p. 4428-4438.

[17] Chen, D.; Wu, M.; Chen, J.; Zhang, C.; Pan, T.; Zhang, B.; Tian, H.; Chen, X.; Sun, J. Robust, flexible, and bioadhesive free-standing films for the co-delivery of antibiotics and growth factors. Langmuir. 2014. 30(46): p. 13898-13906.

[18] Chen, D.; Chen, J.; Wu, M.; Tian, H.; Chen, X.; Sun, J. Robust and flexible free-standing films for unidirectional drug delivery. Langmuir. 2013. 29(26): p. 8328-34.

[19] Yin, Y.; Alivisatos, A.P. Colloidal nanocrystal synthesis and the organic – inorganic interface. Nature. 2004. 437: p. 664-670.

[20] Webb, R.C.; Bonifas, A.P.; Behnaz, A.; Zhang, Y.; Yu, K.J.; Cheng, H.; Shi, M.; Bian, Z.; Liu, Z.; Kim, Y.-S.; Yeo, W.-H.; Park, J.S.; Song, J.; Li, Y.; Huang, Y.; Gorbach, A.M.; Rogers, J.A. Ultrathin conformal devices for precise and continuous thermal characterization of human skin. Nature Materials. 2013. 12: p. 938-944.

[21] Baffou, G.; Berto, P.; Ureña, E.B.; Quidant, R.; Monneret, S.; Polleux, J.; Rigneault, H. Photoinduced Heating of Nanoparticle Arrays. ACS nano. 2013. 7(8): p. 6478-6488.

[22] Tordera, D.; Zhao, D.; Volkov, A.V.; Crispin, X.; Jonsson, M.P. Thermoplasmonic Semitransparent Nanohole Electrodes. Nano Letters. 2017. 17(5): p. 3145-3151.

[23] Virk, M.; Xiong, K.; Svedendahl, M.; Kall, M.; Dahlin, A.B. A thermal plasmonic sensor platform: resistive heating of nanohole arrays. Nano Letters. 2014. 14(6): p. 3544-3549.

[24] Brolo, A.G.; Kwok, S.C.; Moffitt, M.G.; Gordon, R.; Riordon, J.; Kavanagh, K.L. Enhanced Fluorescence from Arrays of Nanoholes in a Gold Film. Journal of America Chemistry Society. 2005. 127: p. 14936-14941.

[25] Rindzevicius, T.; Alaverdyan, Y.; Sepulveda, B.; Pakizeh, T.; Käll, M.; Hillenbrand, R.; Aizpurua, J.; Abajo, F.J.G.d. Nanoholes Plasmons in Optically Thin Gold Films. Journal of Physical Chemistry C. 2007. 111(3): p. 1207-1211.

[26] Yang, J.-C.; Ji, J.; Hogle, J.M.; Larson, D.N. Metallic Nanohole Arrays on Fluoropolymer Substrates as Small Label-Free Real-Time Bioprobes. Nano Letters. 2008. 8(9): p. 2718-2724.

[27] Wang, X.; Jiang, K.; Shen, G. Flexible fiber energy storage and integrated devices: recent progress and perspectives. Materials Today. 2015. 18(5): p. 265-272.

[28] Xiao, Y.; Low, B.T.; Hosseini, S.S.; Chung, T.S.; Paul, D.R. The strategies of molecular architecture and modification of polyimide-based membranes for CO2 removal from natural gas—A review. Progress in Polymer Science. 2009. 34(6): p. 561-580.

[29] Qi, J.; Motwani, P.; Gheewala, M.; Brennan, C.; Wolfe, J.C.; Shih, W.-C. Surface-enhanced Raman spectroscopy with monolithic nanoporous gold disk substrates. Nanoscale. 2013. 5(10): p. 4105-4109.

[30] Santos, G.M.; Zhao, F.; Zeng, J.; Shih, W.-C. Characterization of nanoporous gold disks for photothermal light harvesting and light-gated molecular release. Nanoscale. 2014. 6(11): p. 5718-5724.

[31] Zhang, J.T.; Wang, L.; Lamont, D.N.; Velankar, S.S.; Asher, S.A. Fabrication of large-area two-dimensional colloidal crystals. Angewandte Chemie International Edition in English. 2012. 51(25): p. 6117-6120.

[32] El-Sayed, M.A. Some Interesting Properties of Metals Confined In Time And Nanometer Space Of Different Shapes. Accounts of Chemical Research. 2001. 34(4): p. 257-264.

[33] Dickerson, E.B.; Dreaden, E.C.; Huang, X.; El-Sayed, I.H.; Chu, H.; Pushpanketh, S.; McDonald, J.F.; El-Sayed, M.A. Gold nanorod assisted near-infrared plasmonic photothermal therapy (PPTT) of squamous cell carcinoma in mice. Cancer Letters. 2008. 269(1): p. 57-66.

[34] Putz, B.; Schoeppner, R.L.; Glushko, O.; Bahr, D.F.; Cordill, M.J. Improved electro-mechanical performance of gold films on polyimide without adhesion layers. Scripta Materialia. 2015. 102: p. 23-26.

[35] Couture, M.; Liang, Y.; Poirier Richard, H.-p.; Faid, R.; Peng, W.; Masson, J.-f. Tuning the 3D plasmon field of nanohole arrays. Nanoscale. 2013. 5(24): p. 12399-12408.

[36] Nishida, M.; Hatakenaka, N.; Kadoya, Y. Multipole surface plasmons in metallic nanohole arrays. Physical Review B. 2015. 91(23): 235406.

[37] Schwind, M.; Kasemo, B.; Zoric, I. Localized and propagating plasmons in metal films with nanoholes. Nano Letters. 2013. 13(4): p. 1743-1750.

[38] Lesuffleur, A.; Im, H.; Lindquist, N.C.; Oh, S.-H. Periodic nanohole arrays with shape-enhanced plasmon resonance as real-time biosensors. Applied Physics Letters. 2007. 90(24): 243110.

[39] Cheng, K.; Wang, S.; Cui, Z.; Li, Q.; Dai, S.; Du, Z. Large-scale fabrication of plasmonic gold nanohole arrays for refractive index sensing at visible region. Applied Physical Letters. 2012. 100: 253101.

[40] Teodorescu, F.; Queniat, G.; Foulon, C.; Lecoeur, M.; Barras, A.; Boulahneche, S.; Medjram, M.S.; Hubert, T.; Abderrahmani, A.; Boukherroub, R.; Szunerits, S. Transdermal skin patch based on reduced graphene oxide: A new approach for photothermal triggered permeation of ondansetron across porcine skin. Journal of Controlled Release. 2017. 245: p. 137-146.

[41] Teodorescu, F.; Oz, Y.; Queniat, G.; Abderrahmani, A.; Foulon, C.; Lecoeur, M.; Sanyal, R.; Sanyal, A.; Boukherroub, R.; Szunerits, S. Photothermally triggered on-demand insulin release from reduced graphene oxide modified hydrogels. Journal of Controlled Release. 2017. 246: p. 164-173.

[42] Zagorodko, O.; Spadavecchia, J.; Serrano, A.Y.; Larroulet, I.; Pesquera, A.; Zurutuza, A.; Boukherroub, R.; Szunerits, S. Highly sensitive detection of DNA hybridization on commercialized graphene-coated surface plasmon resonance interfaces. Analytical Chemistry. 2014. 86(22): p. 11211-11216.

[43] Otto, M. Staphylococcus colonizationof the skin and antimicrobial peptides. Expert Review of Dermatology. 2010. 5(2): p. 183-195.

[44] Meeker, D.G.; Jenkins, S.V.; Miller, E.K.; Beenken, K.E.; Loughran, A.J.; Powless, A.; Muldoon, T.J.; Galanzha, E.I.; Zharov, V.P.; Smeltzer, M.S.; Chen, J. Synergistic Photothermal and Antibiotic Killing of Biofilm-Associated Staphylococcus aureus Using Targeted Antibiotic-Loaded Gold Nanoconstructs. ACS Infectious Diseases. 2016. 2(4): p. 241-250.

[45] Zhu, Y.; Ramasamy, M.; Yi, D.K. Antibacterial activity of ordered gold nanorod arrays. ACS Applied Materials & Interfaces. 2014. 6(17): p. 15078-15085.

[46] Svensson, S.; Forsberg, M.; Hulander, M.; Vazirisani, F.; Palmquist, A.; Lausmaa, J.; Thomsen, P.; Trobos, M. Role of nanostructured gold surfaces on monocyte activation and Staphylococcus epidermidis biofilm formation. International Journal of Nanomedicine. 2014. 9: p. 775-794.

[47] Parreira, P.; Magalhaes, A.; Goncalves, I.C.; Gomes, J.; Vidal, R.; Reis, C.A.; Leckband, D.E.; Martins, M.C. Effect of surface chemistry on bacterial adhesion, viability, and morphology. Journal of Biomedical Materials Research Part A. 2011. 99(3): p. 344-353.

[48] Gharechahi, M.; Moosavi, H.; Forghani, M. Effect of Surface Roughness and Materials Composition. Journal of Biomaterials and Nanobiotechnology. 2012. 03(04): p. 541-546.

[49] Joshi, S.; Pellacani, P.; van Beek, T.A.; Zuilhof, H.; Nielen, M.W.F. Surface characterization and antifouling properties of nanostructured gold chips for imaging surface plasmon resonance biosensing. Sensors and Actuators B: Chemical. 2015. 209: p. 505-514.

[50] Khantamat, O.; Li, C.H.; Yu, F.; Jamison, A.C.; Shih, W.C.; Cai, C.; Lee, T.R. Gold nanoshell-decorated silicone surfaces for the near-infrared (NIR) photothermal destruction of the pathogenic bacterium *E. faecalis*. ACS Applied Materials & Interfaces. 2015. 7(7): p. 3981-3993.

[51] CarleH, A.; Nikdel, K.; Wennerberg, A.; Holmberg, K.; Olsson, J. Surface characteristics and in vitro biofilm formationon glass ionomer and composite resin. Biomaterials. 2001. 22: p. 481-487.

[52] Stylianopoulos, T.; Aksan, A.; Barocas, V.H. A Structural, Kinetic Model of Soft Tissue Thermomechanics. Biophysical Journal. 2008. 94(3): p. 717-725.

CHAPTER 3 SELECTIVE ISOLATION AND ERADICTION OF *E.COLI* ASSOCIATED WITH URINARY TRACT INFECTIONS USING ANTI-FIMBRIAL MODIFIED MAGNETIC REDUCED GRAPHENE OXIDE NANOHEATERS

3.1 Introduction

Rapid and effective separation and followed up elimination of bacteria from water, food or in clinical settings is still a challenging task. Based on the size discrimination, sedimentation, bacterial cell agglomeration or the surface charging properties, typical techniques developed for bacterial isolation and/or ablation from solutions include filtration [1, 2], centrifugation [3, 4], sonication [5] and dielectrophoresis [6]. Lately, with the great development of nanotechnology, various nanostructures have been reported for real time removal of bacteria from solutions through interaction with the particle surface as well as the ablation of pathogens due to the intrinsic antibacterial properties of these nanostructures [7-12]. This last system requires strong, efficient and selective binding of the pathogen to the nanostructures. In this regard, magnetic separation techniques based on magnetic nanostructures allow for easy removal of bacteria from different media *via* a contactless and harmless external magnet [8-10, 12-20]. In addition to the magnetic properties, the high surface/volume ratio of magnetic particles offers more contact surface area for binding pathogen ligands and subsequent capture of pathogens. Moreover, the size of these particles is typically 2 orders of magnitude smaller than a bacterium, which permits the attachment of multiple particles onto a bacterial cell, making magnetic-mediated separation much easier. Despite the promising properties of magnetic particles, however, the removal efficiency of bacteria using magnetic nanoparticles alone remains rather low (see **Section 3.3**), which may be attributed to the insufficient interaction between the nanoparticles and bacterial cells. Besides, these systems are also not highly effective in removing ultralow bacteria concentrations ($< 1\times10^2$ cfu mL^{-1}) due to unspecific interactions with other molecules and substances presented next to bacteria, limiting their practical applications. More advanced particle systems, easily separated from water, that exhibit limited nonspecific interactions and are target specific with high loading capacity at high and low bacteria concentrations would be a great advantage.

In this chapter, to overcome the above mentioned limitations of magnetic nanoparticles, a hybridization of 2-nitrodopamine coated magnetic particles (MP_{ND}) and anti-fouling reduced

graphene oxide (rGO) nanosheets are presented (**Figure 3.1**). This novel magnetic nanocomposite material combines several features: (a) a rGO/MP_{ND} based matrix offering large surface area for effective binding of bacteria, (b) good magnetic properties for the removal of bacteria, (c) decreased non-specific interaction with serum proteins due to the presence of poly (ethylene glycol) functionalized pyrene units (pyrene-PEG), (d) target specificity towards type-1 fimbriae carrying *E. coli* such as uropathogenic ones due to the integration of anti-fimbrial *E. coli* antibodies, and (e) photothermal properties which allow the eliminated pathogens to be ablated on the matrix.

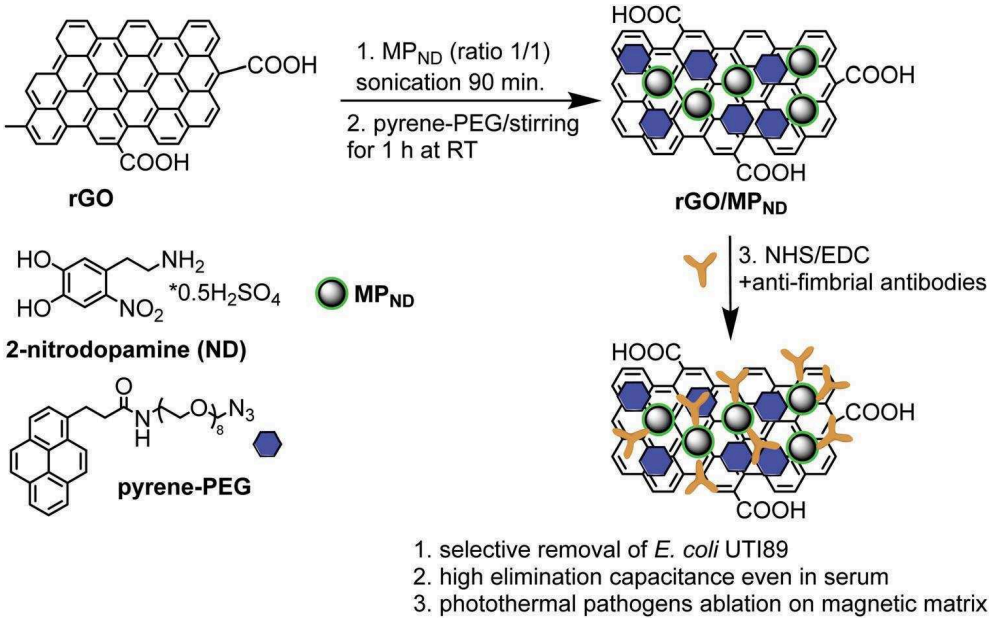

Figure 3.1: Schematic illustration of the fabrication of magnetic nanoheaters for pathogen isolation together with their different advantages.

3.2 Fabrication of magnetic reduced graphene oxide nanosheets

The fabrication of this nanostructure is based on the pre-synthesis of magnetic nanoparticles, and their integration into reduced graphene oxide (rGO) nanosheets, followed by the functionalization with pyrene-PEG as well as *E. coli* UTI89 specific anti-fimbrial antibodies (**Figure 3.1**) to obtain magnetic nanostructures with high and selective bacterial elimination efficiency, which can be used in aqueous solution as well as in more complex media such as serum.

It has been shown previously by our group that 2-nitrodopamine is an excellent ligand to stabilize iron oxide particles formed using the co-precipitation reaction of Fe^{2+} and Fe^{3+} in

alkaline media [21]. This amine-terminated ligand is indeed known to be a far superior ligand to stabilize magnetic particles than dopamine [22-24]. The higher oxidation potential of the 2-nitrodopamine ligand implies that nanoparticle surface degradation is diminished, ensuring irreversible binding of the ligands and good stability of the resulting nanostructures. These properties are crucial when using such particles for follow-up reactions and in biomedical applications. Furthermore, π–π stacking interaction of the catechol groups with the aromatic network of a rGO might be in addition favorable for the formation of stable nanostructures.

The 2-nitrodopamine coated iron oxide particles were characterized by FTIR (**Figure 3.2A**) and X-ray photoelectron spectroscopy (XPS) (**Figure 3.2B**). The FTIR spectrum of the MP_{ND} particles exhibits a band at ≈1290 cm^{-1} corresponding to C–O or NO_2 vibration. The band at 1500 cm^{-1} is due to the C=C vibration of the catechol system, which overlaps with the asymmetric vibrations of NO_2 at about 1548 cm^{-1}. The bands at 2882 and 2920 cm^{-1} are due to -CH stretching vibrations of the dopamine ligand. The broad band at 3367 cm^{-1} and the band at 1650 $cm^{-1}$are ascribed to the stretching and bending mode of primary amines, respectively. The content of nitrogen in the MP_{ND} particles determined by XPS was 3.3 at%, indicating further that 2-nitrodopamine is bonded to the surface of the magnetic particles. The amino group density was in addition determined using the UV spectroscopic method proposed by Kaiser *et al* [25]. And proposed by *Krueger* for the analysis of nanoparticles [26]. The amount of primary amino groups on the MP_{ND} particles was found to be 45±11 nM g^{-1}, in accordance with other amino functionalized magnetic particles [27].

A representative Fe_{2p} core level XPS spectrum is seen in **Figure 3.2B**. The $Fe_{2p3/2}$ region can be deconvoluted into bands at 709.01 and 711.02 eV, indicating the presence of both Fe^{2+} and Fe^{3+}species. The satellite peak at ≈717 eV is a direct evidence for the presence of Fe^{3+} in the form of γ-Fe_2O_3, suggesting that the 2-nitrodopamine coated magnetic particles are partially oxidized.

To get more insight into the structure and morphology of the MP_{ND}, transmission electron microscopy (TEM) analysis was performed by imaging a sample coated Cu grid (**Figure 3.2C**). The size of the nanoparticles is in the range of 8–10 nm. EDAX analysis displays different elements (Fe, O, C, N) present in the sample in accordance with the chemical structure of the particles. Furthermore, high resolution transmission electron microscopy (HRTEM) analysis was performed to get more information about the sample. The HRTEM

image of MP_{ND} displays fringes with a calculated fringe width of 0.283 nm corresponding to the iron oxide nanoparticles. Dynamic light scattering measurements were performed in addition to determine the hydrodynamic diameter of the particles, which was determined to be 140±50 nm.

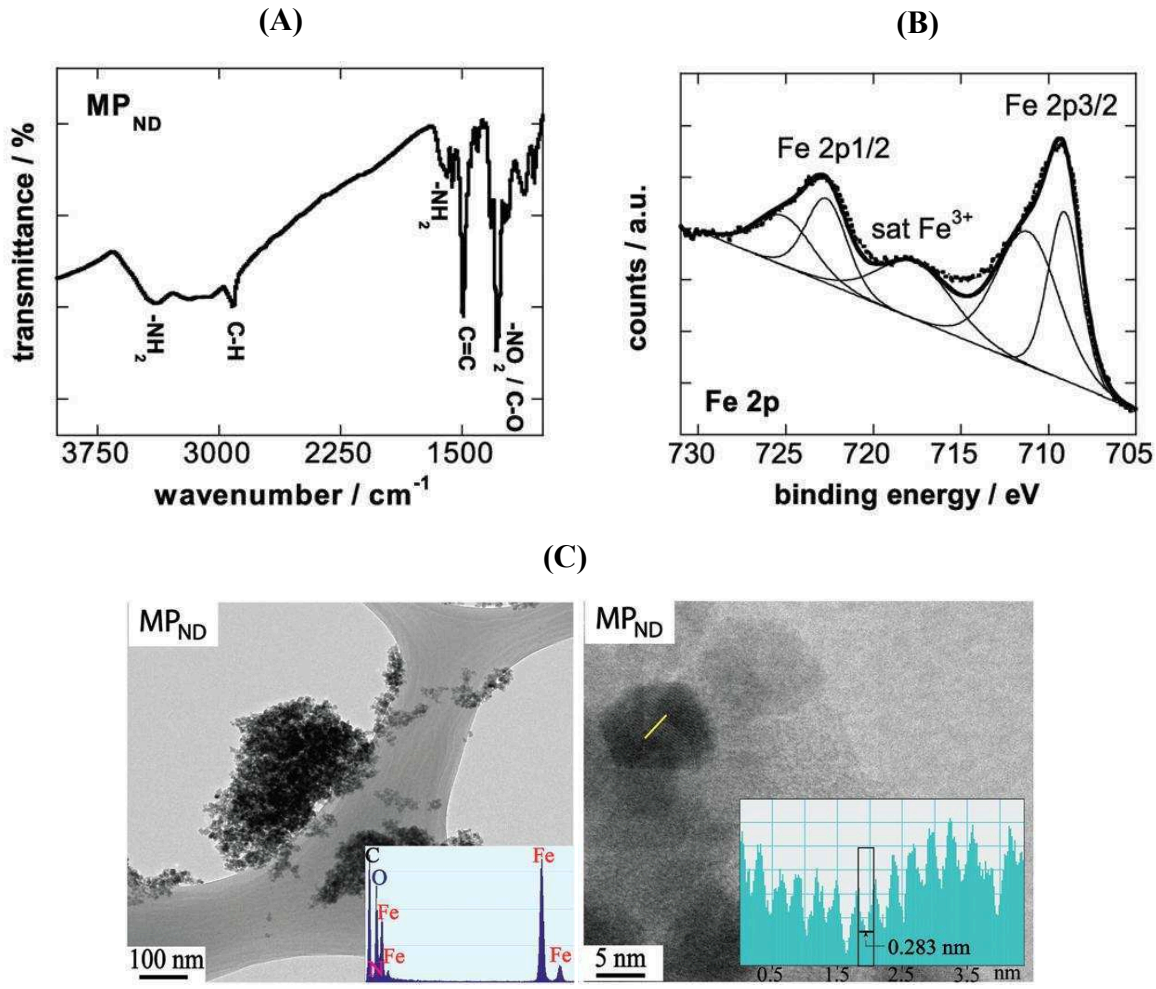

Figure 3.2: Characterization of MP_{ND}: (A) FTIR spectrum; (B) Fe_{2p} high resolution XPS spectrum; (C) Transmission electron microscopy (TEM) and HRTEM analysis (inset: EDAX analysis displaying the different elements present in the sample).

The MP_{ND} particles were incorporated with reduced graphene oxide (rGO) by mixing in a 1:1 ratio and sonicating for 2 h. The FTIR spectra of rGO before and after loading with MP_{ND} particles are displayed in **Figure 3.3A**. The spectrum of rGO is dominated by a band at ≈1570 cm^{-1} due to a C=C stretching mode of the aromatic rings. The presence of an O–H stretching vibration band (≈3430 cm^{-1}) and stretching modes due to other oxygen containing groups implies the incomplete removal of oxygen groups as expected for rGO. The bands at 1734 and 1094 cm^{-1} correspond to C=O stretching vibration of residual –COOH and C–O functions,

respectively. Loading of rGO with MP_{ND} particles results in a comparable FTIR spectrum as for rGO with additional bands at 2882 cm^{-1} (C–H stretching) and 1233 cm^{-1} due to symmetric vibrations of $-NO_2$ groups.

The UV-vis spectrum of hydrazine reduced graphene oxide (**Figure 3.3B**) displays an optical absorption peak at 273 nm with an absorption tail in the NIR characteristic of rGO. The UV-vis spectrum of the free 2-nitrodopamine ligand exhibits a prominent peak at 352 nm. The UV-vis spectrum of rGO/MP_{ND} nanostructures is comparable to that of rGO and exhibits a broad absorption maximum at 273 nm and an absorption tail until the NIR.

TEM image of the rGO/MP_{ND} hybrid reveals the integration of MP_{ND} nanostructures onto the rGO nanosheets (**Figure 3.3C**) with the overall size of the hybrid estimated to be 200± 60 nm. The surface area of the rGO/MP_{ND} hybrid was determined from N_2 adsorption–desorption isotherms as shown in **Figure 3.3D**. The N_2 adsorption-curve of MP_{ND} can be classified as typical type II without a hysteresis loop [28]. In the case of rGO/MP_{ND}, the curve is close to type IV with a weak hysteresis loop in the 0.4–1.0 relative pressure range with the specific surface area increased to 81.71 $m^2\ g^{-1}$. This increased active surface area will be favorable for the efficient removal of pathogens, as confirmed in the following experiments.

Figure 3.3E indicates the difference in colloidal stability of a rGO/MP_{ND} hybrid in water compared to rGO. While MP_{ND} particles have good colloidal stability, from the photographs in **Figure 3.3E**, it is evident that the stability of aqueous suspensions of rGO is poor. The rGO particles have completely settled on the bottom of the cuvette after 24 h. In the case of the rGO/MP_{ND} hybrid the slightly opaque color indicates that some larger particles seem to be present in the remaining solution, which have not settled after the 24 h period, indicating a good long term colloidal stability.

The saturation magnetization (MS) curves of MP_{ND} and rGO hybrids were determined (**Figure 3.3F**). The saturation magnetization value for MP_{ND} is ≈49 emu g^{-1} at 250 K. Compared to the room temperature MS value of bulk Fe_3O_4 (≈92 emu g^{-1}), the values of the MP_{ND} particles are lower as expected, due to the mass of 2-nitrodopamine coating [29]. The embedding of these nanostructures onto rGO results in a further decrease to ≈34 emu g^{-1} (**Figure 3.3F**). Ferromagnetic behavior with a coercivity of about 280 Oe is observed for both nanostructures in accordance with XPS data showing the partial oxidation of the MP_{ND} particles.

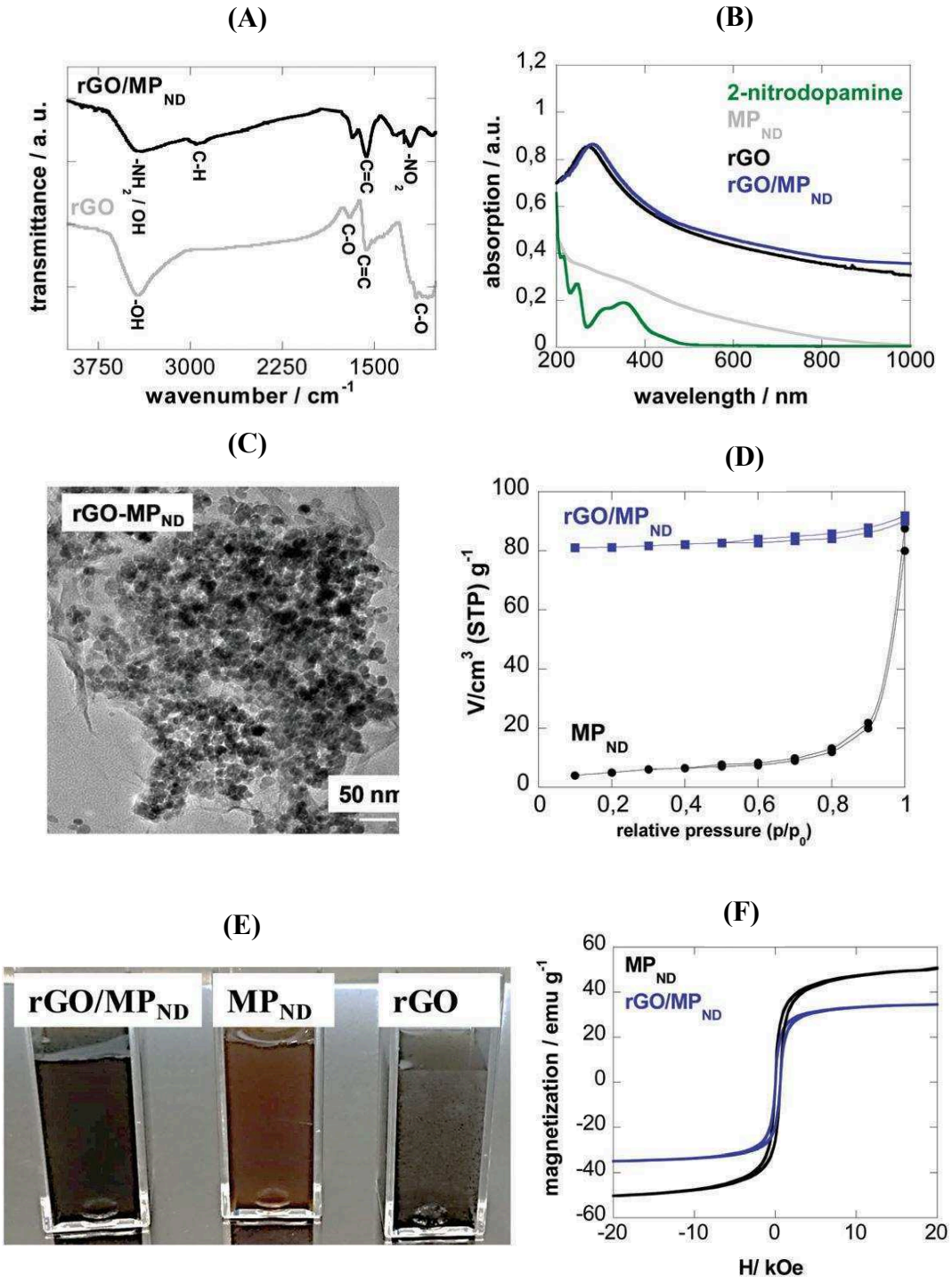

Figure 3.3: Characterization of rGO/MP_{ND} particles: (A) FTIR spectra of rGO (grey) and rGO/MP_{ND} (black); (B) UV/Vis absorption spectra of MP_{ND} (grey), rGO (black) and rGO/MP_{ND} (blue); (C) TEM image of rGO/MP_{ND}; (D) N_2 adsorption–desorption isotherms for MP_{ND} (black) and rGO/MP_{ND} (blue); (E) Photographs of aqueous dispersions of rGO, MP_{ND} and rGO/MP_{ND} (500 mg mL^{-1}); (F) Hysteresis curves of MP_{ND} and rGO/MP_{ND}.

3.3 Capture of bacterial cells

To assess the enrichment effect of rGO/MP_{ND} particles under magnetic field separation, the rGO/MP_{ND} (500 mg mL^{-1}) was incubated for up to 30 min with *E. coli* and *S. aureus* and then set on a magnet for magnetically driven sedimentation of the nanostructures with bound bacteria. As is shown in **Figure 3.4A**, MP_{ND} particles show a removal capacity of ~62% for *E. coli* and ~32% for *S. aureus*. The difference is believed to be due to the different charge states of Gram-positive and Gram-negative pathogens and that of the particles [12]. At physiological pH, MP_{ND} particles exhibit a positive charge of ~20±2 mV (**Figure 3.4B**). In contrast, both the gram positive and gram negative pathogens show negative charge at pH 7 (**Figure 3.4C**). Meanwhile, *E.coli* is more negatively charged than *S. aureus*, which is attributed to the different cell wall structures of these two strains. The surface charge results of MP_{ND} and the bacteria are consistent with the bacterial capture test, in which more negatively charged *E.coli* has stronger bonding with MP_{ND} nanoparticles. However, once attached to rGO, the importance of the surface charge of the nanocomposite is masked by the strong interaction of *E. coli* and *S. aureus* with the underlying rGO nanosheets resulting in 100% capture efficiencies for Gram-positive and Gram-negative bacteria (**Figure 3.4A**). This is probably due to the two dimensional structure of rGO, which favors the interaction site of the nanosheet with bacterial cell membrane, rendering bare magnetic nanoparticles the potent capability for the application of efficient and rapid removal of both gram positive and negative bacteria.

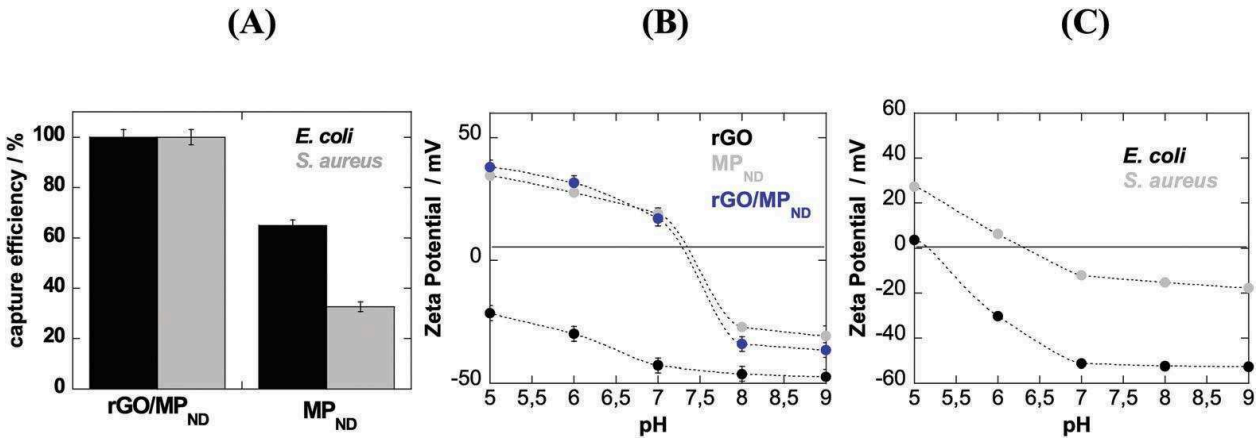

Figure 3.4: (A) Removal efficiency of MP_{ND} and rGO/MP_{ND} (500 $mgmL^{-1}$) of *E. coli* and *S. aureus* (1×10^9 cfu mL^{-1}); (B) Zeta potential of rGO, MP_{ND}, and rGO/MP_{ND} as a function of solution pH; (C) Zeta potential of *E. coli* and *S. aureus* suspensions (1×10^9 cfu mL^{-1}).

The time and concentration dependent capture efficiency of rGO/MP_{ND} was tested with *E.coli*

UTI89. As we can see in **Figure 3.5A**, 500 mg mL^{-1} of rGO/MP_{ND} resulted in complete bacterial removal in less than 30 min, while 100 mg mL^{-1} and 250 mg mL^{-1} removed about 10% and 30% of the total colonies. The capture efficiency shows a nonlinear concentration dependence (**Figure 3.5B**), with complete bacterial removal only reached at higher concentrations. From the SEM image in **Figure 3.5C**, it can be seen that the bacteria are bound to the rGO/MP_{ND} and are partly embedded in the 3D nanostructure.

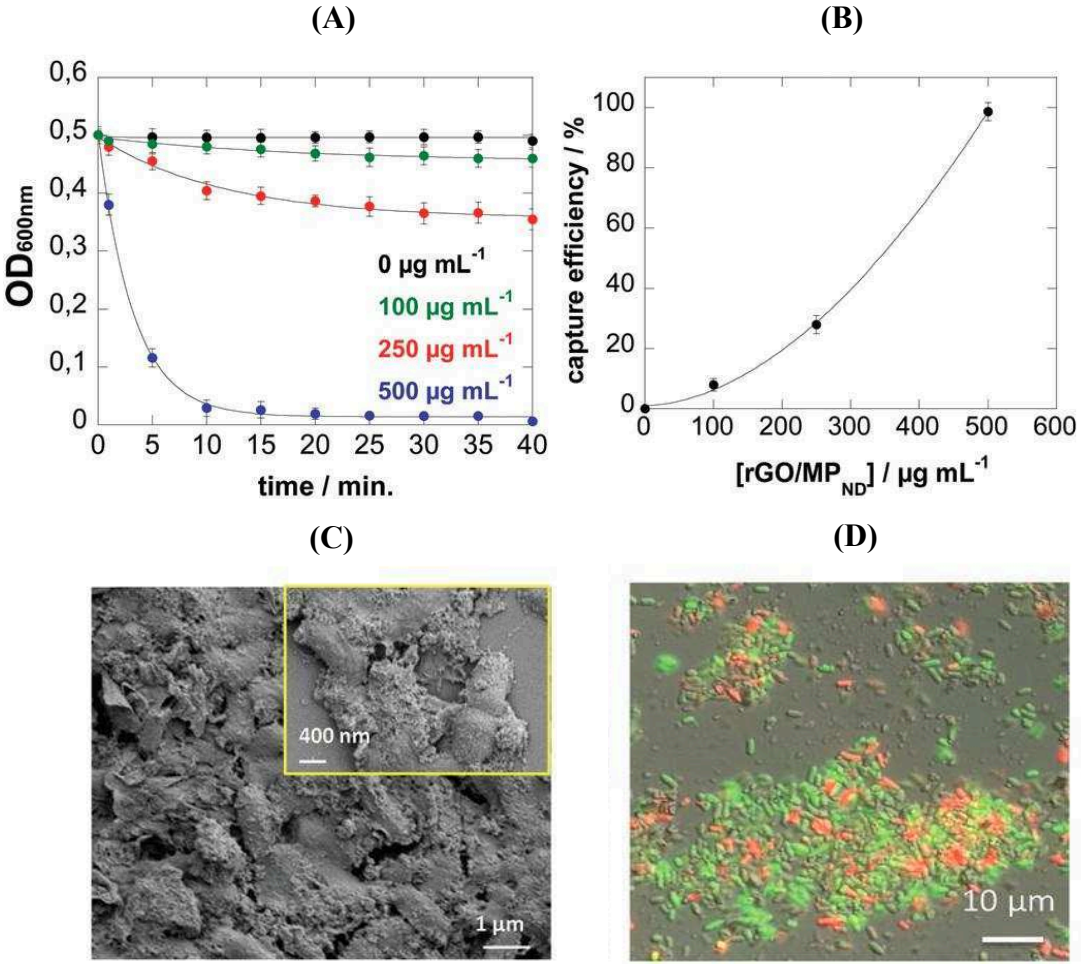

Figure 3.5: (A) Change in OD_{600} over time as a function of the concentration of rGO/MP_{ND} upon incubation in *E. coli* UTI89 (1×10^9cfu mL^{-1}); (B) Capture efficiency as a function of the concentration of rGO/MP_{ND}; (C) SEM images of rGO/MP_{ND} mediated bacterial isolation; (D) Confocal fluorescence images of live and dead bacterial cells after incubation of 500 mg mL^{-1} rGO/MP_{ND} for 30min with *E. coli* UTI89 (1×10^9 cfu mL^{-1}) and subsequent staining with SYTO 9 (green, alive) and PI (red, dead)

Graphene based matrices are reported for their strong antibacterial properties [30]. A fluorescence-based cell live/dead assay was used to investigate the removal mechanism at hand. **Figure 3.5D** shows an overlap of the fluorescence images after staining with SYTO9 and propodium iodide (PI). SYTO9 is a dye which enters through the bacterial membrane and

colors in green both living and dead bacteria, while PI staining indicates dead bacteria due to damaged cell wall membranes and gives a red fluorescent color. A significant amount of green-stained cells is observed, while the rest are showing either yellow or red color. this result indicates that bacteria eliminated by rGO/MP_{ND} are partially viable.

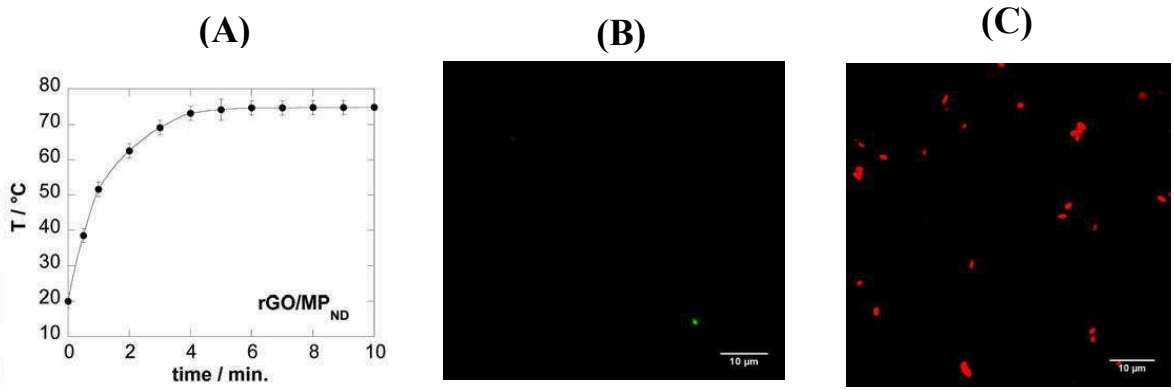

Figure 3.6: Photothermal ablation of captured bacteria and bacterial viability tested with live/dead assay. (A) photothermal heating curve of rGO/MP_{ND} (500 mg mL^{-1}) under NIR illumination at 1 W cm^{-2} in distilled water (1 mL); (B) green fluorescence and (C) red fluorescence ablated bacteria.

To ablate totally the captured pathogens, the photothermal properties of rGO/MP_{ND} in the near-infrared(NIR) were examined. NIR photothermal treatment (PTT) is known for its deep penetration into tissue and in combination with rGO nanosheets is suitable for photothermal ablation of pathogens [1, 9, 30, 31]. The effective light-to-heat conversion capability of rGO causes irreversible damage to bacterial cells and thus represents an efficient antibacterial treatment approach. Irradiation of rGO/MP_{ND} with a continuous laser at 980 nm for several minutes at a laser power of 1 W cm^{-2} results in a temperature increase for distilled water from 20±2 °C to 75±2 °C due to the photothermal heating effect (**Figure 3.6**). As is indicated in **Figure 3.6B** and **Figure 3.6C**, with a presence of significant red fluorescence, irradiation of the bacteria loaded rGO/MP_{ND} matrix for 10 min resulted thus in total ablation of all the bacterial cells.

3.4 Isolation efficiency for pathogen concentrations <1×10^4 cfu mL^{-1}

Next to the quantitative evaluation of the nanocarrier's isolation efficiency of highly concentrated pathogens solutions, analysis of the capture capabilities of bacterial suspensions ranging from 1×10^1 to 1×10^4 cfu mL^{-1} is of utmost importance as the infectious doses of highly virulent pathogens are often <1×10^1 cfu mL^{-1}. The classical plate counting method was

employed here to validate the removal capacity. The photos of plate counting for *E. coli* and *S. aureus* are depicted in **Figure 3.7**. The counted colony number of the original bacterial solution (control) is significantly different from the counted colony numbers of the solution after incubation for 30 min with rGO/MP_{ND} (500 $mgmL^{-1}$) and magnetic separation, with the original solution displaying whole covered bacterial colonies while treated solution showing almost no bacterial stains, indicating an excellent bacterial removal efficiency at ultralow concentrations. It is worth noting that, the capture efficiency of rGO/MP_{ND} remains excellent for both gram negative *E. coli* and gram positive *S. aureus* at ultralow concentrations, which renders the possibility for wide spectrum applications .

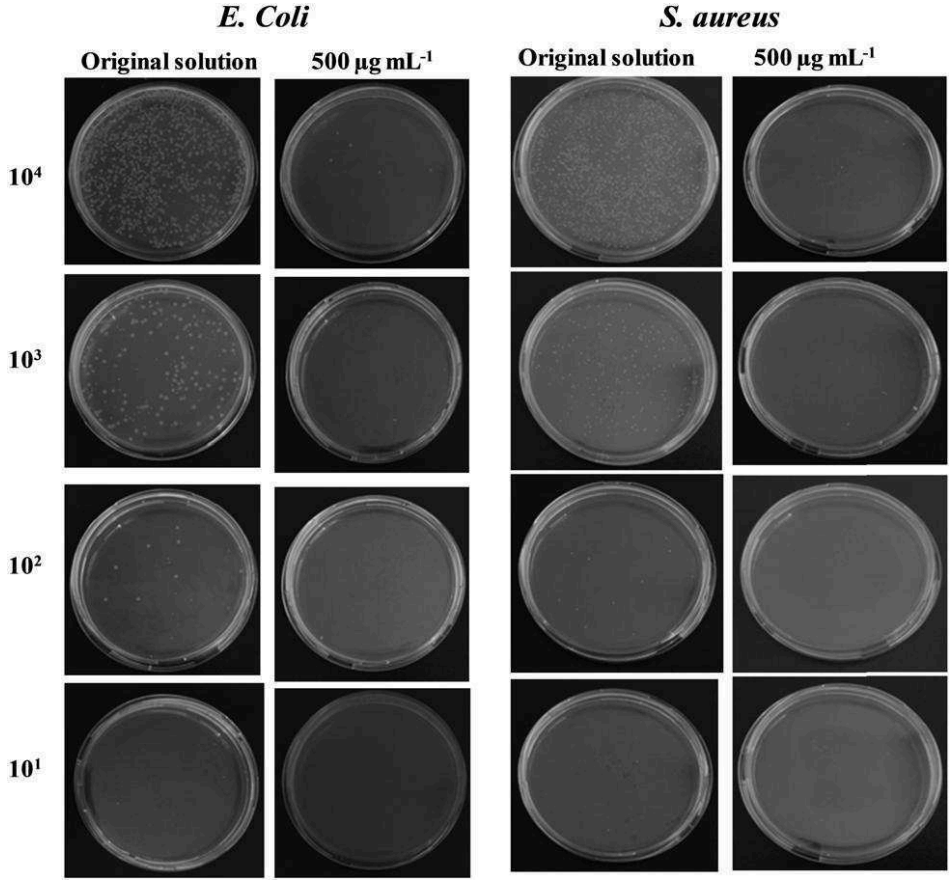

Figure 3.7: Capture and separation efficiency of rGO/MP_{ND} for *E. coli* UTI89 and *S. aureus*. Photos of plate cultures before and after treatment with rGO/MP_{ND} (500 mg mL^{-1}) for 30 min.

3.5 Specific removal of pathogenic *E. coli* UTI89

When it comes to infectious diseases, the selective removal of pathogenic species in complex media such as human serum is important. This issue can only be accomplished by adding pathogen specific targeting sites onto rGO/MP_{ND}. For sometime our group has been interested

in the development of inhibitors [32, 33] and treatments [34] for virulent strains of *E. coli* associated with urinary tract infections (UTIs). Among the targets that have been identified for the development of antiadhesive strategies are type 1 fimbriae, which constitute major virulence factors produced by *E.coli* [35]. Type 1 fimbriae are filamentous proteinaceous organelles that are distributed over the entire surface of the bacterium. To achieve selective bacteria elimination, antibodies against the major pilin protein FimA of the *E. coli* UTI89 type1 fimbriae were covalently anchored to rGO/MP_{ND} (**Figure 3.1**) using the free –NH_2 groups of the 2-nitrodopamine coating of the magnetic particles.

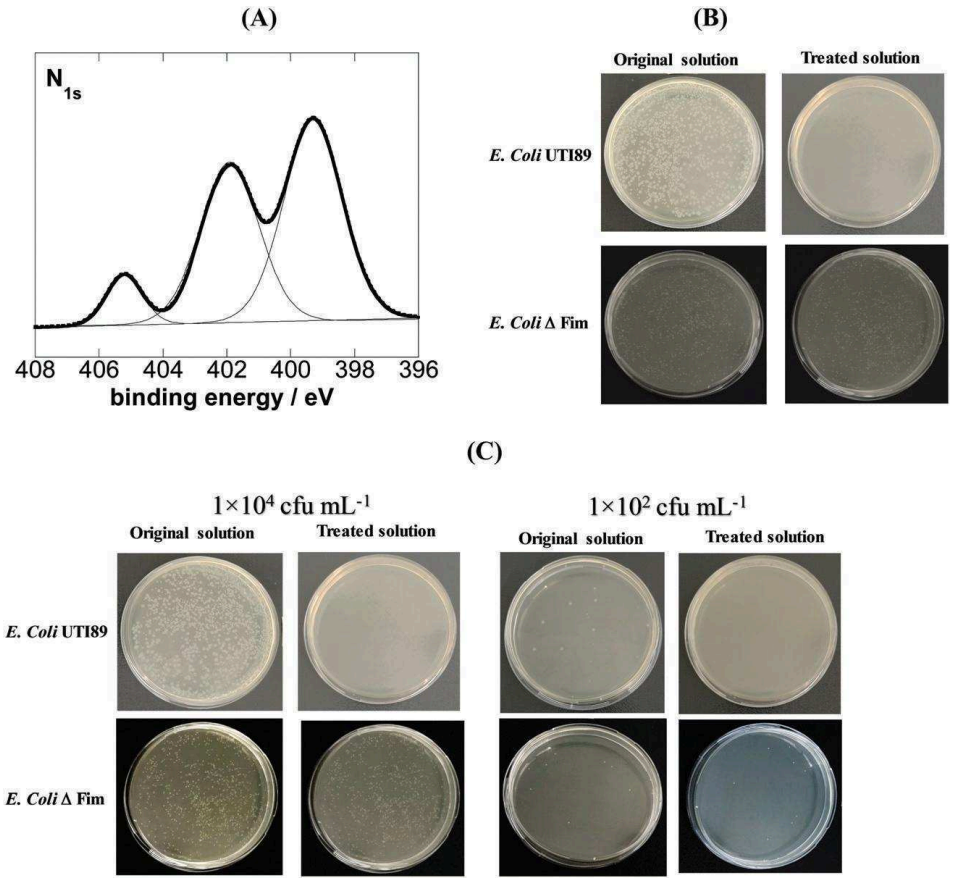

Figure 3.8: (A) N_{1s} high resolution XPS core level spectrum of azide terminated pyrene-PEG and anti-fimbrial modified rGO/MP_{ND}; (B) Photos of plate cultures of the original solution of *E.coli* UTI89 and *E. coli* Δfim at 1×10^4 cfu mL^{-1} after treatment with rGO/MP_{ND} (500 $mgmL^{-1}$) for 30 min, (C) Specific isolation of *E. coli* UTI89 over *E. coli* Δfim from human serum samples spiked with 1×10^8cfu mL^{-1} and 1×10^2 cfu mL^{-1} pathogens.

To avoid non-specific interaction with bacteria, the modified nanostructures were immersed into a solution of pyrene-PEG (**Figure 3.1**), rendering the matrix antifouling. We used an azide modified pyrene-PEG as it allowed us to validate its integration using XPS (**Figure 3.8A**). The high-resolution N_{1s} XPS spectrum of the rGO/MP_{ND} nanostructure modified

withpyrene-PEG-N_3 and anti-fimbrial antibodies reveals the azido function incorporation by the presence of signals at 405.2 ($Ar–N=N^+=N^-$) as reported for other N_3-modified interfaces [36], with the band at 401.9 eV assigned to $Ar–N=N^+=N^-$ and the–NH–C=O linkage of the pyrene-PEG and of the anti-fimbrial linkage. The band at 399 eV is due to the presence of unreacted primary NH_2 groups on the MP_{ND} particles and of the antifimbrial antibodies. The capability of these nanostructures for the selective capturing of *E. coli* UTI89 was investigated further. As seen from the photos of plate counting assays (**Figure 3.8B**) for wild type *E. coli* UTI89 and an *E. coli* UTI89 strain lacking type-1 fimbriae (UTI89 Δfim), the complete removal of *E. coli* UTI89 is achieved, while none of the non-fimbriated *E. coli* were eliminated magnetically by the matrix. The excellent results prompted us to investigate rGO/MP_{ND} nanocarriers for the removal of bacteria from contaminated serum samples. For this, serum samples spiked with 1×10^4 cfu mL^{-1} or 1×10^2 cfu mL^{-1} *E. coli* UTI89 or *E. coli* Δfim were exposed to $rGO–MP_{ND}$ (500 mg mL^{-1}) for 30 min before being magnetically separated. As seen in **Figure 3.8C**, excellent capture efficiency could be achieved even in serum indicating an excellent enrichment capability of pyrene-PEG and antifimbrial modified rGO/MP_{ND} even in serum.

3.6 Conclusion

In this chapter, anti-fimbrial modified magnetic rGO nanocomposites are demonstrated for a magnetic-separation based body fluid purification approach of *E. coli* UTI89. Owing to the large surface area of rGO and the magnetic properties of the integrated 2-nitrodopamine modified magnetic particles, the nanocomposite can rapidly capture bacteria, which can then be separated by an external magnetic field. Integration of *E. coli* UTI89 specific anti-fimbrial antibodies as well as anti-fouling pyrene-PEG enabled the selective capturing of uropathogenic *E. coli* at low and high concentration levels. Furthermore, photothermal treatment of the *E. coli* captured nanocomposite results in a complete ablation of the eliminated pathogens. While the azido groups of the pyrene-PEG in this work have only been used as an XPS marker, in the future different ‘‘clickable’’ functional ligands can be easily integrated onto these magnetic nanocomposites which will open up further means of bacterial strain differentiation and will allow the addition of further antibacterial properties onto the matrix. We thus believe that this novel multi-functional pathogen capturing matrix provides an attractive avenue for pathogen decontamination and other biomedical purposes due to high

efficiency even in complex media such as serum. While the therapeutic efficiency of *E. coli* UTI89 removal remains to be demonstrated in the clinic, the proposed approach is expected to help rapid cleaning of bodily fluids in a fast and selective manner.

3.7 References

[1] Hai, F.; Riley, T.; Shawkat, S.; Magram, S.; Yamamoto, K. Removal of Pathogens by Membrane Bioreactors: A Review of the Mechanisms, Influencing Factors and Reduction in Chemical Disinfectant Dosing. Water 2014. 6(12): p. 3603-3630.

[2] Musico, Y.L.F.; Santos, C.M.; Dalida, M.L.P.; Rodrigues, D.F. Improved removal of lead(ii) from water using a polymer-based graphene oxide nanocomposite. Journal of Materials Chemistry A 2013. 1(11): p. 3789-3796.

[3] Lambertz, S.T.; Lindqvist, R.; Ballagi-Pordany, A.; Danielsson-Tham, M.-L. A combined culture and PCR method for detecting pathogenic Yersinia enterocolitica in food. International Journal of Food Microbiology 2000. 57: p. 63-73.

[4] Lindqvist, R. Preparation of PCR samples from food by a rapid and simple centrifugation technique evaluated by detection of Escherichia coli O157:H7. International Journal of Food Microbiology 1997. 37: p. 73-82.

[5] Limaye, M.S.; Coakley, W.T. Clarification of small volume microbial suspensions in an ultrasonic standing wave. Journal of Applied Microbiology spectrum 1998. 84: p. 1035-1042.

[6] Park, S.; Zhang, Y.; Wang, T.H.; Yang, S. Continuous dielectrophoretic bacterial separation and concentration from physiological media of high conductivity. Lab Chip 2011. 11(17): p. 2893-2900.

[7] Zhu, M.; Liu, W.; Liu, H.; Liao, Y.; Wei, J.; Zhou, X.; Xing, D. Construction of Fe3O4/Vancomycin/PEG Magnetic Nanocarrier for Highly Efficient Pathogen Enrichment and Gene Sensing. ACS Applied Materials & Interfaces 2015. 7(23): p. 12873-12881.

[8] Behra, M.; Azzouz, N.; Schmidt, S.; Volodkin, D.V.; Mosca, S.; Chanana, M.; Seeberger, P.H.; Hartmann, L. Magnetic Porous Sugar-Functionalized PEG Microgels for Efficient Isolation and Removal of Bacteria from Solution. Biomacromolecules 2013. 14(6): p. 1927-1935.

[9] Jia, X.; Ahmad, I.; Yang, R.; Wang, C. Versatile graphene-based photothermal nanocomposites for effectively capturing and killing bacteria, and for destroying bacterial biofilms. Journal of Materials Chemistry B 2017. 5(13): p. 2459-2467.

[10] Liu, T.Y.; Chen, C.L.; Lee, Y.C.; Chan, T.Y.; Wang, Y.L.; Lin, J.J. First Observation of Physically Capturing and Maneuvering Bacteria using Magnetic Clays. ACS Applied Materials & Interfaces 2016. 8(1): p. 411-418.

[11] Geilich, B.M.; Gelfat, I.; Sridhar, S.; van de Ven, A.L.; Webster, T.J. Superparamagnetic iron oxide-encapsulating polymersome nanocarriers for biofilm eradication. Biomaterials 2017. 119: p. 78-85.

[12] Xiao, L.; Wu, D.; Han, S.; Huang, Y.; Li, S.; He, M.; Zhang, F.; Feng, X. Self-assembled Fe(2)O(3)/graphene aerogel with high lithium storage performance. ACS Applied Materials & Interfaces 2013. 5(9): p. 3764-3769.

[13] Fang, W.; Han, C.; Zhang, H.; Wei, W.; Liu, R.; Shen, Y. Preparation of amino-functionalized magnetic nanoparticles for enhancement of bacterial capture efficiency. RSC Advances 2016. 6(72): p. 67875-67882.

[14] Huang, Y.F.; Wang, Y.-F; Yan, A.X.-P. Amine-functionalized magnetic nanoparticles for rapid capture and removal of bacterial pathogens. Environmental Science & Technology. 2014. 44: p. 7908-7913.

[15] Arnold J. Kell; Gale Stewart; Shannon Ryan; Regis Peytavi; Maurice Boissinot; Ann Huletsky; Michel G. Bergeron; Simard, a.B. Vancomycin-modified nanoparticles for efficient targeting and preconcentration of Gram-positive and Gram-negative bacteria. ACS nano 2008. 2(9): p. 1777-1788.

[16] El-Boubbou, K.; Gruden, C.; Huang, X. Magnetic Glyco-nanoparticles: A Unique Tool for Rapid Pathogen Detection, Decontamination, and Strain Differentiation. The Journal of American Chemical Society 2007. 129: p. 13392-13393.

[17] Kaufman Rechulski, M.D.; Käldström, M.; Richter, U.; Schüth, F.; Rinaldi, R. Mechanocatalytic Depolymerization of Lignocellulose Performed on Hectogram and Kilogram Scales. Industrial & Engineering Chemistry Research 2015. 54(16): p. 4581-4592.

[18] Gu, H.; Ho, P.L.; Tsang, K.W.; Wang, L.; Xu, B. Using biofunctional magnetic nanoparticles to capture vancomycin-resistant enterococci and other gram-positive bacteria at ultralow concentration. The Journal of American Chemical Society 2003. 125: p. 15702-15703.

[19] Darabdhara, G.; Boruah, P.K.; Hussain, N.; Borthakur, P.; Sharma, B.; Sengupta, P.; Das, M.R. Magnetic nanoparticles towards efficient adsorption of gram positive and gram negative bacteria: An investigation of adsorption parameters and interaction mechanism. Colloids and Surfaces A: Physicochemical and Engineering Aspects 2017. 516: p. 161-170.

[20] Cihalova, K.; Hegerova, D.; Dostalova, S.; Jelinkova, P.; Krejcova, L.; Milosavljevic, V.; Krizkova, S.; Kopel, P.; Adam, V. Particle-based immunochemical separation of methicillin resistant Staphylococcus aureus with indirect electrochemical detection of labeling oligonucleotides. Analytical Methods 2016. 8(25): p. 5123-5128.

[21] Mazur, M.; Barras, A.; Kuncser, V.; Galatanu, A.; Zaitzev, V.; Turcheniuk, K.V.; Woisel, P.; Lyskawa, J.; Laure, W.; Siriwardena, A.; Boukherroub, R.; Szunerits, S. Iron oxide magnetic nanoparticles with versatile surface functions based on dopamine anchors. nanoscale 2013. 5(7): p. 2692-2702.

[22] Amstad, E.; Gehring, A.U.; Fischer, H.; Nagaiyanallur, V.V.; Hähner, G.; Textor, M.; Reimhult, E. Influence of Electronegative Substituents on the Binding Affinity of Catechol-Derived Anchors to Fe3O4 Nanoparticles. The Journal of Physical Chemistry C 2011. 115(3): p. 683-691.

[23] Amstad, E.; Gillich, T.; Bilecka, I.; Textor, M.; Reimhult, E. Ultrastable Iron Oxide Nanoparticle Colloidal Suspensions Using Dispersants with Catechol-Derived Anchor Groups. Nano Letters 2009. 9(12): p. 4042-4048.

[24] Amstad, E.; Textor, M.; Reimhult, E. Stabilization and functionalization of iron oxide nanoparticles for biomedical applications. Nanoscale 2011. 3(7): p. 2819-2843.

[25] Kaiser, E.; Colescott, R.L.; Bossinger, C.D.; Cook, P.I. Color test for detection of free terminal amino groups in the solid-phase synthesis of peptides. Analytical Biochemistry 1970. 34(2): p. 595-598.

[26] Jarre, G.; Heyer, S.; Memmel, E.; Meinhardt, T.; Krueger, A. Synthesis of nanodiamond derivatives carrying amino functions and quantification by a modified Kaiser test. Beilstein journal of organic chemistry 2014. 10: p. 2729-2737.

[27] Bini, R.A.; Marques, R.F.C.; Santos, F.J.; Chaker, J.A.; Jafelicci, M. Synthesis and functionalization of magnetite nanoparticles with different amino-functional alkoxysilanes. Journal of Magnetism and Magnetic Materials 2012. 324(4): p. 534-539.

[28] Zhou, G.; Wang, D.-W.; Li, F.; Zhang, L.; Li, N.; Wu, Z.-S.; Wen, L.; Lu, G.Q.; Cheng, H.-M. Graphene-Wrapped Fe3O4 Anode Material with Improved Reversible Capacity and Cyclic Stability for Lithium Ion Batteries. Chemistry of Materials 2010. 22(18): p. 5306-5313.

[29] Roca, A. G.; Marco, J. F.; del Puerto Morales, M; Serna, C.J. Effect of Nature and Particle Size on Properties of Uniform Magnetite and Maghemite Nanoparticles. Journal of Physical Chemistry C 2007. 111: p. 18577-18584.

[30] Szunerits, S.; Boukherroub, R. Antibacterial activity of graphene-based materials. Journal of Materials Chemistry B 2016. 4(43): p. 6892-6912.

[31] Gu, L.; Wang, J.; Cheng, H.; Zhao, Y.; Liu, L.; Han, X. One-Step Preparation of Graphene-Supported Anatase TiO2 with Exposed {001} Facets and Mechanism of Enhanced Photocatalytic Properties. ACS Applied Materials & Interfaces 2013. 5(8): p. 3085-3093.

[32] Khanal, M.; Larsonneur, F.; Raks, V.; Barras, A.; Baumann, J.S.; Martin, F.A.; Boukherroub, R.; Ghigo, J.M.; Ortiz Mellet, C.; Zaitsev, V.; Garcia Fernandez, J.M.; Beloin, C.; Siriwardena, A.; Szunerits, S. Inhibition of type 1 fimbriae-mediated Escherichia coli adhesion and biofilm formation by trimeric cluster thiomannosides conjugated to diamond nanoparticles. Nanoscale 2015. 7(6): p. 2325-35.

[33] Barras, A.; Szunerits, S.; Marcon, L.; Monfilliette-Dupont, N.; Boukherroub, R. Functionalization of diamond nanoparticles using "click" chemistry. Langmuir 2010. 26(16): p. 13168-13172.

[34] Turcheniuk, K.; Hage, C.-H.; Spadavecchia, J.; Serrano, A.Y.; Larroulet, I.; Pesquera, A.; Zurutuza, A.; Pisfil, M.G.; Héliot, L.; Boukaert, J.; Boukherroub, R.; Szunerits, S. Plasmonic photothermal destruction of uropathogenic E. coli with reduced graphene oxide and core/shell nanocomposites of gold nanorods/reduced graphene oxide. Journal of Materials Chemistry B 2015. 3(3): p. 375-386.

[35] Hartmann, M.; Lindhorst, T.K. The Bacterial Lectin FimH, a Target for Drug Discovery-Carbohydrate Inhibitors of Type 1 Fimbriae‐Mediated Bacterial Adhesion. European Journal of Organic Chemistry 2011: p. 3583-3609.

[36] Gouget-Laemmel, A. C.; Yang J.; Lodhi M. A.; Siriwardena A.; Aureau D.; Boukherroub R.; Chazalviel J.-N.; Ozanam F.; Szunerits S. Functionalization of Azide-Terminated Silicon Surfaces with Glycans Using Click Chemistry: XPS and FTIR Study. The Journal of Physical Chemistry C 2012. 117: p. 368-375.

CHAPTER 4 HEAT-ENHANCED TRANSDERMAL DELIVERY OF METFORMIN USING SELF-ASSEMBLY GRAPHENE-BASED HYDROGELS

4.1 Introduction

Diabetes mellitus has become one of the great healthy concerns around the world. According to the data, one out of eleven adults are suffering hyperglycemic problems while 1.5 millon die as a result [1]. Metformin hydrochloride, discovered in 1920, is a commonly used anti-hyperglycemic agent and currently the first line drug in the management of Type 2 diabetes mellitus. As is shown in Figure 4.1, different mechanisms of action of metformin on diabetes have been reported. One of the main mechanisms is to decrease hepatic glucose production. Glucose 6 phosphatase (G6P), an enzyme that is encoded by the G6P gene in hepatic cells, is responsible for the catalysis of hepatic glucose production. Metformin acts by suppressing the G6P gene expression in hepatic cells and thus decreasing hepatic glucose production. Other mechanisms include increase of peripheral insulin sensitivity in muscle and decrease of glucose absorption in gastrointestinal tract.

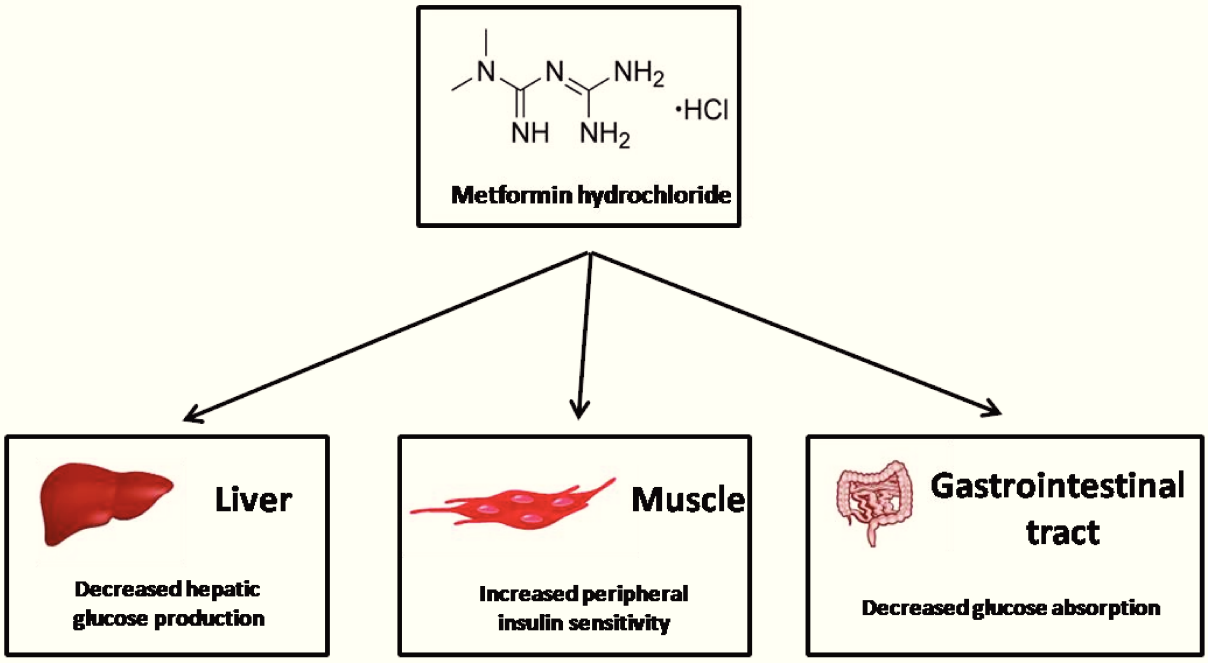

Figure 4.1: Metformin hydrochloride and its main mechanisms of action in reducing blood glucose [2].

The most common route of metformin administration is oral intake. However, several uncomfortable side effects have been reported, such as nausea, abdominal pain and indigestion, often leading to a discontinuation of the treatment. Moreover, metformin is a class III drug according to The Biopharmaceuticals Classification System, showing an unfavorable pharmacokinetics profile, having low and variable oral bioavailability (50-60 %) and half lifetime of 0.9-2.6 h [3]. As a result, frequent dosing of large quantities is thus by oral route.

Transdermal delivery of metformin has been identified as an effective alternative for patients who cannot tolerate the oral dose or have problems swallowing large tablets [4-6]. The transdermal administration route allows metformin to be absorbed into the body while bypassing the gastrointestinal tract thus avoiding many of the unpleasant side effects. To this has to be added the advantage that the daily metformin dose is only 10% of the oral one [7]. Furthermore, frequent dosing can be avoided through transdermal route as it offers sustainable drug delivery, displaying better patient compliance.

Hydrogels are unique supramolecular solid-like assemblies composed of highly cross linked network, which is capable of holding large amounts of water [8, 9]. Owing to their special properties, such as high water content, favorable structural features, hydrogels have attracted various applications, including tissue engineering, sustained drug release systems, biosensors, etc [10-12]. In the case of transdermal drug delivery of metformin, massive works have been dedicated in developing chemical hydrogel-forming microneedles based on their outstanding properties [6, 13-17]. However, Polymeric chemical hydrogels are usually formed using potentially toxic photo-initiators and cross-linkers, decreasing eventually the bioactivity of the encapsulated drug as well as limiting the release of the encapsulated drug [18]. In contrast, physical hydrogels, which are formed through hydrogen bonding, ionic interactions, hydrophobic effects or a combination of these interactions [19], possess better biocompatibility and more facile fabrication process. In addition, the weak interactions are sensitive to external stimuli such as pH, temperature and light, which can be tailored for controlled drug release [20-22].

To date, Graphene oxide (GO) based physical hydrogels have attracted much attention for controlled drug release. The large surface area of graphene sheet provides great drug loading capacity [23]. The abundant functional groups on graphene oxide, including epoxy and hydroxyl groups on the basal planar and hydroxyl and carboxyl groups at the edge, offer

different possibilities for surface modifications through covalent or noncovalent routes. Various hydrogels have been developed from GO for drug delivery. For example, H Bai *et al*. developed a GO/poly(vinyl alcohol) hydrogel for pH sensitive release of VB12 [24]. J Wu *et al*. reported a mechanically stable peptide-GO hydrogel for NIR laser triggered release of doxorubicin [25]. In the work of Tao *et al*., GO-based hydrogel with metformin as crosslinking agents was fabricated for pH sensitive release of metformin [26].

Following this idea, one pot synthesis of GO/metformin, as well as carboxylic acid enriched reduced graphene oxide(rGO-COOH)/metformin hydrogels were demonstrated in this chapter for thermal enhanced transdermal delivery of metformin. Formation of hydrogels can be achieved through hydrogen bonding and electrostatic interactions. Release of metformin can be triggered through laser irradiation due to the breakage of the weak interactions. In parallel, as is described in Chapter 1, elevated temperature can result in an increase of skin permeation, creating an integrated enhancing drug release. Photothermal activation of GO/metformin and rGO-COOH/metformin gels results in a stepwise dissolution of the gel and release of active metformin. In vitro assessment of the key target Glucose-6 Phosphatase (G6P) gene expression using Human hepatocyte model [27] confirmed that metformin activity [28] was unaffected by photothermal activation.

4.2 Photothermal effect on transdermal delivery

Before any experiment with metformin transdermal delivery, the photothermal effect on transdermal delivery was studied. Following the idea reported by our group before [29], rGO coated kapton flexible photothermal patch and NIR laser were employed as a heating setup in this study. The flexible substrate can well adapt to the shape of skin, while reduced graphene oxide, an outstanding photothermal agent, renders the possibility to incorporate the heating property. Fluorescein, chemical structure shown in **Figure 4.2A**, is a small molecule with similar molecular mass to metformin. It was used as a model drug to favoring fluorescent observation, which can be used as an indication to mark the depth of drug diffusion through skin [30]. The experimental setup is depicted in **Figure 4.2B**, human skin was mounted onto Franz cells, followed by the application of a drop of fluorescein solution. The skin was subsequently covered with a rGO-kapton photothermalpatch and irradiated with a NIR laser to trigger photothermal effect. After 6 h drug diffusion, the treated skin was sectioned in a cryostat and subjected to fluorescence observation.

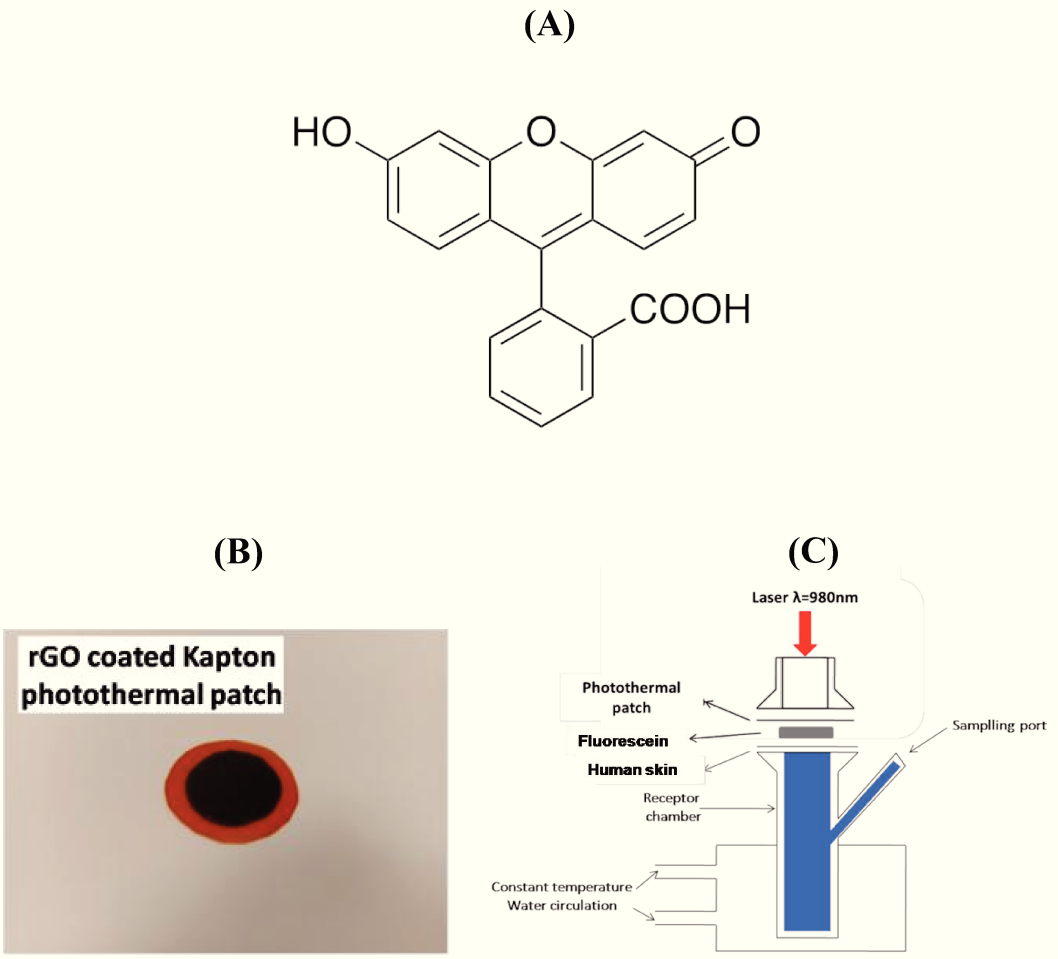

Figure 4.2. Heat-enhanced transdermal delivery of fluorescein. (A) Chemical structure of fluorescein; (B) Picture of rGO-Kapton photothermal patch; (C) Schematic illustration of experimental setup.

As is mentioned in **Chapter 1**, highly condensed structure of stratum corneum acts as the main barrier to transdermal drug release. As we can see from the sectioned images in **Figure 4.3**, stratum corneum covers the outermost layer of skin and displays a thickness varying from 50 μm to 100 μm. Fluorescent image of the skin without irradiation shows that the diffusion of fluorescein is dramatically hampered by stratum corneum as no fluorescence is found beyond the layer of SC, which is in line with the previous studies. In contrast, when the skin was subjected to laser irradiation for 10 min under 1 W cm^{-2}, which led to a final heating temperature of 60 ˚C, the great barrier was overcome and SC became permeable to the modal drug as the fluorescence is found throughout the skin layer, suggesting a superior enhancing effect compared to the control group.

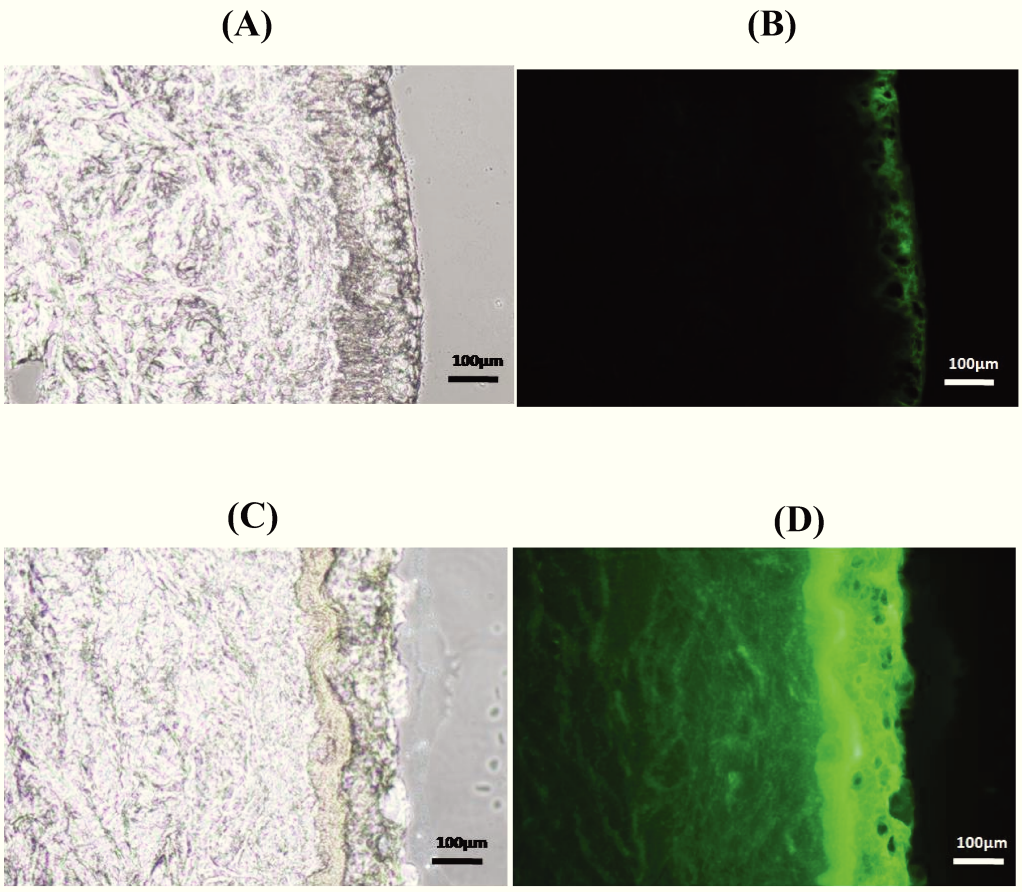

Figure 4.3: Frozen sectioned images of transermal drug delivery. (A) White field and (B) fluorescent image of untreated skin; (C) white field and (D) fluorescent image of photothermal treated skin. 100 µg of fluorescien in PBS was placed onto skin and subsequently coverd with rGO-kapton photothermal patch. The system was irradiated with 980nm laser at 1W/cm^2 for 10min, reaching a final heating temperature of 60 ˚C. Diffusion was left for 6h before cutting for fluorescent images.

As we can see form **Figure 4.4**, a dark channel can be found in the white field picture of the skin, correlating to strong fluorescence. The heat gradient is thus able to create micropores on the skin through which drug can pass, which is in line with the results that have been reported by previous studies [31, 32].

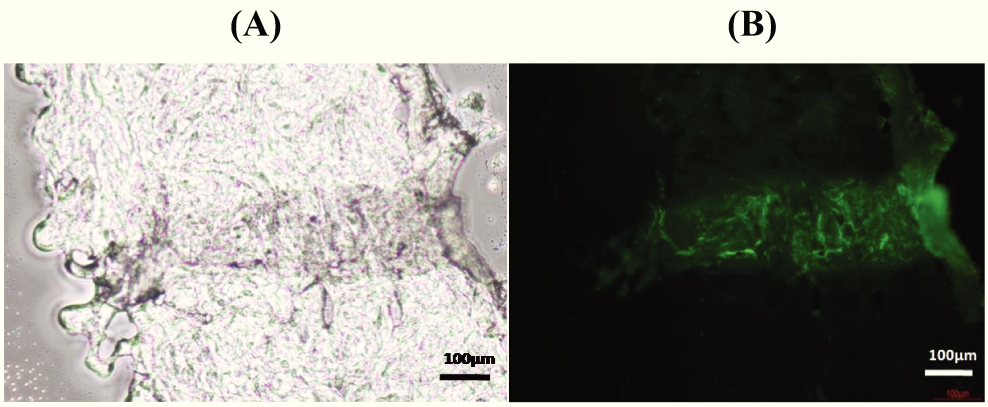

Figure 4.4: Transdermal delivery through created pathway. (A) White field image of skin with existed pathway; (B) Enhanced fluorescein permeation through the pathway over other part of skin.

4.3 Self-assembly GO/metformin hydrogel for heat enhanced transdermal delivery of metformin

4.3.1 Formation of GO/metformin hydrogel

Figure 4.5A shows the mechanism of hydrogel formation using GO as a cross linker. It can be formed under mild conditions by mixing GO/metformin in a weight ratio of 10/1. The rapid crosslinking process enables an instant formation of GO/metformin hydrogel. As is shown in the tube-inverting test (**Figure 4.5B**), comparing to GO solution alone, the mixture of GO and metformin displays a great increase of viscosity, indicating a successful formation of hydrogel. The obtained hydrogel was then lyophilized and the dried GO/metformin gel shows a fluffy structure (**Figure 4.5C**).

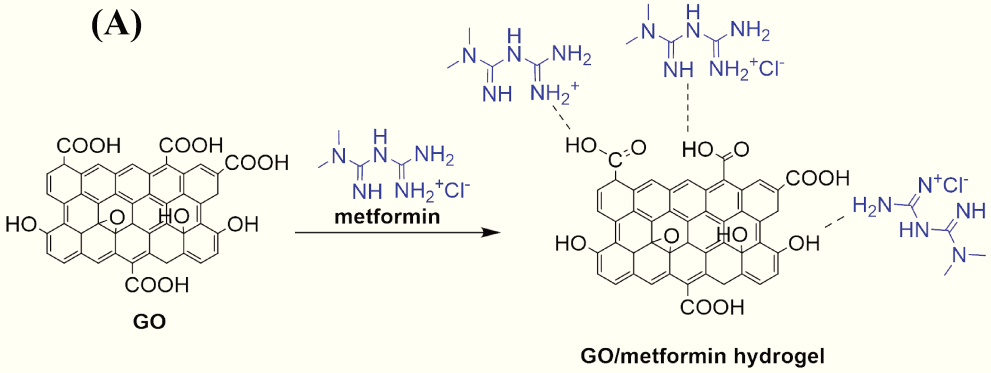

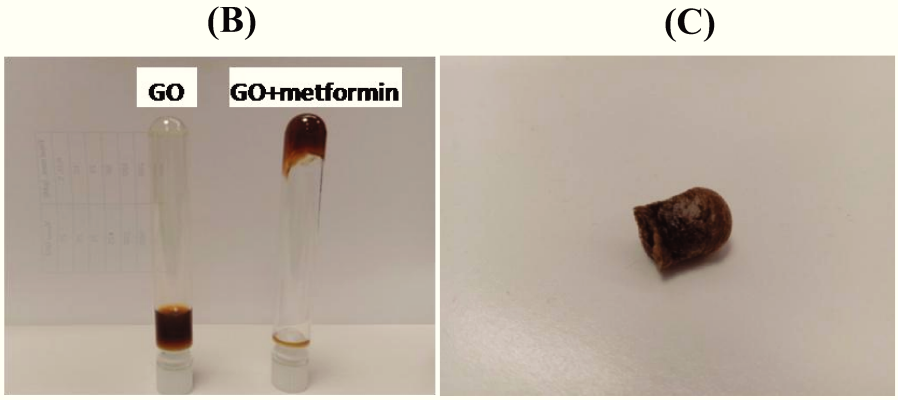

Figure 4.5: Formation of GO/metformin hydrogel. (A) The crosslinking between GO and metformin hydrochloride; (B) Tube-inverting test of GO solution and GO solution mixed with metformin hydrochloride; (C) Image of lyophilized GO/metformin hydrogel.

The SEM images (**Figure 4.6A**) of the gel demonstrates a 3D structure, while zoomed image displays a grid like morphology, in which graphene nanosheet serves as skeleton with an approximate hole size of 10±5 μm. The XPS spectrum of GO (**Figure 4.6B**) shows the presence of C and O elements with a C/O ratio of 2.1, which implies the abundance of oxygen-containing functional groups. In contrast to GO alone, N element is further determined in the spectrum of GO/metformin, indicating the presence of metformin. The content of nitrogen is identified as 5.4 at%, which is in line with the mixing ratio of GO and metformin. The C1s high resolution spectrum of GO/metformin (**Figure 4.6C**) shows bands at 284.6, 286.6 and 288.3 eV corresponding to C=C, C-O/C-N and C=O. These functional groups are expected to form strong bonding with metformin. Indeed, as metformin lacks any aromatic structures, the fast gelation process at room temperature is considered to be attributing to the strong hydrogen boding and electrostatic interactions between graphene oxide and metfomine. The N1s high resolution spectrum of GO/metformin (**Figure 4.6D**) displays a peak at around ~400 eV, which corresponds to C-NH_2 group. **Figure 4.6E** shows the characteristic Raman feature for GO and the GO/metformin gel with the G band centered at around 1585 cm^{-1} corresponding to the in-plane sp^2 C-C stretching, and the D band at 1350 cm^{-1} due to the defects. The ratio of I_D/I_G is 0.76 for GO and increased to 0.93 for GO-metformin arguing for an increase in defects due to the gelling process. The UV/Vis spectrum of GO/metformin was collected by crushing the gel and dispersing in water, as is shown in **Figure 4.6F**, a strong absorption band in the ultraviolet at 232 nm characteristic of metformin as well as to a π- π * contribution of GO , the shoulder at ≈310 nm corresponding to an n- π * plasmon peak [33], the absorption tail is lasting until the near-infrared region. The

photothermal heating curve of GO/metformin is in accordance with the UV/Vis spectrum, showing moderate heating capacity under irradiation with 980 nm laser at 1 W cm^{-2} (**Figure 4.6G**), resulting in a solution temperature of 41 °C.

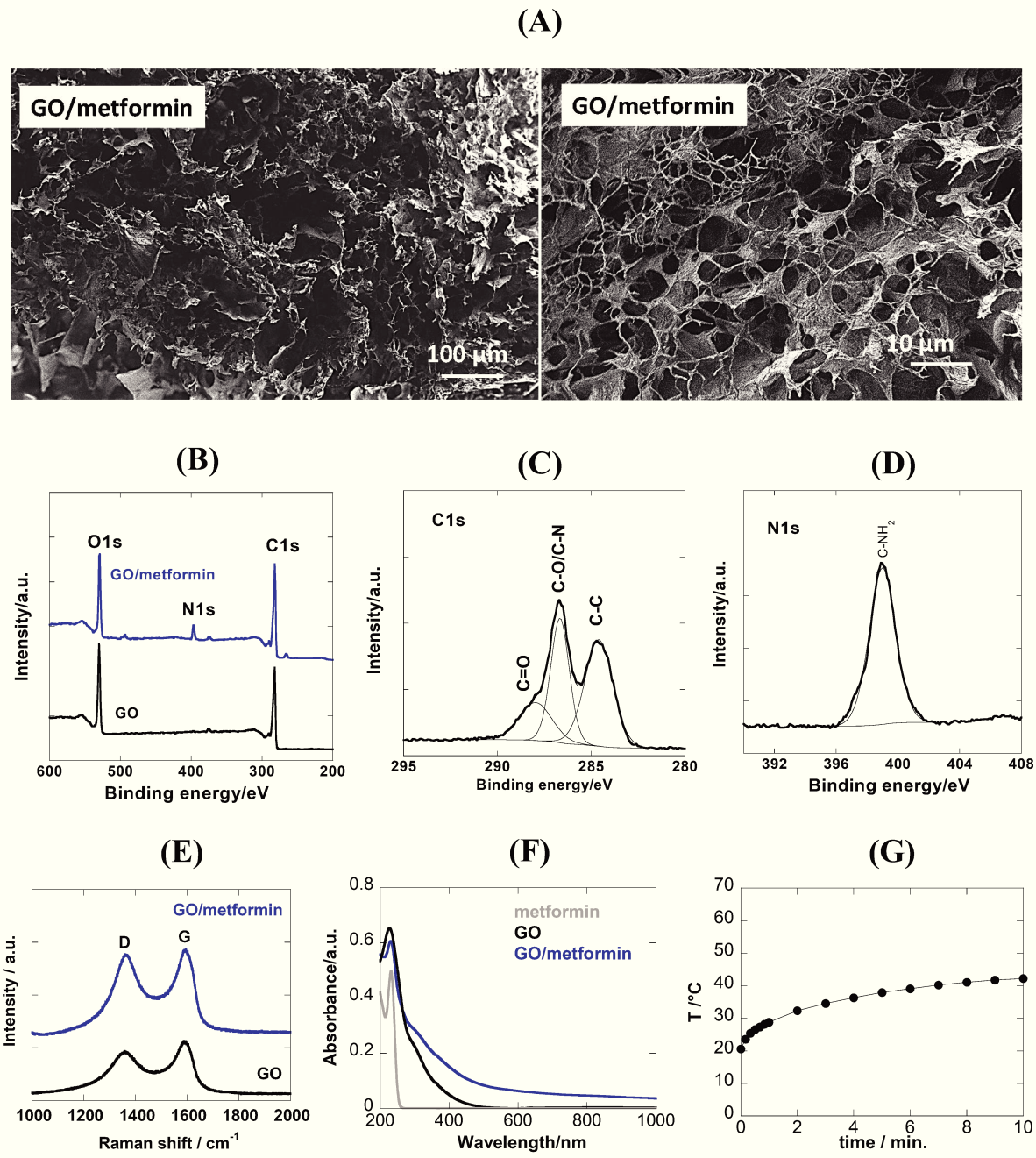

Figure 4.6: Characterizations of GO/metformin hydrogel. (A) SEM images of GO/metformin hydrogel; (B) XPS spectra for GO (black) and GO/metformin (blue); (C) C1s high resolution XPS spectra for GO/metformin; (D) N1s high resolution XPS spectra for GO/metformin; (E) Raman spectra of GO/metformin hydrogel and GO; (F) Comparison of UV/Vis spectra of metformin, GO and GO/metformin; (G) Heating curve of GO/metformin under irradiation of 980 nm laser for 10min at a power density of 1W cm^{-2}.

4.3.2 Metformin release in solution with GO/metformin hydrogel

The stability of the GO/metformin hydrogel is strongly pH dependent (**Figure 4.7A**). Immersion of GO/metformin gel into NaOH (0.1 M, pH 12) results in a fast decomposition of the gel most likely due to the deprotonation of –COOH groups of GO under basic conditions, decreasing hydrogen bonding occurrence with metformin. With a pKa of 12.4 for metformin breaking of electrostatic interactions with negatively charged GO can occur as well. Lowering the pH reduces the degree of negative charge on GO (**Figure 4.7B**) and electrostatic interaction, however hydrogen-bonding between GO and metformin limits the full collapse of the GO/metformin hydrogel until pH 3. The release profile of metformin at ambient conditions (T=23°C) was studied by immersing the gel into different pH for 6 h and quantified with HPLC. As we can see from **Figure 4.7D**, the releasing profile is in accordance with the stability of the GO/metformin gels. A release of about 10 μg mL^{-1} between pH 7 and 9, while the instability of the gel at pH 12 results in a complete release of metformin as expected. pH 5 and 3 resulted in an accumulative release of around 18 and 20 μg mL^{-1} respectively, the slightly increase of metformin release is attributed to the weakened electrostatic interaction between metformin and GO under acidic pH. As skin pH is acidic ranging from 4-6 [34], the fabricated hydrogel is thus favorable for transdermal delivery of metformin.

The effect of photothermal heating on metformin release from the gels immersed in PBS (pH 7.4) was further assessed. As depicted in **Figure 4.7E**, photothermal heating using a laser density of 1 W cm^{-2} (corresponds to a steady-state temperature of 41°C) leads to improved metformin release from the GO/metformin gel, where about 12 μg (12%) of metformin is released per laser activation, while without activation a total amount of 9 μg (9%) is released in the first two hours and then remains constant. The amount of metformin released is comparable to other reports using NIR melting microneedles with metformin release between 12-24% [14-17].

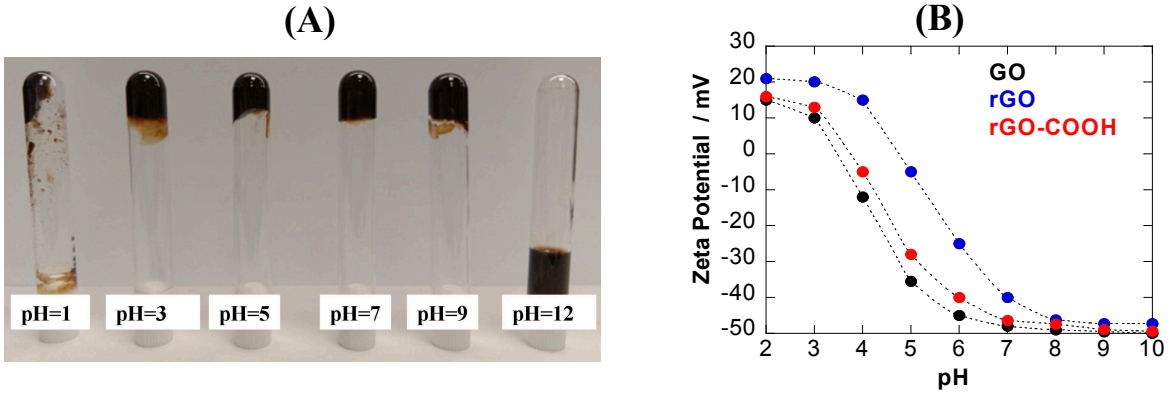

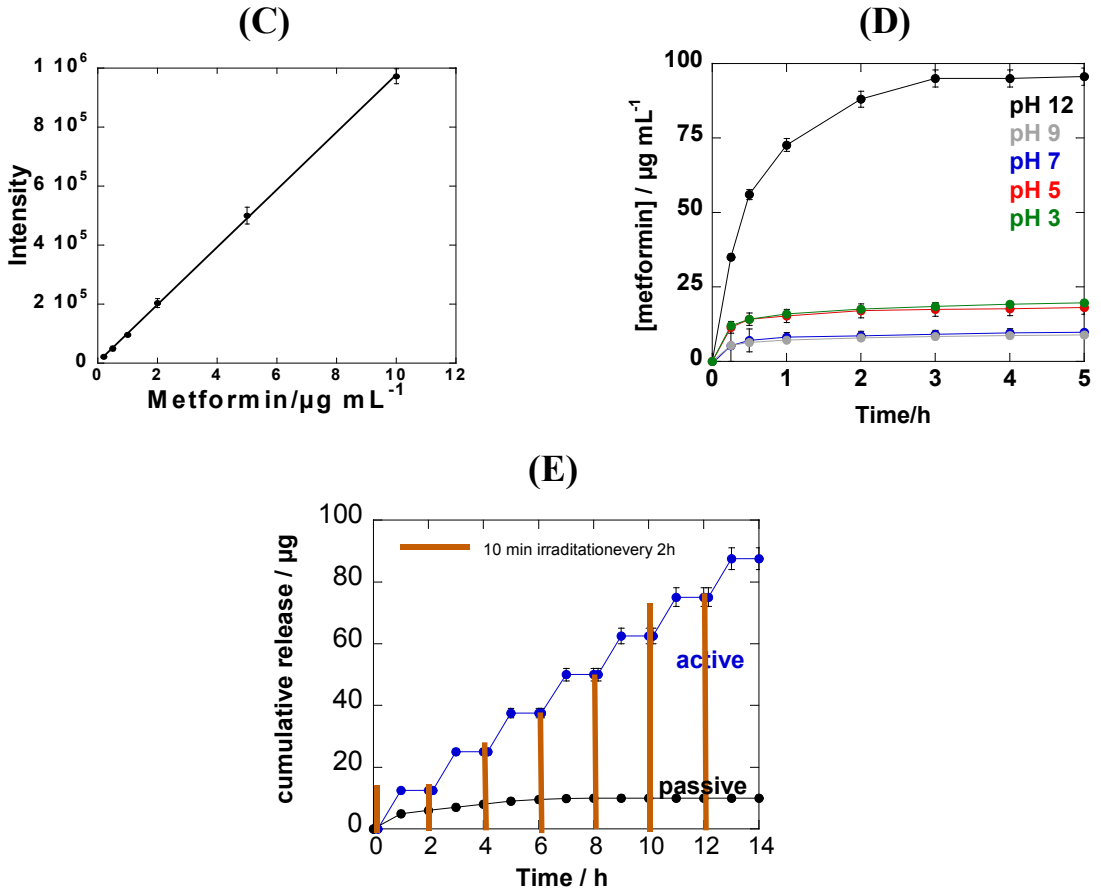

Figure 4.7: Metformin release profile in solution with GO/metformin hydrogel. (A) Stability of hydrogel in different pH; (B) Zeta potential of GO, rGO and rGO-COOH as a function of solution pH; (C) HPLC calibration curve of metformin at different concentrations; (D) Release profiles of metformin from freeze-dried samples upon immersion into solutions of different pH (3, 5, 7, 9, and 12). The data points are averaged over three parallel experiments; (D) Metformin release from GO/metformin gel into PBS (pH 7.4) upon photothermal irradiation of the GO/metformin gel at 980 nm (10 min at 1 W cm-2 every 2 h) in comparison to passive release.

4.4 Self-assemblyrGO-COOH/metformin hydrogel for heat enhanced transdermal delivery of metformin

Although metformin can be released and pass through skin with GO/metformin hydrogel, the amount is rather low comparing with previous study [7]. Metformin release was confined probably due to the compressing effect by the application of photothermal patch. Fabrication of metformin hydrogel with better photothermal property is thus of great importance. In fact, the suboptimal absorption of NIR light by the highly oxidized GO and the subsequent high dose/power needed for photothermal therapy can be improved by using reduced GO (rGO) [35-40]. Partial restoration of the aromatic network in rGO affords a significant increase in

NIR absorbance and rGO has become of particular interest as highly effective photothermal agent. However, as can be seen in **Figure 4.8**, rGO crosslinking properties is rather weak due to absence of hydroxyl and carboxylic functions needed for hydrogen bonding formation and electrostatic interactions with metformin.

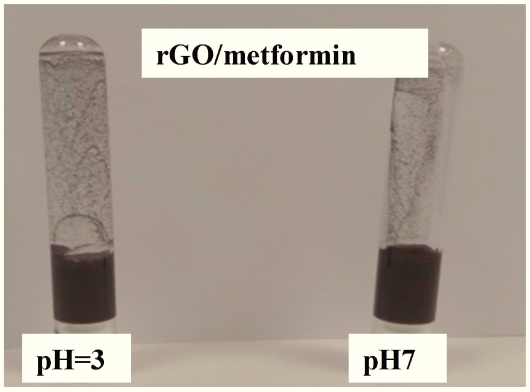

Figure 4.8: Hydrogel formation with rGO and metformin at pH=3 and pH=7.

4.4.1 Formation of rGO-COOH/metformin hydrogel

The other route is the enrichment of GO with carboxylic acid groups through chemical reaction with chloroacetic acid under strong basic conditions (0.7 M) and simultaneous reduction at 80 °C. The epoxy and ester groups present on GO surface are converted under these conditions to hydroxyl groups, which in turn are transformed into carboxylic acid -COOH moieties *via* reaction with chloroacetic acid. Performing the carboxylation reaction at 80 °C results in the formation of rGO-COOH with the electronic conjugation within the GO nanosheetbeing partially restored (**Figure 4.9A**). Indeed, this material has been presented by our group for photothermal ablation of bacteria, the partially restored graphene grid offered good photothermal property while abundant carboxylic acid groups enabled chemical decoration [41]. The UV/Vis spectrum (**Figure 4.9B**) shows an increased absorption tail in the NIR region, which is indicative for the restoration of graphene carbon grids. Then the obtained rGO-COOH was mixed with metformin in a ratio of 10/1 to fabricate rGO-COOH/metformin hydrogel. As we can see from **Figure 4.9C**, the mixture of metformin and rGO-COOH at pH=8 and pH=9 can significantly increase the velocity of the solution but still not enough to support a complete formation of hydrogel. This is due to the conversion of the functional groups into -COOH groups, while majority of the -COOH groups are deprotonated to -COO- at basic pH, only part of the groups participated in the formation of hydrogen bonds. Further decrease of pH to 7 and 5 resulted in the formation of hydrogel owing to the

protonation of -COOH, as well as the decrease of electronegativity that impedes the interaction between graphene sheet. Similar to GO/metformin hydrogel, rGO-COOH/metformin hydrogel collapses in strong basic conditions (pH=12), owing to the breakage of hydrogen bonding and electrostatic interactions.

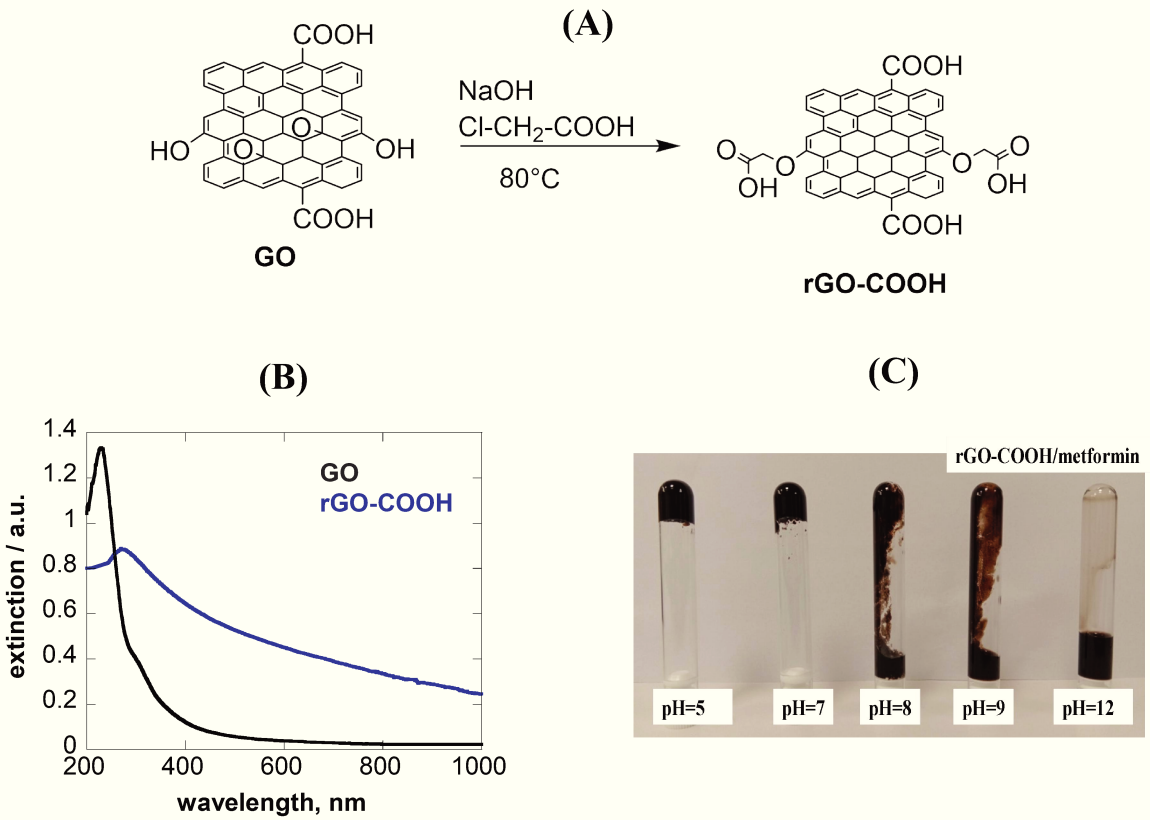

Figure 4.9: Formation of GO-COOH/metformin hydrogel. (A) Formation mechanism of rGO-COOH; (B) UV/Vis spectra of GO and rGO-COOH; (C) pH dependent formation of rGO-COOH/metformin hydrogels.

From the SEM images in **Figure 4.10A** a porous structure is still observed with the average of the pores of 25 ±10 nm, which is slightly larger than GO/metformin hydrogel. The XPS spectrum of rGO-COOH (**Figure 4.10B**) indicates the presence of C and O elements with a C/O ratio of 3.0, which is higher than GO, suggesting the reduction of graphene oxide. N element is determined to be 5.3 at% in rGO-COOH/metformin, which is in line with the result obtained for GO/metformin, as well as the ratio added in the fabrication of the gel. The high resolution C1s spectrum of rGO-COOH/metformin (**Figure 4.10C**) displays peaks at 284.6, 286.6, 288.5 and 292.7 eV, corresponding to C-C, C-O/C-N, C=O and O-C=O, respectively. Compared with GO, C-O bonding is largely decreased on rGO-COOH, while on the other hand C=O and O-C=O groups increased, indicating the successful conjugation of acetic acid groups. Though the functional groups have been greatly changed, hydrogen bonding can still

be formed with the new formed groups. As is shown in the high resolution N1s spectrum of rGO-COOH/metformin (**Figure 4.10D**), peak around 400 eV is still found, which is related to C-NH_2 groups attributed to the presence of metformin. Raman spectra of rGO-COOH and rGO-COOH/metformin show that the I_D/I_G ratio increases slightly from 0.84 to 0.87 (**Figure 4.10E**) owing to the defects formed in gellation process, which is in line with the result obtained in GO/metformin hydrogels. The photothermal properties have been largely improved when compared to GO/metformin, reaching temperature of 61°C in 10 min with irradiation of a 980 nm laser at 1 W cm^{-2} (**Figure 4.10F**) and temperature of 52 °C and 43 °C for laser powers at 0.7 and 0.5 W cm^{-2}, respectively.

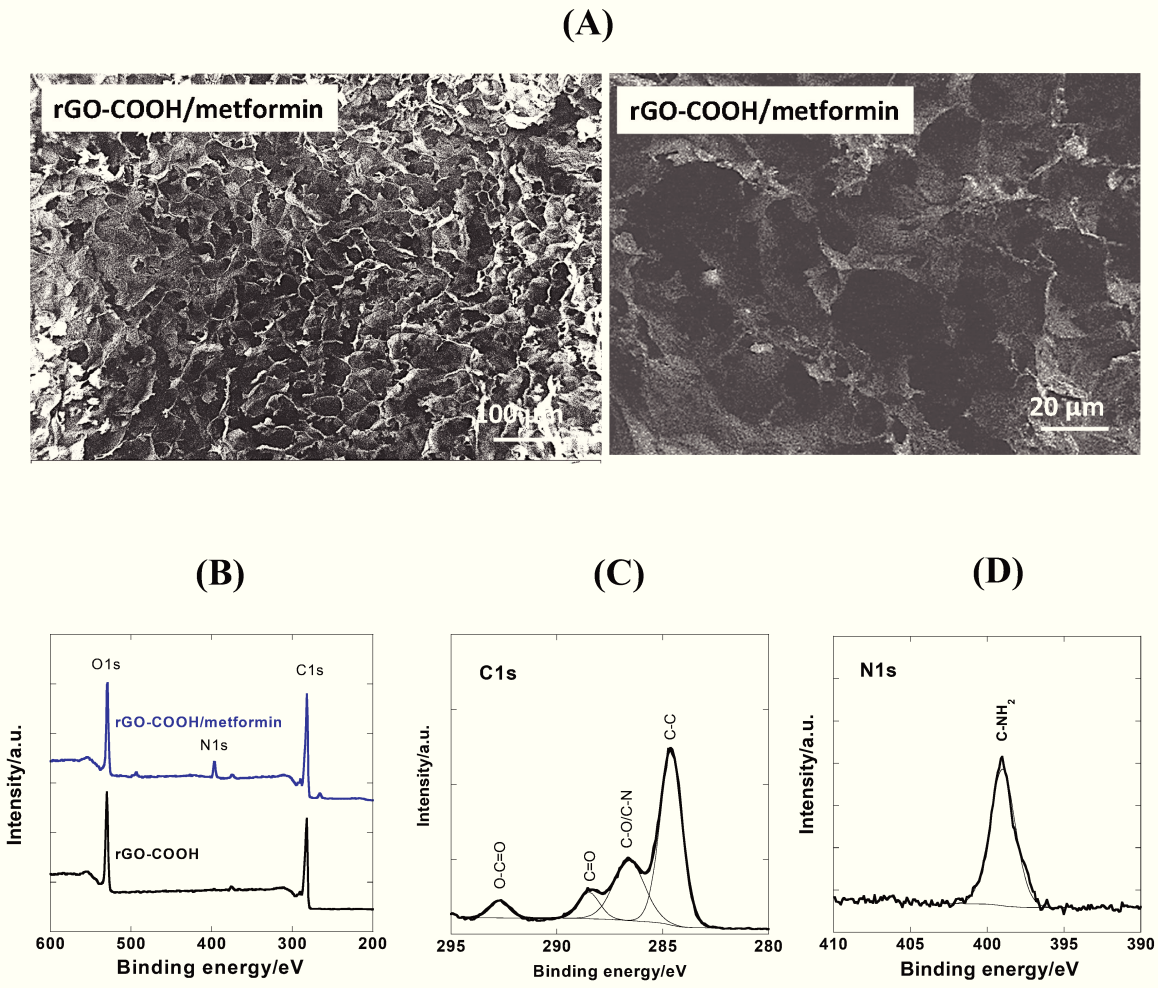

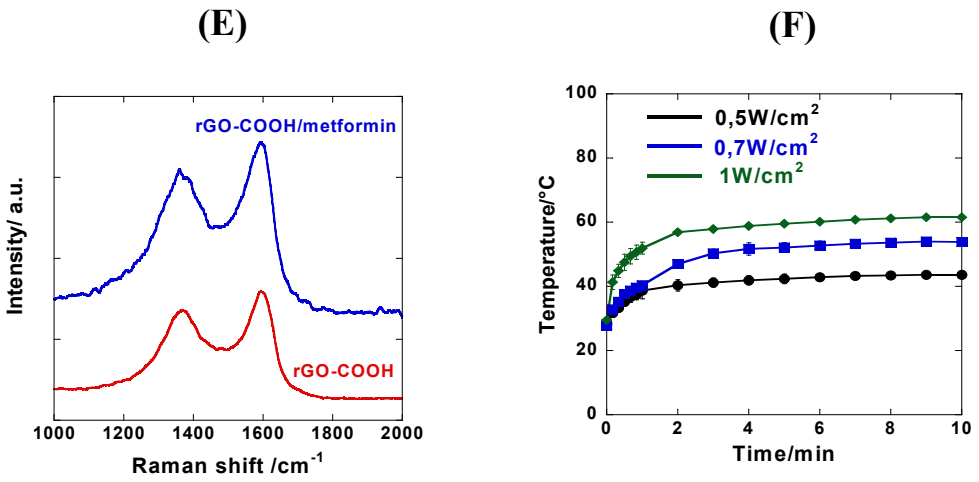

Figure 4.10: Charaterizations of rGO-COOH/metformin. (A) SEM images of rGO-COOH/metformin hydrogels; (B) XPS spectra for rGO-COOH (black) and rGO-COOH/metformin (blue); (C) C1s high resolution XPS spectrum for rGO-COOH/metformin; (D) N1s high resolution XPS spectrum for rGO-COOH/metformin; (E) Raman spectra of rGO-COOH and rGO-COOH/metformin; (F) Heating curve of rGO-COOH/metformin hydrogel with 980 nm laser irradiation for 10 min at different power densities.

4.4.2 Metformin release in solution with rGO-COOH/metformin hydrogel

Release of metformin from rGO-COOH/metformin into solution was carried out similarly as GO/metformin. The release into different pH shares the same trend with GO/metformin, as we can see from **Figure 4.11A**, pH=7 led to a total release of 18 µg out of 100 µg in 6 h, while the decrease of pH resulted in an increase of release, with 27.2 µg and 32 µg found in pH=5 and pH=3 respectively. Strong basic condition induced a burst release of metformin due to the collapse of the hydrogel. Temperature responsive release was studied through laser irradiation at 1 W cm^{-2} for 10 min every 2 h and monitoring the release for 6h (**Figure 4.11B**), The better heating ability of rGO-COOH resulted in an increased metformin release from the gel upon laser activation at 1 W cm^{-2} (corresponding to a steady-state temperature of 61 °C) where about 25 µg (21%) of metformin is released per laser activation (resulting in a total of 75 µg for 3 laser activation cycles of 10 min each). Passive release is increased due to the larger pore size attaining a total amount of 11 µg (11%) in the first two hours and then remains constant.

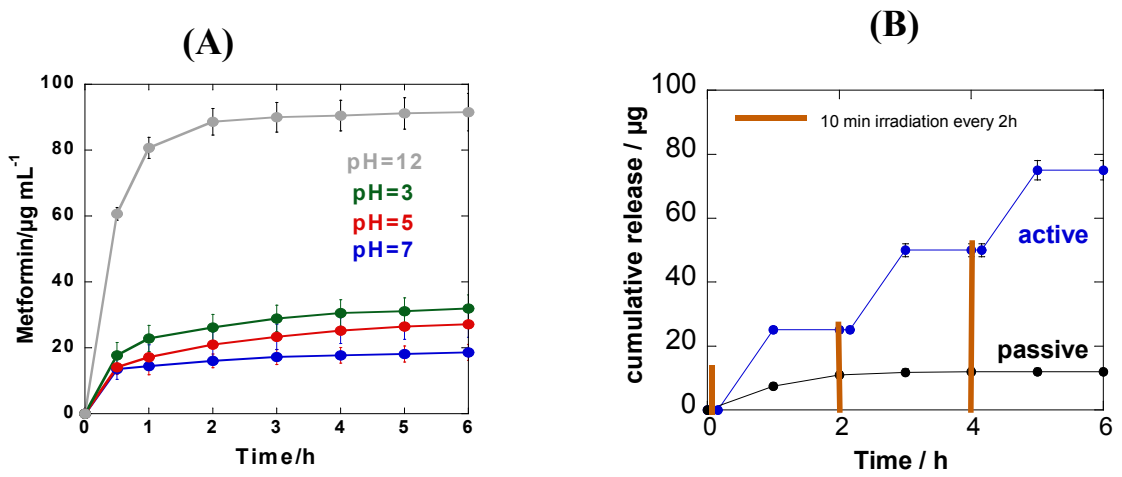

Figure 4.11: Release profile of rGO-COOH/metformin hydrogel in solution.(A) metformin release in different pH with rGO-COOH/metformin hydrogel for 6 h; (B) Metformin release from a rGO-COOH/metformin gel into PBS (pH 7.4) upon photothermal irradiation of the GO/metformin gel at 980 nm (10 min at 1 W cm^{-2} every 2 h) in comparison to passive release.

4.4.3 Transdermal metformin release through mouse skin with rGO-COOH/metformin hydrogel

The rGO-COOH/metformin heatable hydrogel is further implemented in ex vivo transdermal drug delivery studies using mice skin in Franz diffusion cells (**Figure 4.12A**). **Figure 4.12B** represents the cumulative permeation profile of metformin from rGO-COOH/metformin gels (500 µg) passively and under the impact of one-time NIR laser irradiation at 1 W cm-2 (corresponding to about 61 °C) and at 0.7 W cm-2 (corresponding to about 54 °C). After 6 h permeation, 80±8 µg cm-2 (16% of total patch as determined by HPLC, 1 W cm-2) and 56±5 µg cm-2 (12%, 0.7 W cm-2) metformin had diffused through the skin. The combined metformin delivery for a day is 319±8 µg cm-2 (64%, 1 W cm-2) and 222±10 µg cm-2 (45%, 0.7 W cm-2). The passive release after 24 h corresponds to 50±5 µg cm-2 (10%). The efficiency of thermal-induced transdermal metformin delivery of rGO-COOH/metformin gel is competitive with the hydrogel microneedles reported recently by Migdadi et al. [6], reaching a release percentage of 12.94±2.96% and 37.53±3.17% after 6 and 24 h, respectively. About 5-30 µg (5-6%) of metformin was further found to be trapped in the skin (**Figure 4.12C**), which might be possible to enter capillary afterwards.

To ensure that NIR laser irradiation did not alter the activity of metformin, G6PC mRNA in human IHH hepatocytes cells exposed to metformin photothermally heated at 45 °C, 55 °C and 65 °C, which approximately correspond to 0.5, 0.7 and 1.0 W cm^{-2}, was measured. Downregulation of the G6PC expression in hepatocytes, leading to diminished

gluconeogenesis, partly accounts for the improved insulin sensitivity and the antidiabetic effect of metformin. As previously observed, exposure of IHH cells to native metformin results in drastic reduction of the G6PC expression (**Figure 4.12D**). The effect of metformin heated at 45 °C, 55 °C and 65 °C on the decrease of G6PC mRNA level was comparable to that of caused by native metformin (**Figure 4.12D**), indicating that the laser irradiation enabling the transdermal metformin delivery does not affect the drug activity.

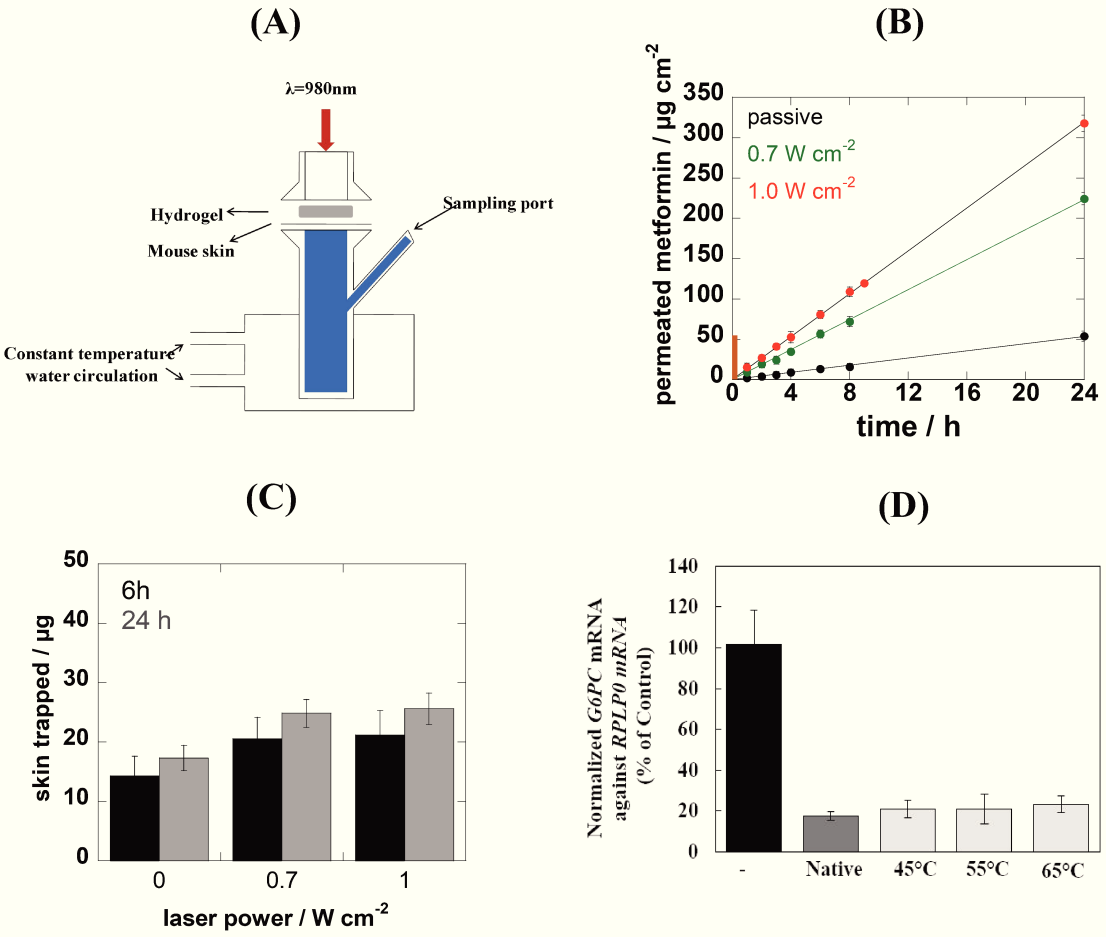

Figure 4.12: *Ex vivo* permeation profiles of metformin assessed using Franz diffusion cells. (A) Experimental *ex-vivo* set up; (B) rGO-COOH/metformin gel of 500 µg metformin activated one time for 10 min at 0.7 W cm^{-2} (green) or 1.0 W cm^{-2} (red) as well as without activation (black); (C) amount of metformin trapped in the skin; (D) The Glucose 6 Phosphatase Catalytic (G6PC) mRNA level of human IHH hepatocyte cells exposed to heated (45, 55 and 65 °C) and native metformin for 24 h. The G6PC mRNA was normalized against the RPLP0 mRNA. Similar result was found upon normalization against TBP mRNA. The expression levels from untreated cells (-, Control) were set to 100%. Data are the mean value of three independent experiments made in triplicates.

The thermal damage to the skin tissue was further evaluated. When skin is exposed to temperatures above the physiological temperature over an extended period of time, skin tissue damage can occur [42]. We have recently demonstrated that heating rGO loaded hydrogels in

contact with a skin at a laser power density of up to 5 W cm^{-2} did not induce any significant histological changes to the skin [29]. **Figure 4.13** shows the histological analysis of the skin in contact with rGO-COOH/metformin gel before and after laser irradiation (10 min, 0.7-2.0 W cm^{-2}) using conventional haemotoxylin and eosin (H&E) staining. At a laser power density up to 1.0 W cm^{-2} normal dermis characteristics are observed. The epidermis as well as the dermis are unaffected. These results are in agreement with reports by others using Cu_7S_4 loaded microneedles, where tissue necrosis in the dermis could be visualized after NIR irradiation for 3 min and 1 min, respectively [13]. Application of higher (> 1 W cm^{-2}) laser power results however in skin damage.

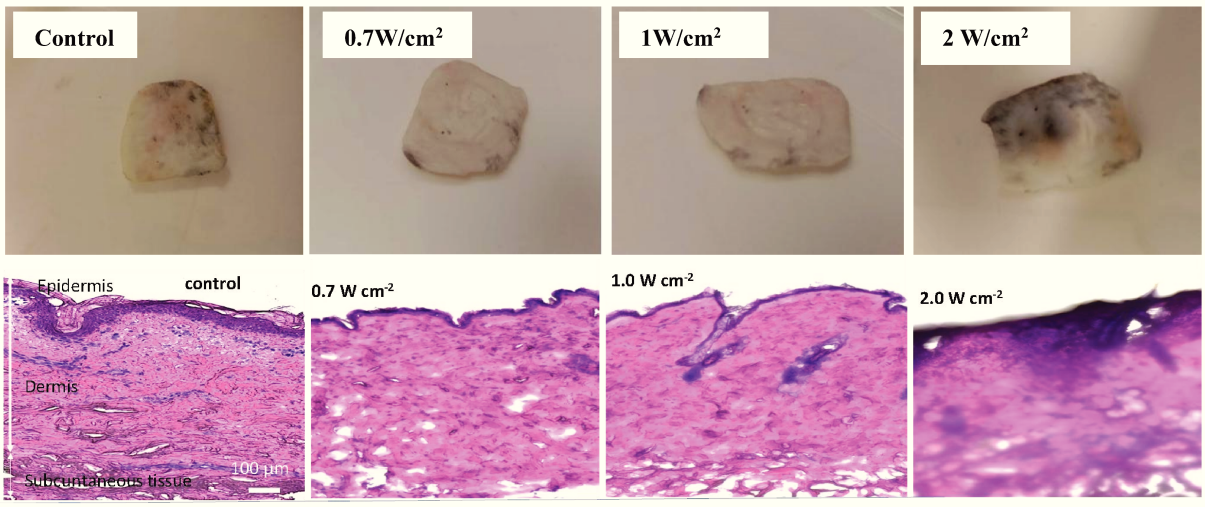

Figure 4.13: Bright-field micrograph of histological section of mice skin after H&E staining: The skin sample with no-treatment is chosen as control.

4.5 Conclusion and perspective

In summary, one pot synthesized graphene based hydrogels are presented in this chapter for heat enhanced transdermal delivery of metformin. Specifically, graphene oxide (GO) and carboxylic acid enriched reduced graphene oxide (rGO-COOH) were used as crosslinkers to instantly form hydrogels with metformin through hydrogen bonding interactions and electrostatic interactions. These weak interactions can be readily broken via change of pH and heating with laser, offering promising properties for enhanced transdermal drug delivery. GO/metformin hydrogel can be formed in mild conditions by simply mixing GO and metformin in a ratio of 10/1. However, the suboptimal heating property in NIR region with GO/metformin limits its application for photothermal enhanced transdermal delivery. The partial restoration of carbon grid on rGO-COOH offers better NIR light absorbance, while the

abundant carboxylic acid groups provide great chances for crosslinking. *Ex vivo* test on mouse skin showed that an accumulative release of 319±8 μg cm^{-2} was realized after 24 h using rGO-COOH/metformin hydrogel triggered at 1 W cm^{-2}, showing encouraging potential for heat enhanced transdermal delivery. *In vitro* assessment of the key target Glucose-6 Phosphatase (G6P) gene expression using Human hepatocyte model confirmed that metformin activity was unaffected by photothermal activation up to a heating temperature of 65 ℃. Histological tests showed that the skin stayed unharmed up to a laser power density of 1 W cm^{-2}.

4.6 Reference

[1] World Health Organization (WHO). Global report on diabetes. 2016: World Health Organization.

[2] Schwartz, SS.; Katz, A. Sodium-glucose cotransporter-2 inhibitor combination therapy to optimize glycemic control and tolerability in patients with type 2 diabetes: focus on dapagliflozin-metformin. 2016. 15;9: p.71-82.

[3] Graham, G.G.; Punt J.; Arora, M.; Day, R.O.; Doogue, M.P.; Duong, J.K.; Furlong, T.J.; Greenfield, J.R.; Greenup, L.C.; Kirkpatrick, C.M.; Ray, J.E.; Timmins, P.; Williams, K.M. Clinical pharmacokinetics of metformin. Clin Pharmacokinet 2011. 50(2): p. 81-98.

[4] Yu, W.; Jiang, G.; Zhang, Y.; Liu, D.; Xu, B.; Zhou, J. Near-Infrared Light-Triggered and Separable Microneedles for On-Demand Transdermal Delivery of Metformin On Diabetic Rats. Journal of materials chemistry B 2017. 5: p. 9507-9513.

[5] Lee, H.; Choi, T.K.; Lee, Y.B.; Cho, H.R.; Ghaffari, R.; Wang, L.; Choi, H.J.; Chung, T.D.; Lu, N.; Hyeon, T.; Choi, S.H.; Kim, D.H. A graphene-based electrochemical device with thermoresponsive microneedles for diabetes monitoring and therapy. Nature Nanotechnology 2016. 11(6): p. 566-572.

[6] Migdadi, E.M.; Courtenay, A.J.; Tekko, I.A.; McCrudden, M.T.C.; Kearney, M.C.; McAlister, E.; McCarthy, H.O.; Donnelly, R.F. Hydrogel-forming microneedles enhance transdermal delivery of metformin hydrochloride. Journal of Controlled Release 2018. 285: p. 142-151.

[7] Yu, X.; Jin, Y.; Du, L.; Sun, M.; Wang, J.; Li, Q.; Zhang, X.; Gao, Z.; Ding, P. Transdermal Cubic Phases of Metformin Hydrochloride: In Silico and in Vitro Studies of Delivery Mechanisms. Molecular Pharmaceutics 2018. 15(8): p. 3121-3132.

[8] Kopecek, J.; Yang, J. Peptide-directed self-assembly of hydrogels. Acta Biomaterialia 2009. 5(3): p. 805-816.

[9] Vashist, A.; Vashist, A.; Guptac, Y.K.; Ahmad, S. Recent advances in hydrogel based drug delivery. Journal of materials Chemistry B 2014. 2: p. 147-166.

[10] Mellati, A.; Dai, S.; Bi, J.; Jin, B.; Zhang, H. A biodegradable thermosensitive hydrogel with tuneable properties for mimicking three-dimensional micro-environments of stem cells. RSC Advances 2014. 4: p. 63951–63961.

[11] Yong Qiu; Park, K. Environment-sensitive hydrogels for drug delivery. Advanced Drug Delivery Reviews 2001. 53: p. 321-339.

[12] Yetisen, A.K.; Naydenova, I.; da Cruz Vasconcellos, F.; Blyth, J.; Lowe, C.R. Holographic sensors: three-dimensional analyte-sensitive nanostructures and their

applications. Chemical Reviews 2014. 114(20): p. 10654-10696.

[13] Zhang, Y.; Wang, D.; Gao, M.; Xu, B.; Zhu, J.; Yu, W.; Liu, D.; Jiang, G. Separable Microneedles for Near-Infrared Light-Triggered Transdermal Delivery of Metformin in Diabetic Rats. ACS Biomaterials Science & Engineering 2018. 4(8): p. 2879-2888.

[14] Zhang, Y.; Jiang, G.; Hong, W.; Gao, M.; Xu, B.; Zhu, J.; Song, G.; Liu, T. Polymeric Microneedles Integrated with Metformin-Loaded and PDA/LA-Coated Hollow Mesoporous SiO2 for NIR-Triggered Transdermal Delivery on Diabetic Rats. ACS Applied Bio Materials 2018. 1(6): p. 1906-1917.

[15] Liu, D.; Zhang, Y.; Jiang, G.; Yu, W.; Xu, B.; Zhu, J. Fabrication of Dissolving Microneedles with Thermal-Responsive Coating for NIR-Triggered Transdermal Delivery of Metformin on Diabetic Rats. ACS Biomaterials Science & Engineering 2018. 4: p. 1687-1695.

[16] Lee, H.; Song, C.; Hong, Y.S.; Kim, M.S.; Cho, H.R.; Kang, T.; Shin, K.; Choi, S.H.; Hyeon, T.; Kim, D.H. Wearable/disposable sweat-based glucose monitoring device with multistage transdermal drug delivery module. Science Advances 2017. 3(3): p. 1-8.

[17] Yu, W.; Jiang, G.; Zhang, Y.; Liu, D.; Xu, B.; Zhou, J. Near-infrared light triggered and separable microneedles for transdermal delivery of metformin in diabetic rats. Journal of Materials Chemistry B 2017. 5(48): p. 9507-9513.

[18] Fichman, G.; Gazit, E. Self-assembly of short peptides to form hydrogels: design of building blocks, physical properties and technological applications. Acta Biomaterialia 2014. 10(4): p. 1671-1682.

[19] Vermonden, T.; Censi, R.; Hennink, W.E. Hydrogels for protein delivery. Chemical Reviews 2012. 112(5): p. 2853-2888.

[20] Guvendiren, M.; Lu, H.D.; Burdick, J.A. Shear-thinning hydrogels for biomedical applications. Soft Matter 2012. 8(2): p. 260-272.

[21] Sathaye, S.; Mbi, A.; Sonmez, C.; Chen, Y.; Blair, D.L.; Schneider, J.P.; Pochan, D.J. Rheology of peptide- and protein-based physical hydrogels: are everyday measurements just scratching the surface? Wiley Interdiscip Rev Nanomed Nanobiotechnol 2015. 7(1): p. 34-68.

[22] Neufeld, L.; Bianco-Peled, H. Pectin-chitosan physical hydrogels as potential drug delivery vehicles. International Journal of Biological Macromolecules 2017. 101: p. 852-861.

[23] Liu, J.; Cui, L.; Losic, D. Graphene and graphene oxide as new nanocarriers for drug delivery applications. Acta Biomaterialia 2013. 9(12): p. 9243-9257.

[24] Bai, H.; Li, C.; Wang, X.; Shi, G. A pH-sensitive graphene oxide composite hydrogel. Chemical Communications 2010. 46(14): p. 2376-2378.

[25] Wu, J.; Chen, A.; Qin, M.; Huang, R.; Zhang, G.; Xue, B.; Wei, J.; Li, Y.; Cao, Y.; Wang, W. Hierarchical construction of a mechanically stable peptide-graphene oxide hybrid hydrogel for drug delivery and pulsatile triggered release in vivo. Nanoscale 2015. 7(5): p. 1655-1660.

[26] Tao, C.-a.; Wang, J.; Qin, S.; Lv, Y.; Long, Y.; Zhu, H.; Jiang, Z. Fabrication of pH-sensitive graphene oxide–drug supramolecular hydrogels as controlled release systems. Journal of Materials Chemistry 2012. 22(47): p. 24856-24861.

[27] Abderrahmani, A.; Yengo, L.; Caiazzo, R.; Canouil, M.; Cauchi, S.; Raverdy, V.; Plaisance, V.; Pawlowski, V.; Lobbens, S.; Maillet, J.; Rolland, L.; Boutry, R.; Queniat, G.; Kwapich, G.; Tenenbaum, M.; Bricambert, J.; Saussenthaler, S.; Anthony, E.; Jha,

P.;Derop, J.; Sand, O.; Rabearivelo, I.; Leloire, A.; Pigeyre, M.; Daujat-Chavanieu, M.; Gerbal-Chaloin, S.; Dayeh, T.; Lassailly, G.; Mathurin, P.; Staels, B.; Auwerx, J.; Schürmann, A.; Postic, C.; Schafmayer, C.; Hampe, J.; Bonnefond, A.; Pattou F.; and P. Froguel, Increased Hepatic PDGF-AA Signaling Mediates Liver Insulin Resistance in Obesity-Associated Type 2 Diabetes. Diabetes. 2018. 67: p. 1310-1321.

[28] Madsen, A.; Bozickovic, O.; Bjune, J. I.; Mellgren G. and J. V. Sagen, Metformin inhibits hepatocellular glucose, lipid and cholesterol biosynthetic pathways by transcriptionally suppressing steroid receptor coactivator 2 (SRC-2). Scientific Reports. 2015. 5: 16430.

[29] Teodorescu, F.; Queniat, G.; Foulon, C.; Lecoeur, M.; Barras, A.; Boulahneche, S.; Medjram, M.S.; Hubert, T.; Abderrahmani, A.; Boukherroub, R.; Szunerits, S. Transdermal skin patch based on reduced graphene oxide: A new approach for photothermal triggered permeation of ondansetron across porcine skin. Journal of Controlled Release. 2017. 245: p. 137-146.

[30] Son, D.; Lee, J.; Qiao, S.; Ghaffari, R.; Kim, J.; Lee, J.E.; Song, C.; Kim, S.J.; Lee, D.J.; Jun, S.W.; Yang, S.; Park, M.; Shin, J.; Do, K.; Lee, M.; Kang, K.; Hwang, C.S.; Lu, N.; Hyeon, T.; Kim, D.-H. Multifunctional wearable devices for diagnosis and therapy of movement disorders. Nature Nanotechnology. 2014. 9(5): p. 397-404.

[31] Weiss, R.; Hessenberger, M.; Kitzmuller, S.; Bach, D.; Weinberger, E.E.; Krautgartner, W.D.; Hauser-Kronberger, C.; Malissen, B.; Boehler, C.; Kalia, Y.N.; Thalhamer, J.; Scheiblhofer, S. Transcutaneous vaccination via laser microporation. Journal of Controlled Release. 2012. 162(2): p. 391-399.

[32] Lee, J.W.; Gadiraju, P.; Park, J.H.; Allen, M.G.; Prausnitz, M.R. Microsecond thermal ablation of skin for transdermal drug delivery. Journal of Controlled Release. 2011. 154(1): p. 58-68.

[33] Lai, Q.; Zhu, S.; Luo, X.; Zou, M.; Huang, S. Ultraviolet-visible spectroscopy of graphene oxides. AIP Advances. 2012. 2: p. 1-5.

[34] Ali, S.M.; Yosipovitch, G. Skin pH: from basic science to basic skin care. Acta Derm Venereol. 2013. 93(3): p. 261-267.

[35] Robinson, J.T.; Tabakman, S.M.; Liang, Y.; Wang, H.; Casalongue, H.S.; Vinh, D.; Dai, H. Ultrasmall reduced graphene oxide with high near-infrared absorbance for photothermal therapy. The Journal of American Chemical Society. 2011. 133(17): p. 6825-6831.

[36] Yang, K.; Wan, J.; Zhang, S.; Tian, B.; Zhang, Y.; Liu, Z. The influence of surface chemistry and size of nanoscale graphene oxide on photothermal therapy of cancer using ultra-low laser power. Biomaterials. 2012. 33(7): p. 2206-2214.

[37] Hu, S.H.; Chen, Y.W.; Hung, W.T.; Chen, I.W.; Chen, S.Y. Quantum-dot-tagged reduced graphene oxide nanocomposites for bright fluorescence bioimaging and photothermal therapy monitored in situ. Advanced Materials. 2012. 24(13): p. 1748-1754.

[38] Matteini, P.; Tatini, F.; Cavigli, L.; Ottaviano, S.; Ghini, G.; Pini, R. Graphene as a photothermal switch for controlled drug release. Nanoscale. 2014. 6(14): p. 7947-7953.

[39] Kim, H.; Kim, W.J. Photothermally controlled gene delivery by reduced graphene oxide-polyethylenimine nanocomposite. Small. 2014. 10(1): p. 117-126.

[40] Chen, J.; Liu, H.; Zhao, C.; Qin, G.; Xi, G.; Li, T.; Wang, X.; Chen, T. One-step reduction and PEGylation of graphene oxide for photothermally controlled drug delivery. Biomaterials. 2014. 35(18): p. 4986-4995.

[41] Turcheniuk, K.; Hage, C.-H.; Spadavecchia, J.; Serrano, A.Y.; Larroulet, I.; Pesquera, A.; Zurutuza, A.; Pisfil, M.G.; Héliot, L.; Boukaert, J.; Boukherroub, R.; Szunerits, S. Plasmonic photothermal destruction of uropathogenic E. coli with reduced graphene oxide and core/shell nanocomposites of gold nanorods/reduced graphene oxide. Journal of Materials Chemistry B. 2015. 3(3): p. 375-386.

[42] Im, I.-T.; Youn, S.B.; Kim, K. Numerical Study on the Temperature Profiles and Degree of Burns in Human Skin Tissue During Combined Thermal Therapy. Numerical Heat Transfer, Part A: Applications. 2015. 67(9): p. 921-933.

CHAPTER 5 CONCLUSIONS AND PERSPECTIVES

Despite the great progress that has been achieved in the past decade, nanotechnology-based medical applications are yet to be fully implemented. The scope of this thesis was the development of heat-based nanomaterials, notably graphene related matrixes, applied for the photothermal ablation of pathogens as well as for heat improved transdermal drug delivery. More precisely, NIR laser-driven photothermal based treatment of skin infection, rapid and complete killing of bacteria using magnetic graphene based matrixes for isolated and enhanced transdermal delivery of metformin were dicussed.

A promising gold nanohole array patterned on flexible a polymer interface, Kapton, using colloidal lithography with a plasmonic extinction band at 950 nm was successfully implemented to heat solutions to 60 ˚C in 10 min. The light-heat transfer could be further improved by post-coating of reduced graphene oxideonto the patch where temperature of about 76 °C could be reached. This patch allowed a complete ablation of both Gram-positive and Gram-negative pathogens in only 10 min. Application for the local treatment of mice with infected skin wounds showed that wound healing was observed upon placing the photothermal patch over the wound and irradiating for 10 min. It is worth noting that the patch is stable for several time usages, making the approach rather appealing as antibiotic free alternative to treat local infections

Magentic graphene based nanosheets proved also to be of high efficient for the magnetic isolation of pathogens from solution. Taking advantage of the magnetic property as well as the arge surface area of rGO, a capture efficiency of 99.9% was achieved for both Gram-positive and Gram-negative pathogens within 30 min even at concentrations as low as of 1×10^1 cfu/mL. The outstanding photothermal property of rGO enables furthermore a complete NIR driven ablation of the captured bacteria. Further intergration of anti-fimbrial *E.coli* antibodies to the nanocomposites offers the capability of selective isolation of *E. coli* UTI89, the pathogen related to urine tract infections. The proposed approach is expected to help rapid cleaning of bodily fluids in a fast and selective manner.

It is hoped that this work opens up novel perspectives in the treatment of infections when cannot be easily eradicated with antibiotics. More work remains to be done in exploring other kinds of nanomaterials and broadening the scope of applications in this timely area. The

focuses may be on the treatment of biofilms, compacted bacterial cells that stick to each other or to a surface, which are still difficult to eradicate and responsible for an estimate 80% of all infections in the world. As the bacteria colonies are generally covered with extracellular polymeric substances, antibiotic treatment remains difficult to implement. Application of nanomaterials are expected to penetrate the thick layer of biofilm and heat can eradicate bacterial cells without causing antibiotic-resistance stress.

Moreover, graphene oxide (GO)/metformin and carboxylic acid enriched reduced graphene oxide (rGO-COOH)/metformin hydrogels could be implemented for heat based transdermal delivery of metformin. The hydrogels were synthesized through a simple mixture of graphene based materials and metformin at a ratio of 10/1. The abundant functional groups on graphene sheets can instantly form physical bonding to metformin and thus become crosslinked hydrogels. GO/metformin gels showed limited heating ability, while rGO-COOH/metformin hydrogels displayed not only enhanced NIR absorption but a heat and pH responsive release. An accumulative transdermal release of 319±8 μg cm^{-2} was found after 24 h under 980 nm laser irradiation at 1W cm^{-2}. *In vitro* assessment of the key target Glucose-6 Phosphatase (G6P) gene expression using Human hepatocyte model confirmed that metformin activity was unaffected by photothermal activation. Histological examination showed that heating with laser up to 1 W cm^{-2} for 10min did not cause any damage to the skin. This approach might be also a way to deliver macromolecular drugs such as proteins, a remaining challenge in this field. Heatable hydrogel microneedles might be a further interesting perspective for the on-demand delivery of drugs transdermally in larger quantities. The future of nanomaterials and in particular 2D nanomaterials such as graphene seems bright.

APPENDIX

EXPERIMENTAL PART

6.1 Materials

All chemicals were reagent grade or higher and were used as received unless otherwise specified. Hydrazine monohydrate, chitosan, dopamine hydrochloride, sodium nitrite ($NaNO_2$), sulfuric acid (H_2SO_4), hydrochloric acid (HCl), dichloromethane (CH_2Cl_2), iron (II) chloride tetrahydrate ($FeCl_2 \cdot 4H_2O$), iron (III) chloride hexahydrate ($FeCl_3 \cdot 6H_2O$), ammonium hydroxide (NH_4OH), *O*-(2-aminoethyl)-*O′*-(2-methylethyl)heptaethylene glycol (≥90%, NH_2-PEG_8-N_3), dichloromethane (≥99.8%, CH_2Cl_2), *N,N′*-disuccinimidyl carbonate (≥95.0%, DSC), 1-Ethyl-3-(3-dimethylaminopropyl)carbodiimide (EDC), *N*-Hydroxysuccinimide (NHS), 1-pyrenecarboxylic acid (97%, Pyr-COOH) and triethylamine (≥99.5%, TEA) Metformin hydrochloride, sodium hydroxide (NaOH) and chloroacetic acid (Cl-CH_2-COOH), Luria−Bertani (LB), Man-Rogosa-Sharpe (MRS) and brain heart infusion (BHI) broth and agar were obtained from Sigma-Aldrich. Kapton® HN polyimide foils (thickness of 75 μm and 125 μm) were obtained from DuPont (Circleville, OH, USA). Graphene oxide (GO) was purchased from Graphitene (UK). live/dead BacLight bacterial viability staining kit was purchased from Invitrogen. Hematoxylin and Eosin (H&E) staining kit was bought from vector labs.

Serum samples were kindly provided by the CHU, Lille. Anti-fimbrial antibodies were obtained by immunizing serum from rats with purified fimbriae, which were delipidated and purified on an HiFliQ ProteinA affinity chromatography column (CliniSciences) and eluted at 1 mg mL^{-1} concentration in sodium citrate buffer at pH 5.6.

6.2 Instrumentation

6.2.1 Nuclear magnetic resonance (NMR)

NMR spectra were recorded with a Bruker Advance 300 MHz spectrometer using deuterated chloroform as the lock and TMS as an internal standard.

6.2.2 Thin layer chromatography (TLC) and Column chromatography

TLC was carried out using precoated aluminium backed silica TLC plates (Alugrams SIL G/UV254, Macherey-Nagel) which were visualized using ultraviolet light. Column chromatography was performed on Sigma-Aldrich silica gel 60 (pore size 60 Å, 230–400 mesh particle size) without applied pressure.

6.2.3 Reversed phase–high performance liquid chromatography (RP-HPLC)

RP-HPLC analyses were realized on a Shimadzu LC2010-HT (Shimadzu, Tokyo, Japan). C4 and C18 columns were used for analyses. In the case of C4 column, a 5 mm C4 QS Uptispheres 300 Å, 250 ×4.6 mm column (Interchim, Montluçon, France) was used as the analytical column. The column was heated to 40 ˚C. The mobile phase was a mixture of eluent A (trifluoroacetic acid 0.05% in H_2O) and eluent B (trifluoroacetic acid 0.05% in CH3CN) at a flow rate of 1 mL min-1. The linear gradient was 0 to 80% of eluent B in 30 min and the detection was performed at 215 and 254 nm after the injection of 40 µL into the column. For C18 column, The mobile phase is consisted of acetonitrile-potassium dihydrogen phosphatebuffer pH 6.5 (34:66, v/v) and 3 mM SDS and was run at a flow rate of 0.3 mL min^{-1}. The reverse phase column was a 2.6 µm C18, 150×4.6 mm column (Interchim, Montluçon, France). The column was maintained at room temperature. The sample solution was injected at a volumn of 10µL and the detection wavelength was set at 230 nm.

6.2.4 High resolution transmission electron microscopy (HR-TEM)

TEM analysis of the prepared samples was carried out by using an FEI, TECNAI G2 F20 instrument operated at an accelerated voltage of 300 kV (Cs = 0.6 mm, resolution 1.7 Å). For the TEM analysis, the sample was prepared by drop casting 10 mL of the dispersed solution of 1 mg of material in 5 mL of isopropyl alcohol over a carbon coated 200 mesh Cu grid. The catalyst drop cast Cu grid was dried and the prepared sample was used for imaging purposes.

6.2.5 UV-Vis spectra

Absorption spectra were recorded using a Perkin Elmer Lambda UV-Vis 950 spectrophotometer in a 1 cm quartz cuvette. The wavelength range was 200–1200 nm.

6.2.6 Fourier transform infrared (FTIR) spectra

FTIR spectra were recorded using a Thermo Scientific FTIR instrument (Nicolet 8700) at a

resolution of 4 cm^{-1}. Dried samples (1 mg) were mixed with KBr powder (100 mg) in an agate mortar. The mixture was pressed into a pellet under 10 tons load for 2–4 min, and the spectrum was recorded immediately. Sixteen accumulative scans were collected. The signal from a pure KBr pellet was subtracted as the background.

6.2.7 Zeta-potential measurements

Zeta-potential measurements were performed using a zeta-sizer nano-ZS (Malvern Instruments Inc. Worcestershire, UK). The samples were diluted to 10 mg mL-1 and measured in Milli-Q water at different pH values.

6.2.8 N_2 adsorption–desorption

N_2 adsorption–desorption data were obtained using a Quantachrom SI Micromeritics apparatus, and the isotherms were evaluated with the Barrett–Joyner–Halenda method to determine the surface area, pore size and distribution.

6.2.9 Saturation magnetization curves

Magnetic properties were determined using an MPMS-XL SQUID magnetometer. The magnetization loops M(H) were measured at 300 K by sweeping the applied magnetic field between 20 kOe and -20 kOe. Thermal variation of magnetization was measured using the zero-field-cooled (ZFC) procedure, for which the sample is first cooled down to 5 K in the absence of an applied magnetic field, and then magnetization is measured during the warming of the sample up to 400 K, with an applied magnetic field of 80 Oe.

6.2.10 Raman spectroscopy

Micro-Raman spectroscopy measurements were performed on a LabRam HR Micro-Raman system (Horiba Jobin Yvon, France) combined with a 473 nm laser diode as excitation source. Visible light is focused by a 100× objective. The scattered light is collected by the same objective in backscattering configuration, dispersed by a 1800 mm focal length monochromator and detected by a CCD camera.

6.2.11 Scanning electron microscopy (SEM)

Images were obtained using an electron microscope ULTRA 55 (Zeiss) equipped with a thermal field emission emitter and three different detectors (Energy-Selective Backscattered

Detector with filter grid, high efficiency In-lens Secondary Electron Detector, and Everhart-Thornley Secondary Electron Detector).

6.2.12 X-ray photoelectron spectroscopy (XPS)

XPS experiments were performed in a PHl 5000 Versa Probe-Scanning ESCA Microprobe (ULVAC-PHI, Japan/USA) instrument at a base pressure below 5×10^{-9} mbar. Core -level spectra were acquired at pass energy of 23.5 eV with a 0.1 eV energy step. All spectra were acquired with 90° between X-ray source and analyzer and with the use of low energy electrons and low energy argon ions for charge neutralization. After subtraction of the Shirley-type background, the core-level spectra were decomposed into their components with mixed Gaussian-Lorentzian (30:70) shape lines using the Casa XPS software. Quantification calculations were conducted using sensitivity factors supplied by PHI.

6.2.13 Measurement of the Photothermal Effect

A 980 nm continuous wave laser (Gbox model, Fournier Medical Solution) was used for the photothermal experiments. This laser was injected into a 400 μm core fiber and placed around 6 cm away from the bottom of the wells. The output was not collimated and the resulting beam divergence allowed us to illuminate uniformly the wells. The temperature changes were captured by an infrared camera (Thermovision A40) and treated using ThermaCam Researcher Pro 2.9 software.

6.3 Synthesis of materials

6.3.1 Fabrication of Gold Nanoholes Modified Kapton (K/Au NHs)

Kapton HN polyimide foils (10 × 10 mm^2, thickness 125 μm) were cleaned with acetone in an ultrasonic water bath for 30 min, followed with isopropanol for 10 min and then dried under a nitrogen flow. The cleaned Kapton foils were modified with gold nanoholes (K/Au NHs) according to recent publications [1-3]. A monolayer of 980 nm polystyrene beads (Microparticles GmbH) was first deposited on the surface of Kapton by self-assembly. To reduce the size of the particles and isolate them, SF_6 and oxygen plasma etching for 11 min was employed (5 mTorr). The samples were coated with 2 nm Ti followed by 40 nm Au at a constant deposition rate of 1 Å s^{-1} using physical vapor deposition. The beads on top of the

Kapton were removed by dissolution in chloroform (overnight). The arrays display holes of an average size of 630 nm and center-to-center spacing of 980 nm.

6.3.2 Preparation of Graphene-Coated K/Au NHs (K/Au NHs-Graphene)

Graphene formed on polycrystalline Cu foils was transferred onto K/Au NHs using a modified wet chemical transfer process as reported in the literature [4]. Poly(methyl methacrylate) (PMMA, 5%) was spin-coated onto the graphene-coated Cu foil and baked at 170 °C for 10 min. The Cu foil was dissolved using a solution of $HCl/H_2O_2/H_2O$ (1/1/40) and the formed graphene/PMMA rinsed with deionized water 5−6 times to remove any ion contamination. Graphene was then mechanically transferred onto K/Au NHs, followed by a slow backing step at 90 °C to remove trapped water and to increase the contact between graphene and K/Au NHs. Finally, the PMMA layer was removed by dipping the sample in acetone for 30 min, rinsed with methanol, and dried by a mild nitrogen blow.

6.3.3 Preparation of rGO-Coated K/Au NHs (K/Au NHs-rGO)

rGO was formed by adding hydrazine hydrate (100 μL, 6.4 mM) to 100 mL of GO aqueous suspension (3 mg mL^{-1}) in a round-bottom flask and heated in an oil bath at 80 °C for 24 h. During this time, the reduced GO gradually precipitates out of the solution. The product was isolated by filtration over a polyvinylidene difluoride (PVDF) membrane with a 0.45 μm pore size, washed copiously with water (5×20 mL) and methanol (5×20 mL), and dried in an oven at 60 °C for 6 h. An aqueous suspension of rGO (1 mg mL^{-1}, 25 μL) was dropcasted three times onto K/Au NHs and allowed to dry overnight at 70 °C.

6.3.4 Synthesis of 2-nitrodopamine

2-Nitrodopamine was synthesized according to previous studies [5]. Dopamine hydrochloride (1.90 g, 10 mmol) and sodium nitrite (1.52 g, 22 mmol) were dissolved in water (25 mL) and cooled to 0 °C. Sulfuric acid (17.4 mmol in 10 mL of water) was added slowly to the mixture, and a yellow precipitate was formed. After stirring at room temperature overnight, the precipitate was filtered and recrystallized from water to give the product as a hemisulfate salt. Yield 1.9 g (77%). 1H NMR (DMSO-d_6, 300 MHz, ppm): 3.10 (br s, 4H, CH_2CH_2), 6.85 (s, 1H), 7.47 (s, 1H).

6.3.5 Synthesis of N-(26-azido-3,6,9,12,15,18,21,24-octaoxahexacosyl)-pyrene-1-carboxamide (pyrene-PEG)

Pyrene-PEG was synthesized as reported earlier by our group [6]. Briefly, 1-pyrenecarboxylic acid (100 mg, 0.41 mmol) and DSC (125 mg, 0.49 mmol) were dissolved in anhydrous CH_2Cl_2 (15 mL). To this solution, TEA (68 mL, 0.49 mmol) and NH2-PEG8-N3 (214 mg, 0.49 mmol) dissolved in CH_2Cl_2 (2 mL) were slowly added under stirring. The resulting mixture was kept under stirring overnight at room temperature. Then the solvent was evaporated under vacuum. The crude product was dissolved in CH_2Cl_2 (6 mL), washed with 5% HCl aqueous solution (5 mL, twice) and H_2O (5 mL, twice), and dried over $MgSO_4$. The residue was purified by silica gel column chromatography using CH_2Cl_2 and the product was isolated as a viscous pale yellow oil; yield = 135 mg, 50%; 1H NMR (300 MHz, $CDCl_3$) d 8.63 (d, 1H, J = 9 Hz, py), 8.3–8.0 (m, 8H, py), 7.06 (bt, 1H, J = 4.3 Hz, –NH–), 3.9–3.3 (m, 36H, PEG); 13C NMR (75 MHz, $CDCl_3$) d 128.6, 127.2, 126.3, 125.8, 125.7, 124.9, 124.7, 124.5, 124.4, 70.8–69.6, 50.7, 40.1; FT-IR: 717, 763, 820, 852, 948, 1039, 1104, 1181, 1248, 1289, 1328, 1348, 1455, 1532, 1602, 1648, 2104, 2867 cm^{-1}.

6.3.6 Preparation of 2-nitrodopamine modified magnetic particles (MP_{ND})

Magnetic particles (MP) were prepared as reported previously [7]. $FeCl_2 \cdot 4H_2O$ (0.34 g, 1.7 mmol) and $FeCl_3 \cdot 6H2O$ (0.95 g, 3.5 mmol) were dissolved in MQ water (20 mL) and subsequently added to a nitrogen-protected three-necked flask under sonication. The resulting mixture was heated at 50 ˚C for 30 min. Then concentrated ammonium hydroxide (2 mL) was added dropwise and kept at 50 ˚C for 30 min. The system was finally cooled to room temperature and the solid product was isolated via a non-uniform magnetic field generated by a Nd–Fe–B permanent magnet. The resulting Fe_3O_4 particles (MPs) were washed six times with Milli-Q water to remove unreacted chemicals and then stored in water. A water dispersion of bare MPs (10 mg mL^{-1}, 1 mL) was mixed with 2-nitrodopamine (20 mg) and sonicated for 1 h at room temperature. The formed magnetic particles (MP_{ND}) were isolated by means of a magnet and purified through six consecutive wash/precipitation cycles with water to ensure complete removal of unreacted dopamine. The precipitate was dried in an oven at 50 ˚C.

6.3.7 Integration of MP_{ND} onto reduced graphene oxide (rGO)

To a solution of rGO (0.5 mg mL^{-1}) was added an aqueous solution of MP_{ND} (0.5 mg mL^{-1}) corresponding to a ratio of 1/1 and sonicated for 90 min. The formed rGO/MP_{ND} nanostructures were isolated by means of a magnet and purified through six consecutive wash/precipitation cycles with water. The precipitate was dried in an oven at 50 ˚C.

6.3.8 Functionalization of rGO/MP_{ND} with pyrene-PEG

The rGO/MP_{ND} nanostructures (500 mg mL^{-1}) were mixed with pyrene-PEG solution (5 mM) and the suspensions were stirred for 1 h at room temperature. All samples were isolated by means of a magnet and purified through six consecutive wash/precipitation cycles with water.

6.3.9 Covalent linking of anti-fimbrial antibody onto pyrene-PEG rGO/MP_{ND}

Anti-fimbrial antibody immobilization onto rGO/MP_{ND} nanostructures was achieved by carbodiimide crosslinking chemistry. Briefly, the rGO/MP_{ND} nanocomposite (500 mg mL^{-1}) was mixed with a 100 times diluted antibody solution of 1 mg mL^{-1} in PBS at pH = 7.4 containing EDC·HCl (25 mM) and NHS (25 mM). The reaction was left to proceed at 4 ˚C for 2 h under agitation, followed by magnetic extraction and PBS washing to remove weakly adsorbed antibodies. The particles were stored in PBS buffer at 4 ˚C before use.

6.3.10 Quantification of amino groups by a modified Kaiser test

Primary amine groups were quantified using a modified photometric assay [8]. Briefly, the MPND particles (500 mg mL^{-1}) were dissolved in 1 mL of Milli-Q water. To this suspension was added 1 mL of the buffer solution (36 g of sodium acetate were dissolved in 6.9 mL of acetic acid and filled with Milli-Q water up to a volume of 100 mL) and then sonicated for 15 min. After that, 1 mL of KCN solution (2 mL of 0.03 M KCN solution was diluted to a volume of 100 mL with pyridine) and 1 mL of phenol solution (80 g of phenol were dissolved in 20 mL of ethanol) were added and the suspension was heated at 120 ˚C for 10 min; 1 mL of ninhydrin solution (5 g of ninhydrin was dissolved in 100 mL of ethanol) was added and heated for another 10 min. After the solution was cooled to room temperature, 5 mL of ethanol was added (60%) and the absorbance was recorded at 570 nm.

6.3.11 Formation of carboxylic acid enriched rGO (rGO-COOH)

Carboxylic acid enriched GO (GO-COOH) was synthesized from GO as described by Sun *et al* [9] In short, sodium hydroxide (NaOH, 1.4 g) and chloroacetic acid (Cl-CH_2-COOH, 1 g) were added to 50 mL of GO (20 mg) aqueous solution and sonicated at 35 kHz for 2 h at 80 °C to convert hydroxyl groups present on GO to COOH via conjugation of acetic acid moieties and to partially reduce GO into rGO. The resulting rGO-COOH solution was quenched with HCl (20 %), washed (four times) with distilled water until neutral pH and purified by repeated rinsing/centrifugation (4500 rpm, 30 min) cycles.

6.3.12 Fabrication of metformin hydrogel

The metformin gel was fabricated by mixing graphene oxide (10 mg mL^{-1}) or rGO-COOH (10 mg mL^{-1}) and metformin hydrochloride (10 mg mL^{-1}) at a ratio of 10:1 (v/v), then the formed gel was homogenized by sonicating for 5 min prior to lyophilization for 12 hours before use.

6.4 In vitro experiments

6.4.1 Bacterial Growth Conditions

The Gram-negative *β*-lactamase-producing LF82 (an adherent-invasive *E. coli*) were grown at 37 °C with shaking in Luria−Bertani (LB) broth overnight. Upon 100-fold dilution, incubation was prolonged until the OD_{600} had reached 0.3−0.5. The probiotic *Enterococcus faecalis* DD14, a Gram positive commensal recently isolated from the meconium of newborn children at the Central Hospital of Roubaix, France, was grown without shaking overnight at 37 °C, in Man-Rogosa-Sharpe (MRS) medium. *S. epidermidis*, a clinical strain obtained from the Central Hospital of Roubaix, France, was grown in a brain heart infusion (BHI) medium at 37 °C overnight without agitation. *E. coli* UTI89 wild-type strain, UTI 89 Δfim (without fim operon) and *S. aureus* cultures were grown on an LB agar plate upon inoculation overnight in Luria–Bertani (LB) broth at 37 ˚C with moderate shaking (200 rpm). Upon 50-fold dilution, incubation was prolonged until the OD_{600} had reached 0.5 equivalent to 1×10^9 cfu mL^{-1}. The bacteria were re-suspended in PBS (10 mM) and adjusted to the required concentration.

6.4.2 Bacteria Cell Irradiation with K/Au NHs photothermal patches

An aliquot of 1 mL cultures were seeded in a sterile 24-well plate at 10^9 cfu mL^{-1}. The interfaces were immersed into a well of the 24-well plates and irradiated with the laser set at 980 nm illumination for different time intervals at laser powers density of 2 W cm^{-2}. After this treatment, survival of the bacteria was measured by determining the titer of viable bacteria able to grow. A tenfold dilution series of the bacterial solutions in phosphate buffer saline were spotted in 10 μL aliquots on corrresponding agar medium. Visual counting of the number of colonies upon overnight incubation at 37 °C allowed reading out the initial and final concentrations of the different strains in cfu mL^{-1}. After irradiation, the bacteria were immediately stained for cell viability assays. The total amount of live and dead bacteria cells was determined using the Live/Dead BacLight bacterial viability staining kit (Invitrogen). A 1:1 mixture of SYTO 9 nucleic acid stain and propidium iodide (PI) was prepared and 3 μL was added to 1 mL bacteria suspension, mixed thoroughly, and incubated at room temperature in the dark for 15 min. Five microliters of the stained bacteria suspension was deposited between a glass slide and a coverslip. The slides were observed using a Leica AF6000 LX fluorescent microscope equipped with an Andor iXon 885 Camera and by using an oil immersion objective (100×; 1.4 NA objective). The fluorescence signal was acquired using a dual band excitation and emission filter sets for green fluorescent protein (GFP) and red fluorescent protein (mCherry).

6.4.3 Biofilm growth

The Gram-negative *E. coli* LF82 and The Gram-positive *Enterococcus faecalis* DD14 were grown at 37 °C with shaking at 160 rpm in Luria−Bertani (LB) broth and Man-Rogosa-Sharpe (MRS) medium respectively for overnight. Upon 100-fold dilution, incubation was prolonged until the OD_{600} had reached 0.3−0.5. The cultures were diluted into a bacterial concentration of 1×106 cfu mL^{-1}. Different interfaces were placed into 24-wells plate and subsequently covered with 1mL of diluted bacterial solution. The plate was incubated at 37 ˚C without shaking for 72 hours. The obtained biofilms were then washed with PBS and imaged by fluorescent microscope and SEM.

6.4.4 Photothermal in Vitro Experiment with LED array

In vitro photothermal ablation tests on parts of fresh pork meat were performed by controlling

the power of a LED array (6×6 mm^2 in size, 10 W, 940 nm) and by controlling the temperature of the meat surface with a thermal forward-looking infrared (FLIR) camera (Seek Thermal, Inc.).

6.4.5 Bacteria isolation with magnetic nanocomposites

The bacterial suspensions were diluted to the desired concentration (1×10^1 to 1×10^8 cfu mL^{-1}). Magnetic nanostructures of different concentrations (4–10 mg mL^{-1}) were dispersed via ultrasonication (5 min, ultrasonic bath Branson 5800) in PBS (5 mL, 10 mM, pH 7.4). Bacterial suspensions (5 mL) were mixed with the magnetic nanostructures (5 mL) under shaking (200 rpm, 37 ˚C). After a given time interval, an aliquot was taken periodically to measure the remaining bacterial cell concentration by UV/Vis in solution after magnetic nanostructures had been separated by applying an external magnetic field. The collection efficiency (E) was calculated according to:

$$E(\%) = \frac{(A_0 - A_t)}{A_0} \times 100\%$$

where A_0 is the initial OD_{600} and A_t the OD_{600} after cell capture.

The capacity (Q, cells per mg) was calculated according to:

$$Q(\text{cells per mg}) = \frac{(A_0 - A_t) \times [\text{E.Coli}]}{0.1 \times c}$$

where c is the concentration of the particles (mg mL^{-1}) and [*E. coli*] is the concentration of the pathogen in solution.

6.4.6 Photothermal treatment of magnetically separated pathogens

The magnetic nanostructures used for the separation of the pathogens were irradiated with a 980 nm continuous wave laser for 10 min at 1 W cm^{-2} and cell viability assessed by counting the viable bacterial colonies.

6.4.7 In vitro release of metformin

GO/metformin and rGO-COOH/metformin (containing 100 µg of metformin) gels were used for metformin release into solutions. pH dependent releases were carried out by immersed the gels into solutions with different pH, samples were collected at different time points (30

min,1,2,3,4,5,6 h). Photothermal responsive releases were performed using 980 nm laser irradiation at different power densities. To increase the heating property of GO/metformin, a rGO-kapton photothermal patch was incorporated with the gel. Quantification of metformin was realized through UV spectrometry method, the difference of the absorbance between λ=232 nm and λ=270 nm (A_{232nm}-A_{270nm}) was plotted against the corresponding metformin concentration, then the released samples were quantified after filtration and dilution.

6.4.8 Skin permeation experiments

Skin permeation studies were performed using fresh mice skin. For this, mice C57BL/6 were anaesthetized with isoflurane, shaved with an electric shaver (Philips Series 7000) and further treated with a depilatory cream (Veet) for 1.5 min. Then mice were killed by cervical dislocation and the skinfrom the back of the mice was cut into pieces of at least 20 mm in diameter and preserved in Dulbecco's modified Eagle medium (DMEM) supplemented with gentamicin (0.4%). The thickness of the skin was determined with skin cutting with cryostat and was determined to be 800-1000 μm.

A static Franz diffusion cell (Proviskin, France) exhibiting an effective area of 0.785 cm^2 was used for skin permeability tests. After filling the receptor compartment with degassed phosphate buffer saline (PBS) with pH = 7.4, the solution was maintained at 32 °C using a circulating bath (Julabo) and stirred with a magnetic stirring bar at around 500 rpm. The mouse skin was carefully clamped between the donor and the receptor compartment (8 mL). Pre-incubation in the receptor compartment medium for 20 min was performed before the two different metformin hydrogels(GO/metformin, rGO-COOH/metformin) were applied to the skin previously wetted with 30 μL of a glycerin solution (50%) to insure contact between the patch and the skin. The metformin hydrogels were illuminated with a 980 nm laser at different power densities(1 W cm^{-2}) to ~50 °C. At determined time intervals (every hour for a total period of 6 h), 500 μL aliquots of diffused solution were removed from the receptor compartment and analysed using HPLC. After each sampling, an equal volume of fresh diffusion medium was added to the receptor compartment to maintain a constant volume. All experiments were performed in triplicates.

The release and permeation profiles were determined by plotting the cumulative amount of metformin in the receptor compartment (Q_{exp}) against time:

$$Q_{exp} = c_n \times V + \sum_{i=1}^{n-1} c_i \times V,$$

with Q_{exp} the cumulative amount of metformin diffused through the skin (µg), $c_n$theamount of metformin (µg) determined at the n^{th} sampling interval, and V the volume of the acceptor phase (receptor compartment) (mL).The metformin flux (J) was determined according to

$J = A/S$,

with J the flux of metfromin through the skin (µg cm^{-2} h^{-1}), $A$the linear slope of the cumulative amount *versus* time curves in equilibrium conditions (µg h^{-1}), and S the surface of the membrane of the Franz cells

To estimate the amount of in metformin trapped in the skin, the skin was added into water/ice mixture for 10 min and sonicated in the presence of ZnO_2 beads (4 mm in diameter), before being centrifuged for 30 min at 13500 rpm using an ultracentrifuge (Midi Scanfuge ORIGIO). The liquid phase was collected and filtrated through a 0.1 µm Nylon filter (Whatman Puradisc 13 mm) and the amount of metformin was determined.

6.4.9 *In vitro* assessment of metformin activity

In vitro assessment of metformin activity was performed using the Immortalized Human Hepatocytes (IHH) as relevant Human hepatocyte cell model as they retain features of normal hepatocytes[10]. IHH cells (maintained at passages 25-35) were cultured in Williams E medium (Invitrogen) containing 11 mM glucose and supplemented with 10 % fetal calf serum (FCS; Eurobio), 100 U/mL penicillin, 100 µg/mL streptomycin, 20 mU/mL insulin (Sigma-Aldrich) and 50 nM dexamethasone (Sigma-Aldrich). The activity of metformin when heated at 45 °C, 55 °C and 65 °C was assessed by monitoring the glucose-6-phosphatase catalytic (G6PC) gene expression from IHH cells (4×10^5 cells) cultured in 12-well plates in a Dulbecco's Modified Eagle Medium (DMEM; Invitrogen) supplemented with 5 mM glucose, 2 % FCS, 100 U/mL penicillin, 100 µg/mL streptomycin containing either PBS (Control) or 5 mM heated metformin for 24 h. Total RNA was extracted from IHH cells according to the manufacturer's protocol (RNeasy Lipid Tissue Kit, Qiagen). The RNA purity and concentration were determined by RNA Integrity Number (RNA 6000 Nano Kit, 2100 Bioanalyser, Agilent). Total RNA was transcribed into cDNA as described before.11 Each cDNA sample was quantified by quantitative real-time polymerase chain reaction using the fluorescent TaqMan 5′-nuclease assays or a BioRad MyiQ Single-Color Real-Time PCR Detection System using the BioRad iQ SYBR Green Supermix, with 100 nM primers and 1 µL of template per 20 µL of PCR and an annealing temperature of 60 °C. Gene expression

analysis was normalized against TATA box Binding Protein (*TBP*) expression or 60S acidic ribosomal protein P0 (*RPLP0*). Primers for human *RPLP0* (sense 5′- ACCTCCTTTTTCCAGGCTTT -3′; antisense 5′- CCCACTTTGTCTCCAGTCTTG -3′); Primers for human G6PC (sense 5'-AGACTCCCAGGACTGGTTCA-3'; antisense 5'-ACAGGTGACAGGGAACTGCT-3'); Primers for human TBP (sense 5'-GAACCACGGCACTGATTTTC-3' and antisense 5'- CCCCACCATGTTCTGAATCT-3')

6.4.10 Histological analysis of laser irradiated skin

Immediately after transdermal tests, the skins were embedded into OCT and frozen sectioned in a cryostat(-20 °C). The sectioned skins were then fixed in 4% paraformaldehyde for 30 min, followed by staining with Hematoxylin and Eosin (H&E) kit (Victor labs) according to a standard protocol. After dehydration through 3 times pass in absolute ethanol, the stained slides were imaged under an inverted microscope(Nikon Ti2-U) equipped with a CFI plan Apo Lambda 4× objective. The images were treated with NIS-Elements Documentation software.

6.5 *In Vivo* experiments

6.5.1 *In Vivo* Photothermal Therapy and Histology

Studies involving animals, including housing and care, method of euthanasia, and experimental protocols were conducted in accordance with the local animal ethical committee in the animal house (June 24, 2013; protocol 6) of Danylo Halytsky Lviv National Medical University, under the supervision of Dr. R. Bilyy. Six-week-old male Balb/c mice were used for this investigation. The mice were housed in cages covered with air filters in a temperature controlled room with a 12 h light and 12 h dark schedule and kept on a standard diet with drinking water available ad libitum. All animal experiments were performed in accordance with institutional ethical guidelines. Specifically, 11 white laboratory Balb/c mice were evaluated for skin recovery. To establish the surface infection, mouse hair was removed using MedaSept medical depilation cream and a patch of plaster was continuously applied to the area of skin 15 times with the aim to remove the superficial epidermis. Then 10 μL of Staphylococcus epidermidis bacterial cell culture containing 2×10^7 cfu mL^{-1} was applied and superficial skin infection was allowed to be established for 24 h [11]. After 24 h, mice were anesthetized and sterilized (immersion of the patches into Anios DDSH (ANIOS, France), a cleaning disinfectant for medical devices for 1 h) K/Au NHs (three mice) or K/Au

NHs-rGO (five mice) patches were applied to the skin with the rGO layer facing the skin. Finally, three mice were not treated and used as control. The patch was illuminated for 5 min with the LED array (6×6 mm^2 in size, 10 W, 940 nm) and the surface temperature controlled by the FLIR IR camera to be within 50−52 °C for K/Au NHs-rGO and 36−38 °C for K/Au NHs. Mice were photographed with a Nikon camera equipped with Micro-Nikkor objective, from a fixed position and with reference ruler present in each picture. Photos were processed with ImageJ software to detect erythema, and its area before and 24 h after treatment with patch was evaluated. Mice were sacrificed after 5 days of treatment. The skin was removed, photographed, and fixed with 4% neutral buffered formalin solution and embedded in paraffin according to the standard laboratory protocol. The sliced tissues were stained with hematoxylin (for nucleic acids) and eosin (for basic residues, arginines and lysines, on proteins) (H&E), and Gram stain (for Gram-positive bacteria) using routine laboratory procedures.

6.6 References

[1] Qi, J.; Motwani, P.; Gheewala, M.; Brennan, C.; Wolfe, J.C.; Shih, W.-C. Surface-enhanced Raman spectroscopy with monolithic nanoporous gold disk substrates. Nanoscale 2013. 5(10): p. 4105-4109.

[2] Santos, G.M.; Zhao, F.; Zeng, J.; Shih, W.-C. Characterization of nanoporous gold disks for photothermal light harvesting and light-gated molecular release. Nanoscale 2014. 6(11): p. 5718-5724.

[3] Zhang, J.T.; Wang, L.; Lamont, D.N.; Velankar, S.S.; Asher, S.A. Fabrication of large-area two-dimensional colloidal crystals. Angewandte Chemie International Edition in English 2012. 51(25): p. 6117-20.

[4] Xuesong Li; Weiwei Cai; Jinho An; Seyoung Kim; Junghyo Nah; Dongxing Yang; Richard Piner; Aruna Velamakanni; Inhwa Jung; Emanuel Tutuc; Sanjay K. Banerjee; Luigi Colombo; Ruoff, R.S. Large-Area Synthesis of High-Quality and Uniform Graphene Films on Copper Foils. Science 2009. 324(5932): p. 1312-4.

[5] Rodenstein, M.; Zurcher, S.; Tosatti, S.G.; Spencer, N.D. Fabricating chemical gradients on oxide surfaces by means of fluorinated, catechol-based, self-assembled monolayers. Langmuir 2010. 26(21): p. 16211-20.

[6] Barras, A.; Szunerits, S.; Marcon, L.; Monfilliette-Dupont, N.; Boukherroub, R. Functionalization of diamond nanoparticles using "click" chemistry. Langmuir 2010. 26(16): p. 13168-72.

[7] Mazur, M.; Barras A Fau - Kuncser, V.; Kuncser V Fau - Galatanu, A.; Galatanu A Fau - Zaitzev, V.; Zaitzev V Fau - Turcheniuk, K.V.; Turcheniuk Kv Fau - Woisel, P.; Woisel P Fau - Lyskawa, J.; Lyskawa J Fau - Laure, W.; Laure W Fau - Siriwardena, A.; Siriwardena A Fau - Boukherroub, R.; Boukherroub R Fau - Szunerits, S.;

Szunerits, S. Iron oxide magnetic nanoparticles with versatile surface functions based on dopamine anchors. Nanoscale 2013. 5(7): p. 2692-2702.

[8] Kaiser E.; Colescott, R.L.; Colescott, R.; Bossinger, C.D.; Bossinger, Cd.; Cook, P.I.; Cook, P.I. Color test for detection of free terminal amino groups in the solid-phase synthesis of peptides. Analytical Biochemistry 1970. 34(2): p. 595-8.

[9] Sun, X.; Liu, Z.; Welsher, K.; Robinson, J.T.; Goodwin, A.; Zaric, S.; Dai, H. Nano-graphene oxide for cellular imaging and drug delivery. Nano Research 2008. 1(3): p. 203-212.

[10] Abderrahmani, A.; Yengo, L.; Caiazzo, R.; Canouil, M.; Cauchi, S.; Raverdy, V.; Plaisance, V.; Pawlowski, V.; Lobbens, S.; Maillet, J.; Rolland, L.; Boutry, R.; Queniat, G.; Kwapich, G.; Tenenbaum, M.; Bricambert, J.; Saussenthaler, S.; Anthony, E.; Jha, P.;Derop, J.; Sand, O.; Rabearivelo, I.; Leloire, A.; Pigeyre, M.; Daujat-Chavanieu, M.; Gerbal-Chaloin, S.; Dayeh, T.; Lassailly, G.; Mathurin, P.; Staels, B.; Auwerx, J.; Schürmann, A.; Postic, C.; Schafmayer, C.; Hampe, J.; Bonnefond, A.; Pattou F.; and P. Froguel, Diabetes. 2018, 67: p. 1310-1321.

[11] Kugelberg, E.; Norstrom, T.; Petersen, T.K.; Duvold, T.; Andersson, D.I.; Hughes, D. Establishment of a superficial skin infection model in mice by using Staphylococcus aureus and Streptococcus pyogenes. Antimicrobial Agents and Chemotherapy 2005. 49(8): p. 3435-41.

LIST OF PUBLICATIONS

1. **Li, C.**; Ye, R.; Bouckaert, J.; Zurutuza, A.; Drider, D.; Dumych, T.; Paryzhak, S.; Vovk, V.;Bilyy, R.O. ; Melinte, S.; Li, M.; Boukherroub, R.; Szunerits.,S., Flexible Nanoholey Patches for Antibiotic-Free Treatments of Skin Infections. ACS Appl. Mater. Interfaces, 2017,9, pp.36665−36674.

2. Halouane, F.; Jijie, R.; Meziane, D.; **Li, C.**; Singh, S. K. ; Bouckaert, J.; Jurazek, J.; Kurungot, S.;Barras, A.; Li, M.; Boukherroub, R.; Szunerits, S., Selective isolation and eradication of E. coliassociated with urinary tract infections using anti-fimbrial modified magnetic reduced grapheneoxide nanoheaters. J. Mater. Chem. B, 2017, 5(40), pp.8133-8142.

3. Jijie, R.; Dumych, T.; **C, Li.**; Bouckaert, J.; Turcheniuk, K.; Hage, C.; Heliot, L.; Cudennec, B.; Dumitrascu, N.; Boukherroub, R.; Szunerits, S., Particle-based photodynamic therapy based on indocyanine green modified plasmonic nanostructures for inactivation of a Crohn's disease associated Escherichia coli strain. J. Mater. Chem. B, 2016, 4(15), pp.2598-2605.

4. Mohammad, F.; Sahraei, A.; **Li, C.**; Haustrate, A.; Lehen’kyi, V.; Barras, A.; Boukherroub, R.; Szunerits, S. Interaction of Human α-1-Acid Glycoprotein (AGP) with Citrate-Stabilized Gold Nanoparticles: Formation of Unexpectedly Strong Binding Events. J. Phys. Chem. C, 2019, 123 (8), pp.5073-5083.